Nonlinear Dynamic Modeling and Simulation of a Passively Cooled Small Modular Reactor

by

Samet Egemen Arda

A Dissertation Presented in Partial Fulfillment
of the Requirements for the Degree
Doctor of Philosophy

Approved November 2016 by the
Graduate Supervisory Committee:

Keith E. Holbert, Chair
John Undrill
Daniel Tylavsky
George Karady

ARIZONA STATE UNIVERSITY

December 2016

ABSTRACT

A nonlinear dynamic model for a passively cooled small modular reactor (SMR) is developed. The nuclear steam supply system (NSSS) model includes representations for reactor core, steam generator, pressurizer, hot leg riser and downcomer. The reactor core is modeled with the combination of: (1) neutronics, using point kinetics equations for reactor power and a single combined neutron group, and (2) thermal-hydraulics, describing the heat transfer from fuel to coolant by an overall heat transfer resistance and single-phase natural circulation. For the helical-coil once-through steam generator, a single tube depiction with time-varying boundaries and three regions, i.e., subcooled, boiling, and superheated, is adopted. The pressurizer model is developed based upon the conservation of fluid mass, volume, and energy. Hot leg riser and downcomer are treated as first-order lags. The NSSS model is incorporated with a turbine model which permits observing the power with given steam flow, pressure, and enthalpy as input. The overall nonlinear system is implemented in the Simulink dynamic environment. Simulations for typical perturbations, e.g., control rod withdrawal and increase in steam demand, are run. A detailed analysis of the results show that the steady-state values for full power are in good agreement with design data and the model is capable of predicting the dynamics of the SMR. Finally, steady-state control programs for reactor power and pressurizer pressure are also implemented and their effect on the important system variables are discussed.

Dedication

To

my beloved Sister

ACKNOWLEDGMENTS

First and foremost, I should express my sincere gratitude to Dr. Keith E. Holbert for accepting me as one of his student and giving me the once-in-a-lifetime opportunity of studying on this PhD degree level project. As a mentor, his expertise and insight contributed to my graduate experience considerably. I felt his support, guidance, and encouragement during every stage of this study, from the start to the end.

I also give special thanks to Dr. John Undrill for his interest and excitement over the project. He not only helped me about programming but also taught me the importance of relating the theoretical discussions to real physical systems which expanded my understanding of what the engineering really means.

I am very grateful to the member of my supervisory committee, Dr. Daniel Tylavsky and Dr. George Karady, for the consideration to be members of the committee and allocating their precious time to do that.

Finally, I would like to take this opportunity to express my heartfelt gratitude towards my sister and her husband in Turkey as well as my relatives for showing their love, support, and encouragement whenever I needed which contributed significantly to the fulfillment of a long-held dream.

TABLE OF CONTENTS

Page

CHAPTER Page

CHAPTER Page

LIST OF TABLES

LIST OF FIGURES

Figure Page

Figure Page

Figure Page

Figure Page

CHAPTER 1 INTRODUCTION

1.1 Motivation

A small reactor, defined by the International Atomic Energy Agency (IAEA), is a nuclear reactor with an output of less than 300 MWe [1]. The term “modular” is derived from the fact that small reactors can be manufactured in a factory completely and delivered to the site for installation.

The first commercial nuclear power plant in the U.S. was the Shippingport Atomic Power Station with a total capacity of 60 MWe [2]. The plant, which was located 40 km away from Pittsburg, reached critically on December 2, 1957 and was able to produce electricity on December 18, 1957. Since then, the capacity of a single reactor has been increased up to around 1600 MWe considering economy of scale (see Figure 1.1). However, even in the 1960s when the trend was toward larger plant sizes, the potential of SMRs was being considered [3]. Starting with the late 1970s in the U.S., new projects for construction of nuclear power plants mostly have been postponed or canceled due to high initial investments, construction period exceeding 10 years, and cumbersome licensing process [4]. In fact, for the first time after almost 35 years, the Nuclear Regulatory Commission (NRC) approved construction and operation licenses for units 3 and 4 of the Alvin W. Vogtle Electric Generating Plant on February 10, 2012. Prior to that, the last construction permit for a nuclear power plant was issued in 1978 for the Shearon Harris Nuclear Power Plant located in New Hill, North Carolina [5].

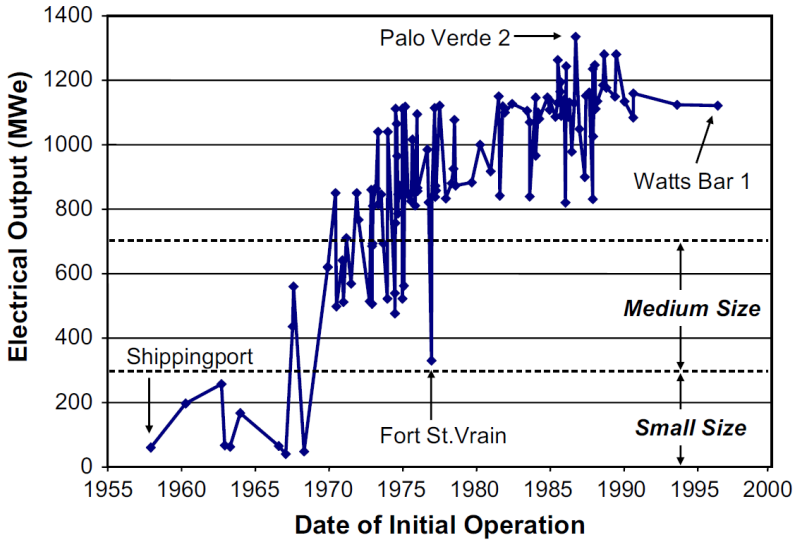

Figure 1.1 Electrical output of U.S. commercial nuclear power plants [6].

Starting in the last decade, there has been a growing trend in the development and commercialization of small modular reactors (SMRs) not only in the U.S. but also in other countries including Russia, Japan, France, India, Argentina, South Korea, and China. However, these SMRs are not intended to be scaled-down version of today's large nuclear reactors. The key in this scramble is to create a unique design, primarily, with the idea of combining steam generators and pressurizer with the reactor core in the reactor pressure vessel which is described with the term 'integral'. Furthermore, lessons learned from 60 years of nuclear engineering and tragic accidents such as Three Mile Island, Chernobyl, and Fukushima compel the industry to develop intrinsically safer and more secure reactors.

To support U.S.-based SMR projects, the Department of Energy (DOE) launched a program called SMR Licensing Technical Support Program in March 2012 [7]. According to this 6-year 452 million dollars cost-share public-private partnership, two

industry members were each awarded with half of the total funding. The first half of the funding was provided to a consortium led by Babcock & Wilcox (B&W) and including the Tennessee Valley Authority and Bechtel on November 20, 2012 [8]. Approximately one year later, DOE announced on December 12, 2013 that NuScale Power LLC would be the company receiving the second half of the funding [9]. Different design features of these two companies' SMRs will be discussed later.

SMRs can be utilized to supply the electricity needs of remote areas suffering from the lack of transmission and distribution infrastructure and also generate local power for particular regions within large population centers. In addition, SMR technology presents an ideal opportunity for small countries where the power demand does not change significantly and countries facing problems with high initial investments associated with large nuclear power plants [10]. However producing electricity is not the only area where SMRs are applicable. Other applications including: water desalination, general process heat for chemical or manufacturing processes, and district heating are also possible with appropriate design.

Advantages of SMRs can be categorized into four groups [11]:

1. Fabrication and construction,
2. Plant safety,
3. Operational flexibility, and
4. Economics.

Fabrication and construction: Parallel with power outputs of SMRs, the physical size of major components in a reactor shrinks which provides simplicity in manufacturing

by reducing or eliminating the need for forging and requires less advanced technology. Utilizing conventional fabrication methods is very important since the technology is a limiting factor causing large nuclear reactors to be manufactured by a few vendors throughout the world. Another problem related to employing large reactor vessel is transportation. Often, reactor vessel size imposes restrictions on possible options for plant location and forces it to be located near the shore of a sea or a large river. On the contrary, SMRs can be transported by a ship, ferry, rail, or even truck and sat onto inland areas or remote locations. Lastly, large nuclear power plants require great amount of on-site work that both increases cost and can cause delays in scheduled construction plan. With SMRs, a higher percentage of a plant can be built in a factory and delivered to the plant site for installation. This also can improve the quality of various components as a result of quality control means of a factory environment.

Plant safety: Regardless of their size and capacity, all nuclear power plants must meet criteria for safe operation. SMRs offer both active and passive features that may not be possible or applied to larger ones. First of all, reduced power output implies that amount of fuel placed in a rector will significantly decrease. Thus, less radioactive gases and fission products, highly dangerous for public health and the habitat around a plant, will be released to the atmosphere in an accident scenario. Moreover, one of the targets with the new design of SMRs is to eliminate large coolant pipes ensuring the circulation of coolant between reactor core and steam generator. This is crucial since any leakage or break of these pipes can result with severe accidents, e.g. reactor meltdown. Hence design of large nuclear power plants includes complex systems and control mechanism for safe circulation of coolant inside both primary and secondary loops. Related to this

aspect, placing steam generator and pressurizer inside reactor vessel will increase the height of the overall system facilitating natural circulation of coolant in a reactor. Finally, due to the size of a SMR, reactors in a plant can be placed into pools under surface level. That provides additional resistance against terror attacks and pools serve as a heat sink for removing the decay heat by radionuclides after a reactor shutdown or in an emergency situation.

Operational flexibility: Nuclear power plants with SMRs compared to ones with large reactors have a smaller footprint, thus, reducing the size of the emergency planning zone [11]. This fact improves the flexibility on site selection and allows reactors to be placed near industrial areas and population centers. A plant site closer to potential customers is very important if the reactor will be utilized for process heat or district heating. Another advantage is that it reduces losses owing to long transmission and distribution lines if the purpose is to produce electricity.

SMRs are also favorable for water usage since less electric output implies less heat rejection to the environment. Thus water demand decreases and the plant does not require a sea or a large river. In addition, reduced dependency on a big water supply is another factor contributing the site selection flexibility.

The other advantage is that smaller capacity and reduced construction time allows matching growth in power demand closely and increasing the power output of a plant incrementally which also impacts plant economics as will be discussed below.

Economics: A typical value for the total cost of a large nuclear power plant is about 10 billion dollars. This is a big capital investment which directly eliminates many

small countries and private utilities from involvement with nuclear industry. However, SMRs enable those countries to start their own nuclear program and utilities to own a nuclear power plant within the local grid they are responsible for.

As mentioned above, the "economy of scale" principle encourages a reactor with higher electrical output but this fact, nevertheless, does not mean that SMRs are not economically viable. In fact, results of a study [12] conclude that the economy of scale law could be overcome by other SMR features such as modularization and lower upfront cost. These features increase SMR competitiveness over large reactors. For example, in case of a nuclear power plant comprising four SMRs, the construction plan can be organized in a way that each reactor is built after the preceding one is complete. In other words, when the first unit starts generating revenue, the second one comes into production line. As a result, cash outflow significantly drops reducing the risk related to high initial investment of large nuclear power plants.

1.2 Different SMR Designs

Different companies from different parts of the world have various unique designs and configurations for SMRs. A brief summary of some of them is provided below:

CAREM-25 is a prototype reactor and currently being built 110 km northwest of Buenos Aires by the Argentine National Atomic Energy Commission (CNEA) with the help of INVAP in Lima [13]. CAREM-25 is a 100 MWt (27 MWe) light-water pressurized water reactor (PWR) and the design concept was first introduced in 1984 [14]. Natural circulation provides the reactor core cooling and the reactor vessel encompasses 12 vertical helical-coil steam generators. The most prominent feature of

CAREM-25 is that the reactor does not have a pressurizer. The balance between the vaporization in the hot leg and the condensation of vapor due to the colder structures in the steam dome achieves self-pressurization in the primary system [15].

HTR-10 is a high-temperature gas-cooled research reactor with 10 MWt output developed at the Institute of Nuclear & New Energy Technology (INET) in China [16]. It is a modular pebble bed type reactor. The reactor core consists of 2700 spherical fuel elements of UO_2 and each of them has 5 g of heavy metal. In this design, graphite is used as reflector and helium as coolant. Cooler helium at the inlet with a temperature of 250 °C flows from top to bottom of the pebble bed reactor core and it reaches to up to a temperature of 700 °C at the outlet. HTR-10 is not an integral type reactor and the steam generator is connected to the reactor pressure vessel by hot gas duct. The steam generator is a once-through steam generator comprised of 30 helical-coil tube bundles [17]. HTR-10 paved the way for a larger version of its design called HTR-PM. The construction of a power plant comprising two HTR-PMs, each 250 MWt, driving a single 201 MWe steam turbine began in December 2012 at Rongcheng in Shandong province in China. The plant is scheduled be online by 2015 [13].

SMART (System-integrated Modular Advanced Reactor) is a 330 MWt integral reactor developed by Korea Atomic Energy Research Institute (KAERI) [18]. SMART is designed for electricity generation (110 MWe) as well as seawater desalination. The reactor core is cooled with the help of four coolant pumps. The design data indicate the coolant temperature increases by 40 °C while passing through the reactor core

corresponding to a core outlet temperature of 310 °C. The reactor vessel houses 8 helical-coil once-through steam generators [19].

The first DOE sponsored design, B&W's mPower, is developed based upon the knowledge and experience gained by the B&W maritime reactor program. One of these earlier designs is used in Otto Hahn, a nuclear powered merchant ship launched in 1964 [20]. mPower is an integral reactor with an output of 530 MWt. Net electricity generation changes according to type of condenser cooling employed—mPower is expected to produce 180 MWe when evaporative cooling is utilized whereas deploying an air-cooled unit reduces the electrical output to 155 MW. The reactor coolant flow rate relies on forced circulation by eight internal coolant pumps [21], [22].

Other U.S.-based SMRs being developed include the Westinghouse SMR, Holtec SMR-160, and PRISM (Power Reactor Innovative Small Module) by a consortium of General Electric and Hitachi [23]-[26]. The Westinghouse SMR and Holtec SMR-160 are PWRs with electrical outputs of 225 MW and 160 MW, respectively. PRISM, on the other hand, is a sodium-cooled fast neutron reactor expected to produce 311 MWe.

1.2.1 NuScale SMR overview

A detailed overview of the NuScale SMR is provided in this section since its design data are used throughout the modeling effort and dynamic analyses of this dissertation. However, the generic approach adopted in this research can be applied for passively cooled SMRs.

The NuScale SMR, capable of producing 45 MWe, is based on the Multi-Application Small Light Water Reactor (MASLWR) concept which was developed by a

consortium including Idaho National Laboratory and Oregon State University under a DOE-sponsored project [27].

Each nuclear steam supply system (NSSS), as seen in Figure 1.2, is immersed in a reactor pool, which has dimensions of 6 m wide by 6 m long and a depth of 23 m. The reactor pressure vessel is housed in the containment vessel sitting inside the reactor pool. The integral design allows the NSSS to encompass all major components, which are the reactor core, two helical-coil once-through steam generators, and pressurizer [28]. Table 1.1 provides a summary of NuScale SMR design features [29].

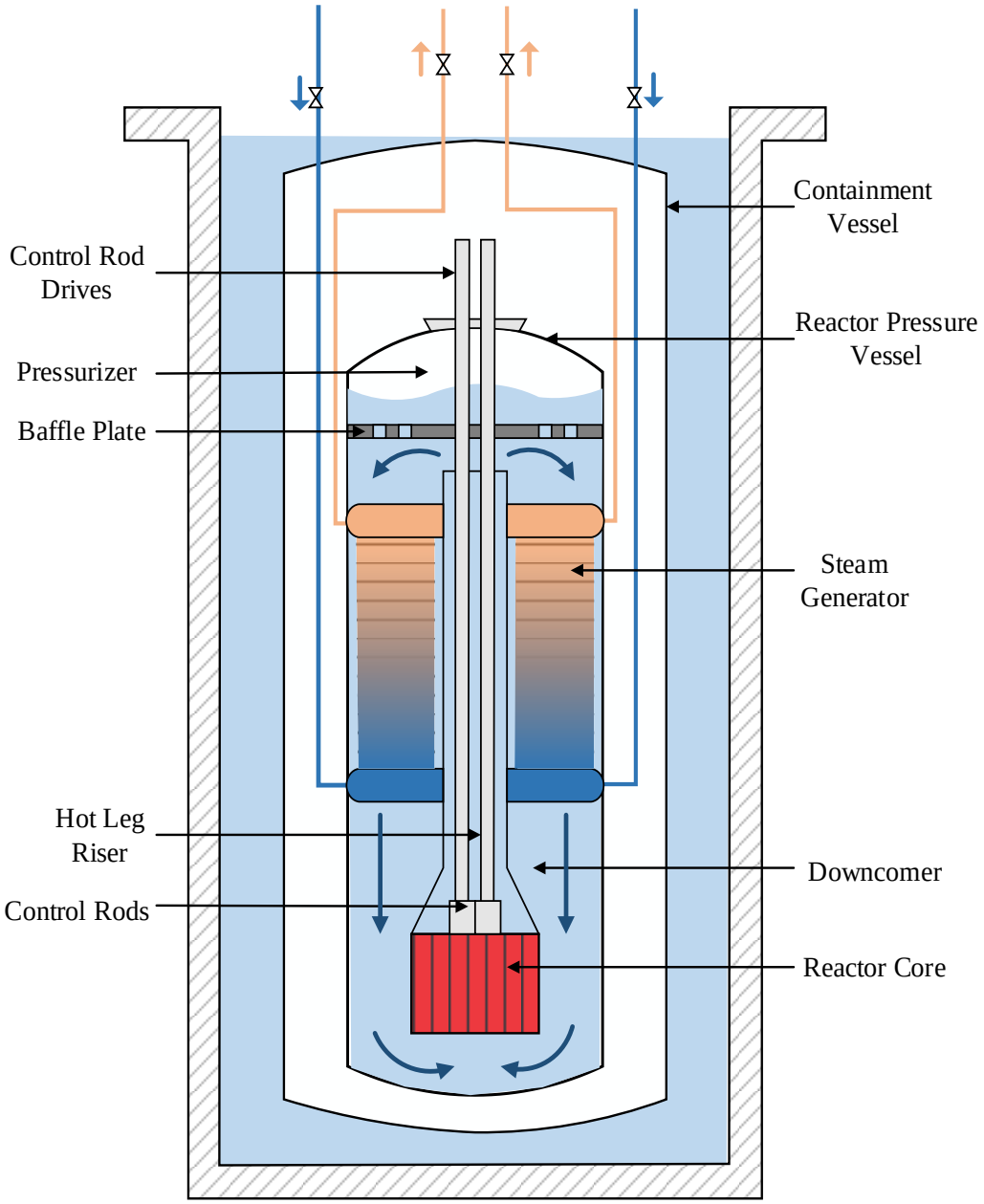

Figure 1.2 Schematic diagram of a single NuScale SMR unit.

Table 1.1 Design features of NuScale SMR

Parameters	**Value**
Reactor thermal power	160 MWt
Power plant output, net	45 MWe
Coolant/Moderator	Light water
Circulation type	Natural circulation
Reactor operating pressure	12.76 MPa
Active core height	2 m
Fuel material	UO_2 ceramic pellets
Fuel element type	17×17, square array
Cladding material	Zircaloy-4
U-235 enrichment	< 4.95%
Fuel cycle length	24 months
Steam generator type	Vertical, helical-coil
Number of steam generators	2
Pressurizer type	Integral

The NuScale SMR design employs natural circulation for the primary coolant system and therefore eliminates reactor coolant pumps. The primary coolant is heated as it passes over the fuel rods and enters the hot leg riser where convection and natural buoyancy provide enough force to drive the fluid upward. After leaving the riser, the primary coolant follows a downward path over the steam generator tubes and the heat is transferred to the feedwater. The denser primary coolant reaches the bottom of the core via the downcomer.

The reactor core is comprised of 37 standard Westinghouse PWR 17×17 square lattice array fuel assemblies with half of the nominal PWR height [30]. Each fuel assembly has 264 fuel pins, 24 guide tube locations for control rods, and a central instrument tube. The core also includes 16 control rod assemblies (CRAs). While four CRAs are used for power regulation during normal plant operation, the others, called the shutdown group, are used for reactor shutdown and scram events [28].

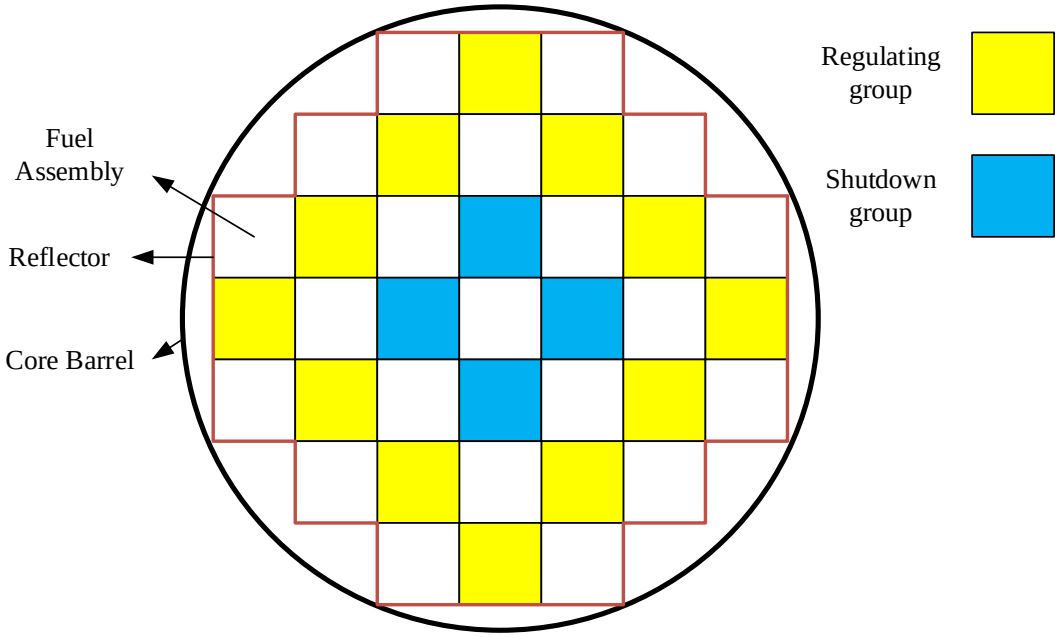

Figure 1.3 Cross-sectional view of NuScale reactor core.

Each NSSS includes two vertical, once-through, helical-coil steam generators. The steam generators are located in the annular space between the hot leg riser and the reactor pressure vessel wall and connections to upper and lower plenums are provided via tubesheets. Each steam generator consists of 506 tubes which are thermally-treated Inconel 690. The tubes have an outside diameter of 16 mm with a 0.9 mm wall thickness and a total length of 22.25 m (see Figure 1.4). The tubes are arranged on a square pitch,

with transverse (P_T) and longitudinal (P_L) pitch ratios of 1.8 and 1.5, respectively [31]. Preheated feedwater enters the lower steam generator plenum through nozzles on the reactor pressure vessel. As feedwater rises through the interior of the steam generator tubes, heat is added from the reactor coolant and the feedwater boils and exits the steam generator as superheated steam.

Figure 1.4 Photo of NuScale full-length helical coil steam generator [32].

The pressurizer is integrated into the top of the reactor pressure vessel and a baffle plate separates the pressurizer from the primary coolant system (see Figure 1.2). The baffle plate, which serves as a thermal barrier between the saturated liquid inside the pressurizer and the primary coolant, has orifices to control the insurge (or outsurge) flow. The pressurizer regulates the primary coolant pressure with electric heaters, installed

above the baffle plate, and spray through nozzles at the top of the reactor pressure vessel. An increase in the coolant pressure is accomplished by actuating electric heaters while the coolant pressure is reduced by spraying cold water from the chemical and volume control system. Unlike traditional PWR pressurizers, a continuous spray flow is not anticipated.

1.3 Research Objectives and Thesis Organization

The main objectives of this study are based upon the following:

- To develop a dynamic model in MATLAB/Simulink for the a passively cooled SMR (such as the NuScale SMR) which is capable of predicting the response of the SMR for typical perturbations; and
- To verify whether the model is realistic or not by comparing the results gathered from other studies.
- To introduce and apply steady-state control algorithms for reactor power and pressurizer pressure.

After this introduction, a review of relevant literature is presented in Chapter 2. While Chapter 3 describes the mathematical models of real physical systems in single SMR unit, Chapter 4 is composed of testing the model in the dynamic environment of Matlab/Simulink. Lastly, Chapter 5 is dedicated to concluding remarks and future work.

CHAPTER 2 LITERATURE REVIEW

2.1 Introduction

Understanding reactor dynamics is crucial to the overall performance of a reactor and the design of suitable control algorithms. That is the reason dynamic modeling attracts a great interest in the nuclear industry.

With the increasing effort into development and commercialization of SMRs, the need for appropriate dynamic models emerges. Although studies regarding individual components of an SMR, i.e., reactor core, steam generator, and pressurizer, are available, there is a lack of complete models for single SMR units in the literature. In addition, different SMR designs require different considerations. In other words, the modeling endeavor is subject to change based on reactor configuration and operation. Considering the problems stated above, a representation for the NuScale SMR is developed in this study.

2.2 Previous Studies on Dynamic Modeling

Kerlin et al. [33] developed a mathematical model for the H. B. Robinson nuclear power plant (NPP) producing 740 MWe (2200 MWth). The model included point kinetics, core heat transfer, piping and plenums, pressurizer, and the steam generator. Point kinetics described the reactor power by using six groups of delayed neutrons and reactivity feedback terms caused by fuel temperature, coolant temperature, and primary loop system pressure. Core thermodynamics were represented with nodal approximation in which every axial section used two coolant temperature nodes for every fuel temperature node because of advantages of this approximation over others such as the

well-mixed and the arithmetic average approximation. The pressurizer was modeled with the help of mass, energy, and volume balances. Moreover, it was assumed that water-steam mixture in the pressurizer was always at saturated conditions. Finally, a control system for the pressurizer was also implemented. For the steam generator, a simple model with the representation of primary fluid, tube metal, and secondary fluid lumps for the heat transfer process was used. All piping and plenums were defined with first-order lags while assuming that the heat was transferred without any losses. First, results for an isolated core when 7.1¢ ($ or ¢ are special units for reactivity which are defined to make the amount of reactivity easier to express) reactivity change occurred and isolated steam generator in the case of 1% increase in steam flow were presented. Following that, the response of the complete model to common step disturbances, such as changes in control rod or steam valve position, were compared with actual measurement results for validation of the theoretical model. A final note was made that the proposed model for the H. B. Robinson NPP was able to predict reactivity and steam valve perturbations well.

In his MS thesis, from which the above paper was derived, Thakkar [34] discussed the modeling of the pressurizer in detail. Validation tests were performed on the isolated pressurizer by step increases in the 3 input variables (insurge and spray flow rate, and electric heat) and changes in the pressure due to these perturbations were presented.

Onega and Karcher [35] wrote a paper about nonlinear modeling of a pressurized water reactor core which incorporates both prompt and delayed temperature feedback. In their model, nonlinearities were treated explicitly, and the temperature dependence of thermal-hydraulic parameters was preserved without any approximation. The isolated core models utilizing six and one group of delayed neutrons were compared with each other for a 30¢ step increase in the reactivity. Then, another comparison was made between the presented nonlinear core heat transfer model with one fuel and coolant node and the linear core heat transfer model with 15 fuel nodes and 30 coolant nodes introduced by Kerlin et al. [33] for a step reactivity insertion of 7.1¢. The results of the comparisons yielded that using six groups of delayed neutrons instead of just one did not have a significant improvement in the response of the model, and the nonlinear and linear core heat transfer models exhibited very similar behavior. In addition, the model responses for a loss of coolant pump and decrease in the coolant inlet temperature were provided.

One of the early studies about natural circulation phenomena in PWRs was conducted by Zvirin [36]. The study was focused on the single-phase natural circulation loops in which heat is transferred from a heat source to a heat sink at a higher elevation. Such loops are applicable in cooling systems of light water reactors (LWRs) and liquid metal fast breeder reactors (LMFBRS), and energy conversion systems such as solar heaters. After a review of existing modeling approaches to natural circulation loops, analytical and numerical methods were used to solve the conservation equations for momentum and energy. The results under both steady-state and transient conditions were presented and relevant stability characteristics were discussed. The effects of various

parameters (e.g. geometry, fluid properties, and boundary and initial conditions) were also examined.

More recent studies [37]-[39] investigated the natural circulation in SMRs, such as CAREM-25 and REX-10 (Regional Energy Reactor-10 MWt), and TRIGA Mark II. CAREM-25 is a 27 MWe SMR design by Argentina, as discussed previously, and REX-10 is a 10 MWt prototype reactor by South Korea based on the SMART. The TRIGA Mark II, however, is a low power pool-type research reactor designed and manufactured by General Atomics [40]. All of these studies took advantage of the fact that the coolant temperature gradient in the primary loop is the main mechanism for the natural circulation and performed a momentum balance. Afterwards, an expression for the primary coolant mass flow rate was derived via the energy balance equation for the core at steady-state conditions. The analysis indicated that the reactor thermal power had significant impact on the natural circulation behavior whereas the primary pressure did not show remarkable effect on natural circulation.

Modeling effort for once-through steam generators has received considerable attention since the computerized simulation techniques evolved. In 1976, Ray and Bowman [41] presented a nonlinear dynamic model of a helical-coil once-through subcritical steam generator for gas-cooled reactors. The model included three sections (economizer, evaporator, and superheater) with time-varying phase boundaries. The nonlinear system composed of differential and algebraic equations was developed based on the conservation of mass, momentum, and energy. The transient response of 8 state variables, due to 5% independent step changes in 5 input variables at full power, was

discussed. In 1994, Abdalla [42] introduced a four-region (i.e. subcooled, nucleate boiling, film boiling, and superheated), moving-boundary, draft-flux flow model for the advanced liquid metal reactor superheated cycle heat-exchanger which is a once-through, helical-coil steam generator. The model was tested for a number of transients including: 10% increases in (1) primary coolant inlet temperature, (2) feedwater flow rate, and (3) outlet steam pressure; and (4) 80% decrease in feedwater flow rate. The results indicated that the model is capable of simulating properly the dynamic response of the steam generator for a wide range of conditions. In a similar manner, recent papers [43], [44] developed representations for the once-through helical-coil steam generator of HTR-10. While Reference [43] incorporated subcooled, boiling, and superheated regions, the latter one employed only subcooled and boiling sections.

CHAPTER 3 DEVELOPMENT OF MATHEMATICAL MODELS

In this section, mathematical modeling of all major components inside a passively cooled SMR, i.e., reactor core, steam generator, pressurizer, hot leg riser, and downcomer is discussed in detail. In addition, control options for reactor power and primary coolant system pressure are presented.

3.1 Reactor Core Model

The reactor core is represented with a combination of neutronics and thermohydraulics model.

3.1.1 Reactor neutronics

The time dependent behavior of neutrons inside the reactor core is described with a point kinetics model, consisting of one energy group and a single combined neutron precursor group [33] and [35]. However, the point kinetics equations are expressed in terms of reactor thermal power (P) since P is proportional to average neutron density. The balance equations are written as:

$$\frac{dP}{dt} = \frac{\rho - \beta}{\Lambda} P + \lambda C \tag{3.1}$$

$$\frac{dC}{dt} = \frac{\beta}{\Lambda} P - \lambda C \tag{3.2}$$

where C is the delayed neutron precursors; ρ is the reactivity; β is the effective delayed neutron fraction; Λ is the neutron generation time; and λ is the decay constant for the delayed neutron precursor.

The reactivity term in Equation (3.1) is also time dependent even though it is zero during steady-state operation. Changes in the position of control rods are an external reactivity input allowing the PWR to operate at different power levels. In addition, reactivity feedback terms due to changes in fuel and moderator temperatures contribute to the system reactivity and couple neutronics with thermohydraulics. Based on these contributors, the reactivity of the system can be expressed as:

$$\rho = \delta\rho_{ext} + \alpha_F \, \delta T_F + \alpha_C \, \delta T_C + \alpha_P \, \delta p_P \tag{3.3}$$

α_F (-2.16×10^{-5}/°C), α_C (-1.8×10^{-4}/°C), and α_P (1.08×10^{-6}/°C) are the reactivity feedback coefficients of fuel and coolant (moderator) temperature and primary coolant pressure [33] and [45], respectively; δT and δp represent the deviation from the steady-state for fuel (F) and coolant (C) temperatures and primary coolant pressure (P); and $\delta\rho_{ext}$ is the reactivity induced by control rod movement.

3.1.2 Reactor thermal-hydraulics

3.1.2.1 Mann's model for heat transfer process

The heat transfer process in the core region is represented using Mann's model [46] that utilizes two coolant lumps for every fuel lump as seen in Figure 3.1. In this model, the temperature difference is taken as the difference between the fuel temperature and the average temperature of the first coolant lump. This approach provides better physical representation than utilizing just one coolant lump in which generally the average coolant temperature is the mean value of inlet and outlet coolant temperatures.

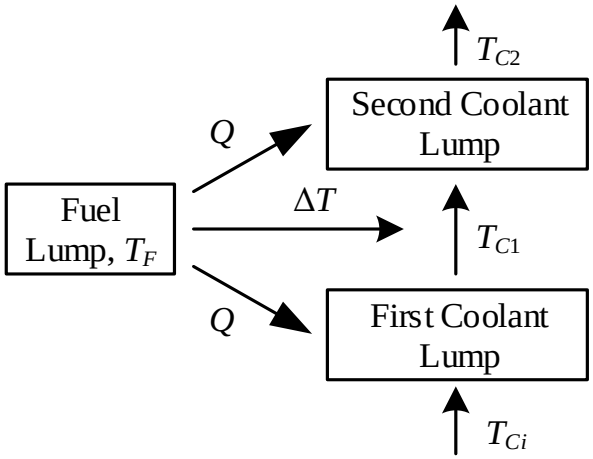

Figure 3.1 Schematic diagram of heat transfer model in reactor core.

Modeling is achieved by considering a number of assumptions including

- one-dimensional fluid flow model is utilized;
- coolant lumps are considered to be well-stirred; and
- the fuel-to-coolant heat transfer coefficient is assumed to be constant.

The governing equations for the behavior of fuel and coolant temperatures are obtained by applying energy conservation to fuel and coolant volumes. The equations describing the fuel and coolant lumps are then

$$\frac{d}{dt}\left(m_F c_{p,F} T_F\right) = f_d P - (UA)_{FC}\left(T_F - T_{C1}\right) \tag{3.4}$$

$$\frac{d}{dt}\left(\frac{m_C}{2} c_{p,C} T_{C1}\right) = \frac{\left(1-f_d\right)}{2} P + \left(U\frac{A}{2}\right)_{FC}\left(T_F - T_{C1}\right) - \dot{m}_C c_{p,C}\left(T_{C1} - T_{Ci}\right) \tag{3.5}$$

$$\frac{d}{dt}\left(\frac{m_C}{2} c_{p,C} T_{C2}\right) = \frac{\left(1-f_d\right)}{2} P + \left(U\frac{A}{2}\right)_{FC}\left(T_F - T_{C1}\right) - \dot{m}_C c_{p,C}\left(T_{C2} - T_{C1}\right) \tag{3.6}$$

where T_F, T_{C1}, and T_{C2} are the average temperatures of the fuel and first and second coolant lumps, respectively, while T_{Ci} is the core inlet coolant temperature; m and c_p are the mass and specific heat of the particular region; f_d is the fraction of the total power directly deposited in the fuel; U_{FC} and A_{FC} are the heat transfer coefficient from fuel to coolant and effective heat transfer surface area, respectively; and finally $\dot{m}_C$ is the mass flow rate of the coolant in the core.

3.1.2.2 Thermal resistance evaluation

The developed thermodynamics model relates the core thermal power to the overall temperature drop from fuel to coolant via an overall heat transfer resistance which can be stated as $R = 1/(UA)_{FC}$ and dictates that, at steady-state conditions, the produced energy equals to the energy given to the coolant. Then, Equation (3.4) can be reorganized as

$$R = \frac{\left(T_F^0 - T_{C1}^0\right)}{f_d P^0} \tag{3.7}$$

where terms with superscripts define the value of the associated parameters at steady-state conditions.

The thermal resistance is constituted by a series of resistances due to the fuel, the gap between the fuel and cladding, the cladding, and the convective heat transfer between the outer surface of the cladding and coolant [39]. Thus, the global heat transfer resistance can be formulated as:

$$R = \frac{1}{n_{fr}}\left(R_f + R_g + R_c + R_s\right) \tag{3.8}$$

where n_{fr} is the total number of fuel rods inside the core; and R with the associated subscript is the thermal resistance of the fuel (f), the gap (g), the cladding (c), and the thermal resistance between the outer surface (s) of the cladding and coolant.

Substituting each term with its equivalence yields that [35], [47]

$$R = \frac{1}{n_{fr}}\left[\frac{1}{4\pi k_f H} + \frac{1}{2\pi r_f h_g H} + \frac{1}{2\pi k_c H}\ln\left(\frac{r_f + t_g + t_c}{r_f + t_g}\right) + \frac{1}{\pi d h_s H}\right] \tag{3.9}$$

Geometrical properties [48] in Equation (3.9) are defined and their values are tabulated in Table 3.1.

Table 3.1 Parameters used to calculate fuel-to-coolant thermal resistance

Symbol	Definition	Value
r_f	Fuel pellet radius	0.409 cm
H	Active core height	2 m
t_g	Gap thickness	9×10^{-3} cm
t_c	Cladding thickness	0.057 cm
d	Fuel rod diameter	0.95 cm
p	Pin pitch	1.26 cm

The gap heat transfer coefficient (h_g) is taken as 5678 $W\cdot m^{-2}\cdot°C^{-1}$ which is a typical value for a standard pressurized water reactor fuel rod while fuel (k_f = 4.15 $W\cdot m^{-1}\cdot°C^{-1}$) and cladding ($k_c$ = 19.04 $W\cdot m^{-1}\cdot°C^{-1}$) thermal conductivities are obtained from Lamarsh and Baratta [49]. The heat transfer coefficient of the cladding surface (h_s) is calculated by utilizing a *Dittus-Boelter correlation* [50] and it can be described as:

$$h_s = \left(0.042\frac{p}{d} - 0.024\right)\frac{k}{D_e}\mathrm{Re}^{0.8}\,\mathrm{Pr}^{1/3} \quad \begin{bmatrix} 0.7 < \mathrm{Pr} < 100 \\ \mathrm{Re} > 10{,}000 \\ H/d > 60 \end{bmatrix} \tag{3.10}$$

where D_e is the equivalent (hydraulic) diameter; k is the thermal conductivity of the primary coolant; Re and Pr are the Reynolds and Prandtl numbers, respectively.

3.1.2.3 Single-phase natural circulation model

The main contributor to natural circulation in a passively cooled SMR is the so-called buoyancy force that is the movement of coolant inside a reactor due to the coolant temperature gradient at various locations in the primary coolant system. In other words, the change in coolant density caused by the coolant temperature gradient establishes enough force to drive coolant either upward or downward depending on the location in the reactor and steam generator.

The assumptions used to carry out the present analysis are listed below:

- Only single-phase natural circulation is considered.
- The coolant within the primary loop is incompressible, meaning the mass flow rate is constant under steady-state conditions.
- The *Boussinesq approximation*, describing the density changes in response to a change in temperature at constant pressure [51], is valid

$$\beta_V = -\frac{1}{\rho}\left(\frac{\partial\rho}{\partial T}\right)_p \tag{3.11}$$

where β_V is the volumetric thermal expansion coefficient.

- The axial component of conductive heat transfer is neglected along the primary coolant system.

Based on these assumptions, momentum balance equations can be summarized in terms of two driving mechanisms as follows:

$$\Delta p_b = \Delta p_l \tag{3.12}$$

where Δp_b and Δp_l are, respectively, the pressure term due to buoyancy forces and the total pressure drop along the primary loop. Hence, it is possible to draw a conclusion that an equilibrium flow rate is reached when buoyancy forces are balanced with pressure losses.

3.1.2.3.1 Buoyancy forces

The driving pressure term due to buoyancy forces can be calculated by the closed path integral:

$$\Delta p_b = \oint \rho_z \, g \, dz \tag{3.13}$$

where ρ_z is the coolant density at specific locations along the vertical (z) axis; and g is gravitational acceleration (see Figure 3.2). Thus, solving Equation (3.13) yields that

$$\Delta p_b = -\bar{\rho}(z_b - z_a)g - \rho_h(z_c - z_b)g - \bar{\rho}(z_d - z_c)g - \rho_c(z_a - z_d)g \tag{3.14}$$

where ρ_h and ρ_c are the coolant density at the hot leg riser and downcomer regions, respectively, and $\bar{\rho}$ is the corresponding average density in that section. After rearranging the above equation and applying the Boussinesq approximation, it takes the form of

$$\Delta p_b = \bar{\rho}\beta_t g\left(T_{C2} - T_{Ci}\right)\Delta L \tag{3.15}$$

where β_t stands for the moderator (coolant) volumetric thermal expansion coefficient.

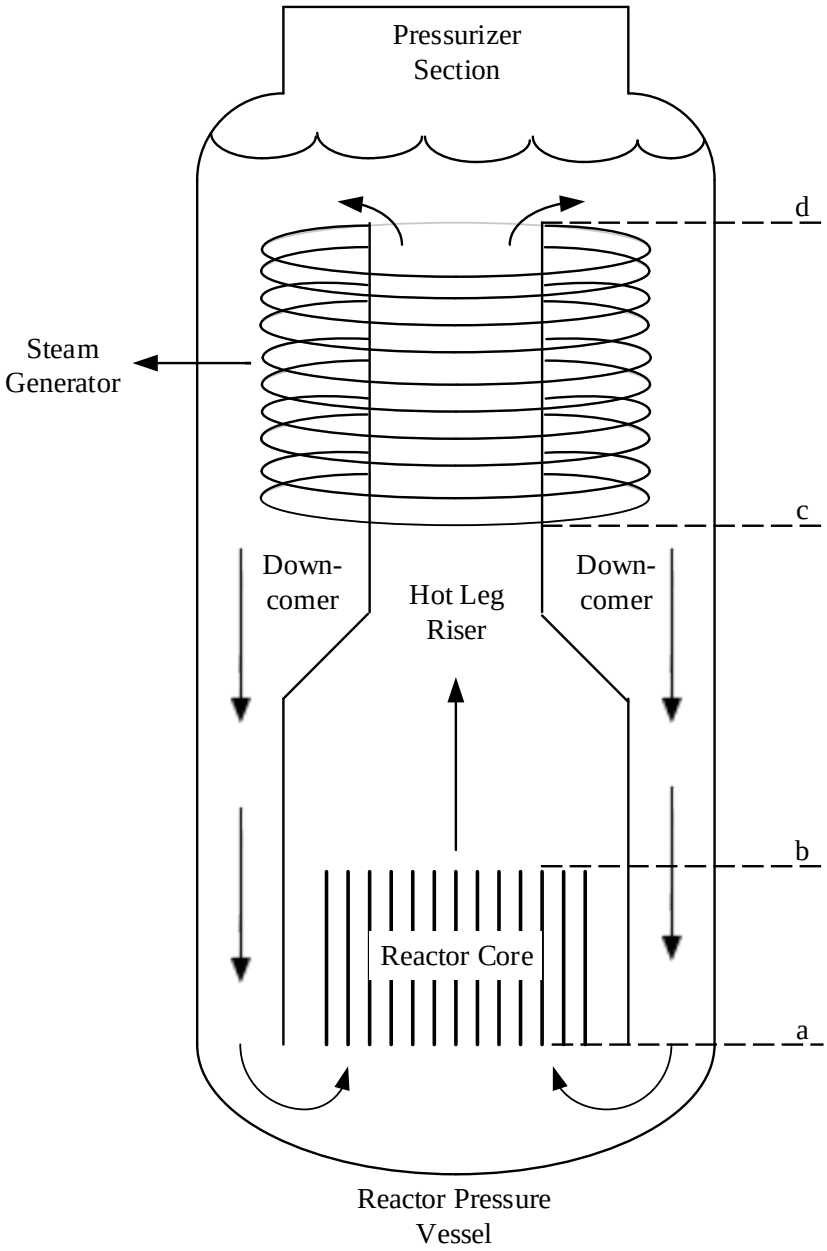

Figure 3.2 Schematic diagram of NuScale SMR.

3.1.2.3.2 Pressure losses

The total pressure drop consists of friction losses and form losses. Pressure losses due to friction occur while coolant flow passes through various components or sections, and form losses are pressure losses due to an abrupt change in flow direction and/or geometry.

The total pressure drop along the primary loop is calculated with the help of the mean density of the coolant inside the primary loop instead of calculating the pressure drop for each section. This is a common practice that is used in other works also [36] - [39].

$$\Delta p_l = \frac{1}{2} R_p \bar{\rho} v^2 \tag{3.16}$$

where v and R_p are the coolant velocity and overall flow resistance, respectively. Then, R_p is defined as:

$$R_p = \sum_{i=1}^{n} f_i \frac{L_i}{D_i} + K_i \tag{3.17}$$

where f is the Fanning friction factor; L is the length of the flow channel; D is the diameter of the flow channel; K is the form loss coefficient; and n number of sections inside primary system, i.e., reactor core, hot leg riser, steam generator, and downcomer.

3.1.2.3.3 Primary coolant flow rate

It is possible to express the coolant mass flow rate through the core as:

$$\dot{m}_C = \rho_{core} v A_{ft} \tag{3.18}$$

where A_{ft} is the total cross-sectional flow area inside the reactor core and ρ_{core} is the density of the primary coolant inside the reactor. After algebraic manipulation and utilizing Equations (3.15) and (3.16), an equation for the mass flow rate is found

$$\dot{m}_C = \sqrt{\frac{2\rho_{core}^2 A_{ft}^2 \beta_t g\left(T_{C2} - T_{Cin}\right)\Delta L}{R_p}} \tag{3.19}$$

where ΔL is the distance between the center of the steam generator to the center of the reactor core.

It should be noticed that the mass flow rate is a nonlinear function of two of the system state variables, i.e., the second coolant lump and reactor core inlet temperatures. The other way of calculating the coolant mass flow rate is to relate $\dot{m}_C$ to the reactor thermal power [15]

$$\dot{m}_C = \sqrt[3]{\frac{2\rho_{core}^2 A_{ft}{}^2 \beta_t g P \Delta L}{R_p \bar{c}_{p,core}}} \tag{3.20}$$

where $\bar{c}_{p,core}$ is the average specific heat of the coolant inside the core region. The conclusion drawn from this new expression is that the coolant mass flow rate is proportional to the cubic root of the reactor thermal power.

3.2 Hot Leg Riser and Downcomer Region

The hot leg riser and downcomer region models are treated as first-order lags, that is

$$\frac{dT}{dt} = \frac{1}{\tau}\left(T_{in} - T\right) \tag{3.21}$$

where $\tau = m/\dot{m}$ is the residence time, and T and T_{in} are the average and inlet coolant temperatures for that particular region, respectively. Then, the energy balance equations for hot leg riser and downcomer region can be written as

$$m_{HL} c_{p,HL} \frac{dT_{HL}}{dt} = \dot{m}_{HL} c_{p,HL} \left(T_{C2} - T_{HL} \right) \tag{3.22}$$

$$m_{DR} c_{p,DR} \frac{dT_{DR}}{dt} = \dot{m}_{DR} c_{p,DR} \left(T_{P1} - T_{DR} \right) \tag{3.23}$$

where m, c_p, T, and $\dot{m}$ are the coolant mass, specific heat, average temperature, and mass flow rate inside the particular region, i.e., the hot leg riser (*HL*) and downcomer (*DR*) regions; and T_{P1} is the primary coolant temperature at the steam generator outlet.

Based on the data obtained from [31], the initial steady-state values of the residence time constants for the hot leg riser (τ_{HL}) and downcomer (τ_{DR}) are calculated as 10.1 and 30.8 seconds, respectively.

3.3 Steam Generator Model

Two common steam generators (SGs) are used in PWRs: (1) recirculation (U-tube) and (2) once-through SGs [52]. In a U-tube SG, heated coolant at high pressure from the reactor core enters at the bottom and follows an upward and then downward path through several thousand inverted U-shaped tubes. In a once-through SG, which usually employs a counterflow heat exchanger, the primary coolant enters at the top and flows downward through tubes and leaves the SG at the bottom. With this design, a dry vapor or a few degrees of superheated steam can be produced. The steam generator configuration in the NuScale SMR is similar to the once-through design. A major

difference is that the reactor pressure vessel of the SMR encompasses the steam generator, thus motivating the use of helical coils to increase the heat transfer area.

Previous works on the dynamic modeling of helical coil SGs treated them as counterflow heat exchangers [41]-[44] although a helical coil SG is a combination cross and counter flow heat exchanger due to its unique design. All of these cited studies assumed that the two-phase flows in all of the tubes are identical which allows analyzing the SG dynamic behavior using a single characteristic tube concept. This treatment and assumption are applied for this SG model also.

3.3.1 Governing equations and assumptions

The helical-coil steam generator model developed in this study is divided into three regions according to conditions inside secondary side, i.e., subcooled, two-phase (or boiling), and superheated. Control volumes are used to derive the model equations and the length of each region is time-varying as depicted in Figure 3.3.

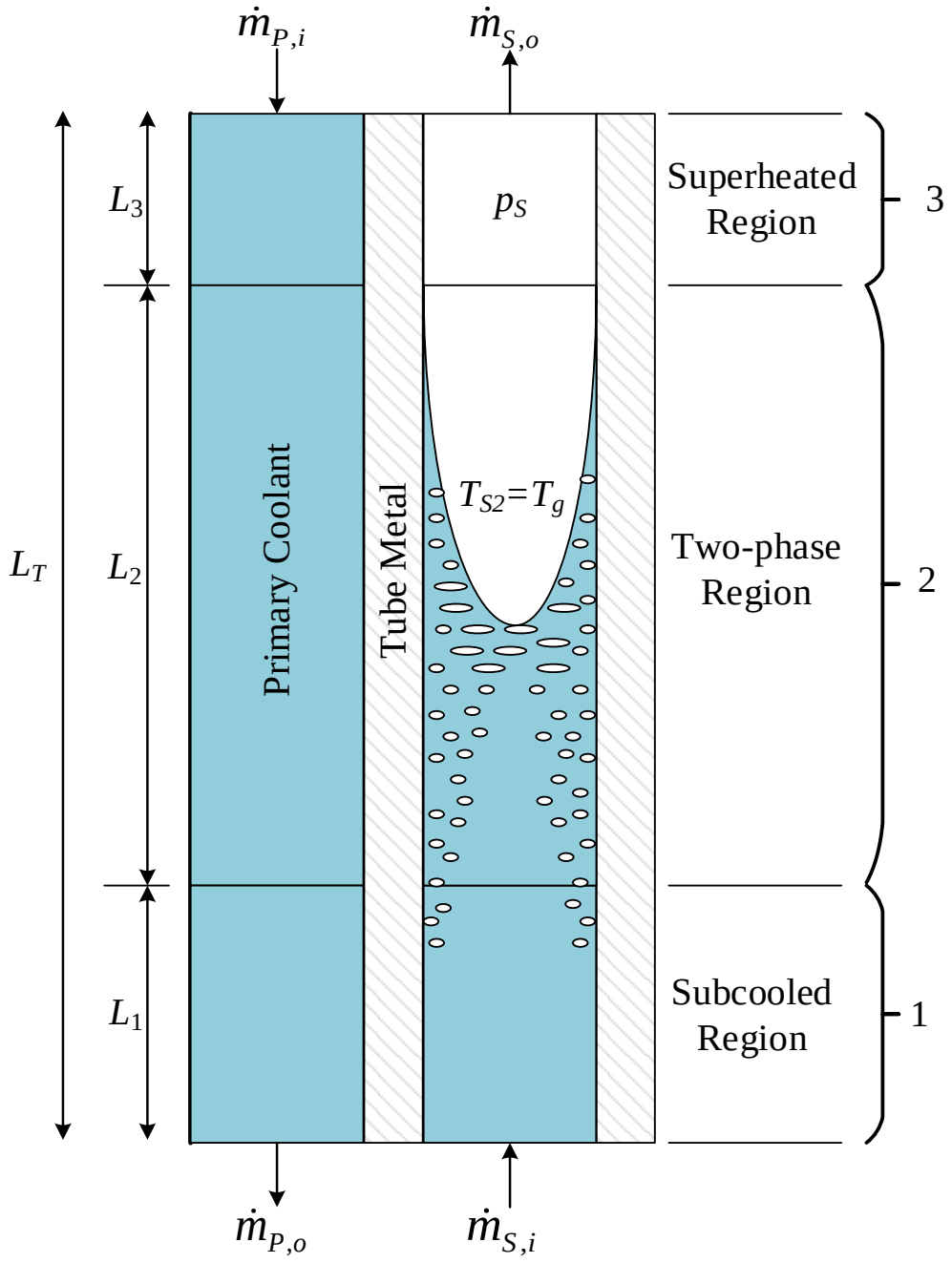

Figure 3.3 Schematic diagram of helical-coil steam generator model.

The fundamental assumptions made to simplify the model development are listed below:

- Tubes inside the steam generator have identical flow. As such, a single tube heat exchanger concept is used for simulating the dynamic behavior of the steam generator.
- One-dimensional fluid flow is utilized for both primary and secondary sides.
- Perfect feedwater control is assumed, that is, feedwater and steam mass flow rates are equal.
- Heat conductivity along the axial direction is negligible.
- Primary and secondary side pressures are assumed to be uniform.
- The two-phase region is in thermal equilibrium.

He et al. [53] provide governing one-dimensional partial differential equations for the conservation of mass and energy (Equations (3.24) and (3.25)) which are applicable to all regions of the secondary side as well as an energy balance (Equation (3.26)) for the tube metal

$$\frac{\partial A_S \rho}{\partial t} + \frac{\partial \dot{m}_S}{\partial z} = 0 \tag{3.24}$$

$$\frac{\partial \left(A_S \rho h - A_S p\right)}{\partial t} + \frac{\partial \dot{m}_S h}{\partial z} = \pi d_i \alpha_i \left(T_M - T_S\right) \tag{3.25}$$

$$c_{p,M} \rho A_M \frac{\partial T_M}{\partial t} = \pi d_i \alpha_i \left(T_S - T_M\right) + \pi d_o \alpha_o \left(T_P - T_M\right) \tag{3.26}$$

The variables will be explicitly defined in the following sections. He et al. were modeling vapor compression cycles with an air heat sink, but this SMR steam generator requires a primary side energy balance of the form

$$c_{p,P}\rho A_P \frac{\partial T_P}{\partial t} = c_{p,P}\dot{m}_P\left(T_{Pi} - T_P\right) + \pi d_o \alpha_o \left(T_M - T_P\right) \tag{3.27}$$

The above conservation equations are integrated over each region and then *Leibnitz theorem* [54], which, is given by Equation (3.28), is applied to obtain a set of ordinary differential equations.

$$\int_{a(t)}^{b(t)} \frac{\partial f(z,t)}{\partial t} dz = \frac{d}{dt}\int_{a(t)}^{b(t)} f(z,t)dz - f\left(b(t),t\right)\frac{db(t)}{dt} + f\left(a(t),t\right)\frac{da(t)}{dt} \tag{3.28}$$

3.3.2 Secondary side equations

In this section, only final forms of mass and energy balance equations for all secondary side regions are presented with aim of providing an insight. Readers interested in the intermediate steps can refer to Appendix B.1.

3.3.2.1 Subcooled region mass and energy balance

Integrating mass and energy balance equations for the subcooled region yields

$$A_S\left\{(\rho_1 - \rho_f)\frac{dL_1}{dt} + L_1\left(\left.\frac{\partial \rho_1}{\partial p_S}\right|_{h_1} + \frac{1}{2}\left.\frac{\partial \rho_1}{\partial h_1}\right|_{p_S}\frac{\partial h_f}{\partial p_S}\right)\frac{dp_S}{dt} + \frac{1}{2}L_1\left.\frac{\partial \rho_1}{\partial h_1}\right|_{p_S}\frac{dh_i}{dt}\right\} = \dot{m}_{S,i} - \dot{m}_{S,12} \tag{3.29}$$

$$\begin{aligned} &A_S\left\{(\rho_1 h_1 - \rho_f h_f)\frac{dL_1}{dt} + \frac{1}{2}L_1\left(\rho_1 + h_1\left.\frac{\partial \rho_1}{\partial h_1}\right|_{p_S}\right)\frac{dh_i}{dt} + \right. \\ &\left. L_1\left(\frac{\rho_1}{2}\frac{\partial h_f}{\partial p_S} + h_1\left(\left.\frac{\partial \rho_1}{\partial p_S}\right|_{h_1} + \frac{1}{2}\left.\frac{\partial \rho_1}{\partial h_1}\right|_{p_S}\frac{\partial h_f}{\partial p_S}\right) - 1\right)\frac{dp_S}{dt}\right\} = \dot{m}_{S,i}h_i - \dot{m}_{S,12}h_f + \pi d_i \alpha_{i1}(T_{M1} - T_{S1}) \end{aligned} \tag{3.30}$$

where A_S is the cross-sectional flow area inside the tube; ρ with subscripts (1) and (f) standing for the average density of the liquid inside the subcooled region and saturated liquid density, respectively; L_1 is the length of the subcooled region; p_S is the steam pressure; h_i, h_1, and h_f are feedwater inlet enthalpy, average enthalpy for the subcooled region and saturated enthalpy, respectively; $\dot{m}_S$ represents the secondary mass flow rate at the steam generator inlet (i) and at the interface of regions 1 and 2 (12); d_i is the tube inner diameter; α_{i1} is the region 1 heat transfer coefficient between the secondary side and tube metal; and finally, T with the related subscripts are tube metal ($M1$) and feedwater ($S1$) temperatures corresponding to the subcooled region.

3.3.2.2 Two-phase region mass and energy balance

Final forms of the mass and energy balance equations for two-phase region are given below:

$$A_S\left\{(\rho_f-\rho_g)\frac{dL_1}{dt}+(1-\bar{\gamma})(\rho_f-\rho_g)\frac{dL_2}{dt}+L_2\left(\bar{\gamma}\frac{\partial\rho_g}{\partial p_S}+(1-\bar{\gamma})\frac{\partial\rho_f}{\partial p_S}\right)\frac{dp_S}{dt}\right\}=\dot{m}_{S,12}-\dot{m}_{S,23} \quad (3.31)$$

$$A_S\left\{(\rho_f h_f-\rho_g h_g)\frac{dL_1}{dt}+(1-\bar{\gamma})(\rho_f h_f-\rho_g h_g)\frac{dL_2}{dt}+\right.$$
$$\left.L_2\left(\bar{\gamma}\frac{\partial(\rho_g h_g)}{\partial p_S}+(1-\bar{\gamma})\frac{\partial(\rho_f h_f)}{\partial p_S}-1\right)\frac{dp_S}{dt}\right\}=\dot{m}_{S,12}h_f-\dot{m}_{S,23}h_g+\pi d_i\alpha_{i2}(T_{M2}-T_{S2}) \quad (3.32)$$

where ρ_g and h_g are saturated vapor density and enthalpy, respectively; $\bar{\gamma}$ is the mean void fraction inside the two-phase region; L_2 is the length of the two-phase region; $\dot{m}_{S,23}$ is the mass flow rate at the interface of regions 2 and 3; α_{i2} is the region 2 heat transfer

coefficient between secondary side and tube metal; T_{M2} is the tube metal temperature at the two-phase region; and T_{S2} equals the saturation temperature (T_{sat}) at a given pressure.

3.3.2.3 Superheated region mass and energy balance

The same approach is followed for the superheated region and the resulting equations for mass and energy balance are

$$A_S\left\{(\rho_g-\rho_3)\frac{d(L_1+L_2)}{dt}+L_3\left(\left.\frac{\partial\rho_3}{\partial p_S}\right|_{h_3}+\frac{1}{2}\left.\frac{\partial\rho_3}{\partial h_3}\right|_{p_S}\frac{\partial h_g}{\partial p_S}\right)\frac{dp_S}{dt}+\frac{1}{2}L_3\left.\frac{\partial\rho_3}{\partial h_3}\right|_{p_S}\frac{dh_o}{dt}\right\}=\dot{m}_{S,23}-\dot{m}_{S,o} \quad (3.33)$$

$$\begin{aligned}&A_S\left\{(\rho_g h_g-\rho_3 h_3)\frac{d(L_1+L_2)}{dt}+\frac{1}{2}L_3\left(\rho_3+h_3\left.\frac{\partial\rho_3}{\partial h_3}\right|_{p_S}\right)\frac{dh_o}{dt}+\right.\\&\left.L_3\left(\frac{\rho_3}{2}\frac{\partial h_g}{\partial p_S}+h_3\left(\left.\frac{\partial\rho_3}{\partial p_S}\right|_{h_3}+\frac{1}{2}\left.\frac{\partial\rho_3}{\partial h_3}\right|_{p_S}\frac{\partial h_g}{\partial p_S}\right)-1\right)\frac{dp_s}{dt}\right\}=\dot{m}_{S,23}h_g-\dot{m}_{S,o}h_o+\pi d_i\alpha_{i3}(T_{M3}-T_{S3})\end{aligned} \quad (3.34)$$

where ρ_3 is the average density of vapor inside the superheated region; L_3 is the length of the superheated region; h_o and h_3 are the steam outlet enthalpy and average enthalpy for the superheated region; $\dot{m}_{S,o}$ is the steam flow rate at the outlet of the steam generator; α_{i3} is the region 3 heat transfer coefficient between secondary side and tube metal; and T with the related subscripts are tube metal ($M3$) and steam ($S3$) temperatures corresponding to the superheated region.

3.3.3 Tube metal equations

An average temperature model, in which the temperature at each boundary is the mean value of temperatures of adjacent wall regions, is utilized to observe the dynamics.

Then the energy conservation equations corresponding to regions of the secondary side are given by

$$A_M \rho_M c_{p,M} L_1 \frac{dT_{M1}}{dt} + A_M \rho_M c_{p,M} (T_{M1} - T_{M2}) \frac{dL_1}{dt} = \pi L_1 \left[d_o \alpha_{o1} (T_{P1} - T_{M1}) - d_i \alpha_{i1} (T_{M1} - T_{S1}) \right] \quad (3.35)$$

$$A_M \rho_M c_{p,M} L_2 \frac{dT_{M2}}{dt} = \pi L_2 \left[d_o \alpha_{o2} (T_{P2} - T_{M2}) - d_i \alpha_{i2} (T_{M2} - T_{S2}) \right] \quad (3.36)$$

$$A_M \rho_M c_{p,M} L_3 \frac{dT_{M3}}{dt} + A_M \rho_M c_{p,M} (T_{M2} - T_{M3}) \frac{d(L_1 + L_2)}{dt} = \pi L_3 \left[d_o \alpha_{o3} (T_{P3} - T_{M3}) - d_i \alpha_{i3} (T_{M3} - T_{S3}) \right] \quad (3.37)$$

where A_M, ρ_M, and $c_{p,M}$ are the cross-sectional area, density, and specific heat of the tube metal, respectively; d_o is the outer diameter of the tube metal; α_o represents the heat transfer coefficient between the primary side and tube metal for each region; T_{P2} and T_{P3} are the average temperatures of the primary coolant for regions 2 and 3, respectively.

3.3.4 Primary side equations

In a similar manner, the energy balance equations for the primary side are

$$A_P \rho_P c_{p,P} L_1 \frac{dT_{P1}}{dt} + A_P \rho_P c_{p,P} (T_{P1} - T_{P2}) \frac{dL_1}{dt} = \dot{m}_P c_{p,P} (T_{P2} - T_{P1}) - \pi d_o \alpha_{o1} L_1 (T_{P1} - T_{M1}) \quad (3.38)$$

$$A_P \rho_P c_{p,P} L_2 \frac{dT_{P2}}{dt} = \dot{m}_P c_{p,P} (T_{P3} - T_{P2}) - \pi d_o \alpha_{o2} L_2 (T_{P2} - T_{M2}) \quad (3.39)$$

$$A_P \rho_P c_{p,P} L_3 \frac{dT_{P3}}{dt} + A_P \rho_P c_{p,P} (T_{P2} - T_{P3}) \frac{d(L_1 + L_2)}{dt} = \dot{m}_P c_{p,P} (T_{Pi} - T_{P3}) - \pi d_o \alpha_{o3} L_3 (T_{P3} - T_{M3}) \quad (3.40)$$

where A_P is the cross-sectional area of the primary coolant flow channel; ρ_P, $c_{p,P}$, and $\dot{m}_P$ are the density, specific heat, and mass flow rate of the primary coolant; and T_{Pi} is the primary coolant temperature at the steam generator inlet.

3.3.5 Heat transfer coefficients and mean void fraction

In this study, the surface heat transfer coefficient for primary side is calculated by utilizing the correlation for a bank of tubes given by [51]

$$\mathrm{Nu} = B\,\mathrm{Re}^{b}\,\mathrm{Pr}^{0.36}\left(\frac{\mathrm{Pr}}{\mathrm{Pr}_s}\right)^{0.25} \quad \begin{bmatrix} n_L \geq 20 \\ 0.7 \leq \mathrm{Pr} \leq 500 \\ 1{,}000 \leq \mathrm{Re} \leq 2\times10^{6} \end{bmatrix} \tag{3.41}$$

where Nu is the Nusselt number; coefficients B (0.021) and b (0.84) are determined from a table in Reference [51] according to the configuration of tubes (aligned or staggered) and the value of the Reynolds number; Pr_s is the Prandtl number at the surface conditions; and n_L is the number of tubes in the bank.

For the surface heat transfer coefficient of the secondary side, a modified version of the *Dittus-Boelter correlation* [55], which is valid for single-phase heat convection, is used

$$\mathrm{Nu} = 0.023\,\mathrm{Re}^{0.85}\,\mathrm{Pr}^{0.4}\left(\frac{d_o}{d_C}\right)^{0.1} \quad \left[6{,}000 < \mathrm{Re} < 65{,}000\right] \tag{3.42}$$

where d_C is the coil diameter. The heat transfer coefficient for two-phase heat convection is determined by taking advantage of the known variables at initial steady-state condition for the two-phase region, i.e., the two-phase region length, the saturation temperature and the temperatures of the tube metal, and the heat delivered by the primary side.

The mean void fraction $\bar{\gamma}$ is calculated with the help of the correlation given by Jensen and Tummescheit [56]

$$\bar{\eta} = \frac{1+\left(\frac{1}{\mu}\right)^{0.66}\left[\frac{2}{3}\ln\left(\frac{1}{\mu}\right)-1\right]}{\left[\left(\frac{1}{\mu}\right)^{0.66}-1\right]^2} \tag{3.43}$$

where $\bar{\eta}$ is the mean liquid fraction and a relationship of $\bar{\eta}+\bar{\gamma}=1$ is valid; and μ is the ratio of the saturated vapor density to the saturated liquid density.

3.3.6 Steam valve equation

The steam flow rate through the turbine is controlled via a steam valve. An expression is adopted for the valve based on the assumption that the steam flow rate is only a function of the steam pressure and any pressure drop inside the turbine does not cause an increase in the flow rate. This is known as critical flow assumption [57]. The relation is then

$$\dot{m}_{S,o} = C_L\, p_S \tag{3.44}$$

where the constant steam valve coefficient C_L calculated from the relevant values under steady-state full power condition.

3.3.7 Steam generator state-space model

The twelve differential equations presented above (Equations (3.29)–(3.40)) incorporate only ten explicit derivative terms. Therefore, the relevant equations are combined and necessary algebraic alterations are made to eliminate $\dot{m}_{S,12}$ and $\dot{m}_{S,23}$ [58].

The resulting state vector is $\mathbf{x} = \begin{bmatrix} L_1 & L_2 & p_S & h_o & T_{M1} & T_{M2} & T_{M3} & T_{P1} & T_{P2} & T_{P3} \end{bmatrix}^T$ and the input vector $\mathbf{u} = \begin{bmatrix} \dot{m}_{S,i} & \dot{m}_{S,o} & h_i & T_{Pi} & \dot{m}_P \end{bmatrix}^T$. Then, it is possible to represent the steam generator model in the following state-space form

$$\dot{\mathbf{x}} = \mathbf{D}^{-1}(\mathbf{x},\mathbf{u})\mathbf{f}(\mathbf{x},\mathbf{u}) \tag{3.45}$$

where

$$\mathbf{D}(\mathbf{x},\mathbf{u}) = \begin{bmatrix} d_{1,1} & 0 & d_{1,3} & 0 & 0 & 0 & 0 & 0 & 0 & 0 \\ d_{2,1} & d_{2,2} & d_{2,3} & d_{2,4} & 0 & 0 & 0 & 0 & 0 & 0 \\ d_{3,1} & d_{3,2} & d_{3,3} & d_{3,4} & 0 & 0 & 0 & 0 & 0 & 0 \\ d_{4,1} & d_{4,2} & d_{4,3} & d_{4,4} & 0 & 0 & 0 & 0 & 0 & 0 \\ d_{5,1} & 0 & 0 & 0 & d_{5,5} & 0 & 0 & 0 & 0 & 0 \\ 0 & 0 & 0 & 0 & 0 & d_{6,6} & 0 & 0 & 0 & 0 \\ d_{7,1} & d_{7,2} & 0 & 0 & 0 & 0 & d_{7,7} & 0 & 0 & 0 \\ d_{8,1} & 0 & 0 & 0 & 0 & 0 & 0 & d_{8,8} & 0 & 0 \\ 0 & 0 & 0 & 0 & 0 & 0 & 0 & 0 & d_{9,9} & 0 \\ d_{10,1} & d_{10,2} & 0 & 0 & 0 & 0 & 0 & 0 & 0 & d_{10,10} \end{bmatrix}$$

$$\mathbf{f}(\mathbf{x},\mathbf{u}) = \begin{bmatrix} \dot{m}_{S,i}(h_i - h_f) + \pi d_i \alpha_{i1} L_1 (T_{M1} - T_{S1}) \\ \dot{m}_{S,i} h_f - \dot{m}_{S,o} h_g + \pi d_i \alpha_{i2} L_2 (T_{M2} - T_{S2}) \\ \dot{m}_{S,o}(h_g - h_o) + \pi d_i \alpha_{i3} L_3 (T_{M3} - T_{S3}) \\ \dot{m}_{S,i} - \dot{m}_{S,o} \\ \pi L_1 \left[d_o \alpha_{o1} (T_{P1} - T_{M1}) - d_i \alpha_{i1} (T_{M1} - T_{S1}) \right] \\ \pi L_2 \left[d_o \alpha_{o2} (T_{P2} - T_{M2}) - d_i \alpha_{i2} (T_{M2} - T_{S2}) \right] \\ \pi L_3 \left[d_o \alpha_{o3} (T_{P3} - T_{M3}) - d_i \alpha_{i3} (T_{M3} - T_{S3}) \right] \\ \dot{m}_P c_{p,P} (T_{P2} - T_{P1}) - \pi d_o \alpha_{o1} L_1 (T_{P1} - T_{M1}) \\ \dot{m}_P c_{p,P} (T_{P3} - T_{P2}) - \pi d_o \alpha_{o2} L_2 (T_{P2} - T_{M2}) \\ \dot{m}_P c_{p,P} (T_{Pi} - T_{P3}) - \pi d_o \alpha_{o3} L_3 (T_{P3} - T_{M3}) \end{bmatrix}$$

The elements of **D(x,u)** are in given in Table 3.2.

Table 3.2 Elements of matrix **D**(**x**,**u**)

Index	Element
$d_{1,1}$	$A_S \rho_1 (h_1 - h_f)$
$d_{1,3}$	$A_S L_1 \left[\left(\left. \frac{\partial \rho_1}{\partial p_S} \right\|_{h_1} + \frac{1}{2} \left. \frac{\partial \rho_1}{\partial h_1} \right\|_{p_S} \frac{\partial h_f}{\partial p_S} \right) (h_1 - h_f) + \frac{\rho_1}{2} \frac{\partial h_f}{\partial p_S} - 1 \right]$
$d_{2,1}$	$A_S (\rho_1 h_f - \rho_3 h_g)$
$d_{2,2}$	$A_S [(1-\bar{\gamma})(\rho_f h_f - \rho_g h_g) + h_g (\rho_g - \rho_3)]$
$d_{2,3}$	$A_S \left[h_f L_1 \left(\left. \frac{\partial \rho_1}{\partial p_S} \right\|_{h_1} + \frac{1}{2} \left. \frac{\partial \rho_1}{\partial h_1} \right\|_{p_S} \frac{\partial h_f}{\partial p_S} \right) + L_2 \left(\bar{\gamma} \frac{\partial (\rho_g h_g)}{\partial p_S} + (1-\bar{\gamma}) \frac{\partial (\rho_f h_f)}{\partial p_S} - 1 \right) + h_g L_3 \left(\left. \frac{\partial \rho_3}{\partial p_S} \right\|_{h_3} + \frac{1}{2} \left. \frac{\partial \rho_3}{\partial h_3} \right\|_{p_S} \frac{\partial h_g}{\partial p_S} \right) \right]$
$d_{2,4}$	$\frac{A_S h_g L_3}{2} \left(\left. \frac{\partial \rho_3}{\partial h_3} \right\|_{p_S} \right)$
$d_{3,1}$	$A_S \rho_3 (h_g - h_3)$
$d_{3,2}$	$A_S \rho_3 (h_g - h_3)$
$d_{3,3}$	$A_S L_3 \left[\left(\left. \frac{\partial \rho_3}{\partial p_S} \right\|_{h_3} + \frac{1}{2} \left. \frac{\partial \rho_3}{\partial h_3} \right\|_{p_S} \frac{\partial h_g}{\partial p_S} \right) (h_3 - h_g) + \frac{\rho_{31}}{2} \frac{\partial h_g}{\partial p_S} - 1 \right]$
$d_{3,4}$	$A_S L_3 \left[\frac{1}{2} \left(\left. \frac{\partial \rho_3}{\partial h_3} \right\|_{p_S} \right) (h_3 - h_g) + \frac{\rho_3}{2} \right]$
$d_{4,1}$	$A_S (\rho_1 - \rho_3)$
$d_{4,2}$	$A_S [(1-\bar{\gamma})(\rho_f - \rho_g) + (\rho_g - \rho_3)]$
$d_{4,3}$	$A_S \left[L_1 \left(\left. \frac{\partial \rho_1}{\partial p_S} \right\|_{h_1} + \frac{1}{2} \left. \frac{\partial \rho_1}{\partial h_1} \right\|_{p_S} \frac{\partial h_f}{\partial p_S} \right) + L_2 \left(\bar{\gamma} \frac{\partial \rho_g}{\partial p_S} + (1-\bar{\gamma}) \frac{\partial \rho_f}{\partial p_S} \right) + L_3 \left(\left. \frac{\partial \rho_3}{\partial p_S} \right\|_{h_3} + \frac{1}{2} \left. \frac{\partial \rho_3}{\partial h_3} \right\|_{p_S} \frac{\partial h_g}{\partial p_S} \right) \right]$
$d_{4,4}$	$\frac{A_S L_3}{2} \left(\left. \frac{\partial \rho_3}{\partial h_3} \right\|_{p_S} \right)$

$d_{5,1}$	$A_M \rho_M c_{p,M} (T_{M1} - T_{M2})$
$d_{5,5}$	$A_M \rho_M c_{p,M} L_1$
$d_{6,6}$	$A_M \rho_M c_{p,M} L_2$
$d_{7,1}$	$A_M \rho_M c_{p,M} (T_{M2} - T_{M3})$
$d_{7,2}$	$A_M \rho_M c_{p,M} (T_{M2} - T_{M3})$
$d_{7,7}$	$A_M \rho_M c_{p,M} L_3$
$d_{8,1}$	$A_P \rho_P c_{p,P} (T_{P1} - T_{P2})$
$d_{8,8}$	$A_P \rho_P c_{p,P} L_1$
$d_{9,9}$	$A_P \rho_P c_{p,P} L_2$
$d_{10,1}$	$A_P \rho_P c_{p,P} (T_{P2} - T_{P3})$
$d_{10,2}$	$A_P \rho_P c_{p,P} (T_{P2} - T_{P3})$
$d_{10,10}$	$A_P \rho_P c_{p,P} L_3$

3.4 Pressurizer Model

Unlike the traditional PWR pressurizer, which is a separate cylindrical tank connected to the reactor coolant system piping by a surge line, an SMR integrates the pressurizer into the top of the reactor pressure vessel. In addition, the pressurizer volume in an integral SMR is considerably larger than the volume of the typical PWR pressurizer relative to reactor thermal power. The larger pressurizer volume coupling with the larger primary coolant system results in slower pressure transients during normal operating conditions. Finally, continuous spray, employed in large PWRs to insure the line does not clog, is eliminated in many SMR design. Instead, a spray line, similar to the auxiliary

spray in larger PWRs, is employed and designed to reduce the pressure when needed [59].

The pressurizer model, as depicted in Figure 3.4, consists of two regions [34]: (1) liquid, and (2) vapor. The following assumptions are carried out to simply the modelling:

- Water-steam inside the pressurizer section is always at saturated conditions corresponding to the primary coolant pressure.
- Heat losses are neglected.
- No condensation on the vessel wall or liquid surface.

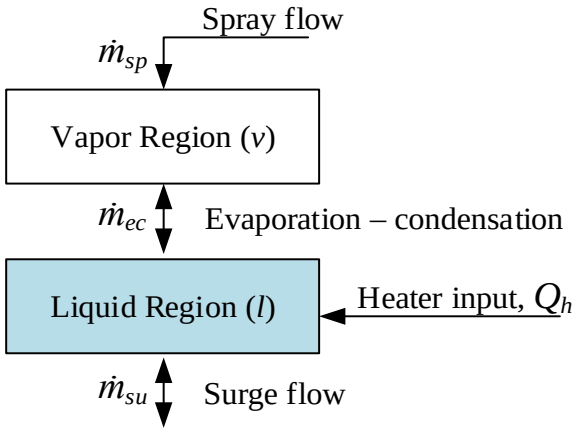

Figure 3.4 Schematic diagram of pressurizer model.

Mass, energy, and volume balance equations for the pressurizer model are presented as follows:

mass balances:

$$\frac{dm_l}{dt} = \dot{m}_{su} + \dot{m}_{sp} - \dot{m}_{ec} \tag{3.46}$$

$$\frac{dm_v}{dt} = \dot{m}_{ec} \tag{3.47}$$

For above equations, condensation occurs if $\dot{m}_{ec} < 0$ while $\dot{m}_{ec} > 0$ indicates that evaporation takes place. In similar manner, $\dot{m}_{su} > 0$ accounts for surge flow into the pressurizer, whereas $\dot{m}_{su} < 0$ means that the surge flow is out of the pressurizer.

volume balance:

$$V_T = V_l + V_v = m_l \upsilon_f + m_v \upsilon_g \tag{3.48}$$

energy balances:

$$\frac{dE_l}{dt} = Q_h + \dot{m}_{su} h + \dot{m}_{sp} h_{DR} - \dot{m}_{ec} h_g - p\frac{dV_l}{dt} \tag{3.49}$$

$$\frac{dE_v}{dt} = \dot{m}_{ec} h_g - p\frac{dV_v}{dt} \tag{3.50}$$

where m_l and m_v are the masses of the liquid and vapor in the pressurizer section; $\dot{m}$ with associated subscript gives surge flow (*su*), spray flow (*sp*), and evaporation-condensation (*ec*) rates; V_T represents the total volume of the pressurizer (constant) comprised of liquid and vapor volumes; E_l and E_v denote energies of liquid and vapor; similarly, the products of $p(dV/dt)$ represent flow work of liquid and vapor; Q_h is the heat given by electric heaters; h_{DR} is the primary coolant enthalpy in the downcomer region, and in the case of insurge $h = h_{HL}$ (primary coolant enthalpy in the hot leg riser) otherwise $h = h_f$ (saturated liquid enthalpy); and finally, h_g is the saturated vapor enthalpy corresponding to primary coolant pressure.

Since saturated conditions are always assumed to be preserved inside the pressurizer, it is possible to derive following equalities for temperature and pressure

$$T_l = T_v = T_{sat} \tag{3.51}$$

$$p_p = p_l = p_v = p_{sat} \tag{3.52}$$

where the subscripts *p*, *l*, *v*, and *sat* stand for pressurizer, liquid, vapor, and saturation. The pressurizer pressure is about 0.35 MPa less than the primary pressure due to the difference in the elevation; see Figure 3.2. With the help of above equalities, the pressurizer pressure equation is obtained after several algebraic manipulations.

$$m_l\left(\frac{\partial h_f}{\partial p_P} - \upsilon_f\right)\frac{dp_p}{dt} = Q_h + \dot{m}_{su}(h - h_f) + \dot{m}_{sp}(h_{DR} - h_f) - \dot{m}_{ec}(h_{fg}) \tag{3.53}$$

where $h_{fg} = h_g - h_f$. Equation (3.48) is combined with an equation of state, in this case the ideal gas law ($p_P V_v = m_v R T_{sat}$), to obtain an expression for the condensation-evaporation rate which is

$$\dot{m}_{ec} = \frac{1}{A}\frac{dp_p}{dt} - \frac{B}{A}\frac{dm_l}{dt} \tag{3.54}$$

where $$A = \frac{RT_{sat}}{V_v - Rm_v\dfrac{\partial T_{sat}}{\partial p_p} - p_p m_l \dfrac{\partial \upsilon_f}{\partial p_p}} \qquad B = \frac{p_p \upsilon_f}{V_v - Rm_v\dfrac{\partial T_{sat}}{\partial p_p} - p_p m_l \dfrac{\partial \upsilon_f}{\partial p_p}}$$

Substituting Equations (3.46) and (3.53) into Equation (3.54) and applying necessary alteration yields the final equation below for the pressurizer pressure.

$$\left[m_l \left(\frac{\partial h_f}{\partial p_P} - \upsilon_f \right) + \frac{h_{fg}}{A} + \frac{B}{A} \left(\frac{h_{fg}}{A-B} \right) \right] \frac{dp_p}{dt} = Q_h + \dot{m}_{su} \left(h - h_f + \frac{B}{A-B} h_{fg} \right) + \dot{m}_{sp} \left(h_{DR} - h_f + \frac{B}{A-B} h_{fg} \right) \tag{3.55}$$

Finally, the summation of expansion (or contraction) of the water inside each primary coolant section comprises the change in insurge (or outsurge) term [60] that is

$$\delta \dot{m}_{su} = -\sum_{i=1}^{n} V_i \vartheta_i \frac{d\delta T_i}{dt} \tag{3.56}$$

where V_i is the volume, T_i is the temperature, and ϑ_i is the slope of the primary coolant density versus T_i for the i-th section.

3.5 Single SMR Unit model

The developed models are combined with a steam turbine representation, which outputs the maximum attainable power P_m based on the steam properties, pressure and enthalpy, and steam flow rate, to constitute a single SMR unit.

$$P_m = \eta_{Turb} \dot{m}_{S,o} \Delta h \tag{3.57}$$

where η_{Turb} represents the turbine efficiency (0.83) [61]; and Δh is the steam enthalpy difference between the turbine inlet and outlet.

The overall nonlinear system of coupled differential equations is introduced in the form of a state-space model. The variables P, C, T_F, T_{C1}, T_{C2}, T_{HL}, T_{DR}, L_1, L_2, p_S, h_o, T_{M1}, T_{M2}, T_{M3}, T_{P1}, T_{P2}, T_{P3}, p_p are selected as the state variables, ρ_{ext}, Q_h, C_L and T_{Si} are selected as the four input variables. The feedwater inlet temperature (T_{Si}) is obtained from the enthalpy h_i. Then, the differential equations, Equations (3.1), (3.2), (3.4), (3.5), (3.6),

(3.22), (3.23), (3.45), and (3.55), form the state equations. The combination of these state equations with algebraic equations, Eqs. (3.20), (3.44), and (3.56), constitute the overall reactor model.

The reactor model is implemented in MATLAB/Simulink [62], which is a user-friendly graphical programming environment for modeling, simulation and analysis of dynamic systems (see Figure 3.5).

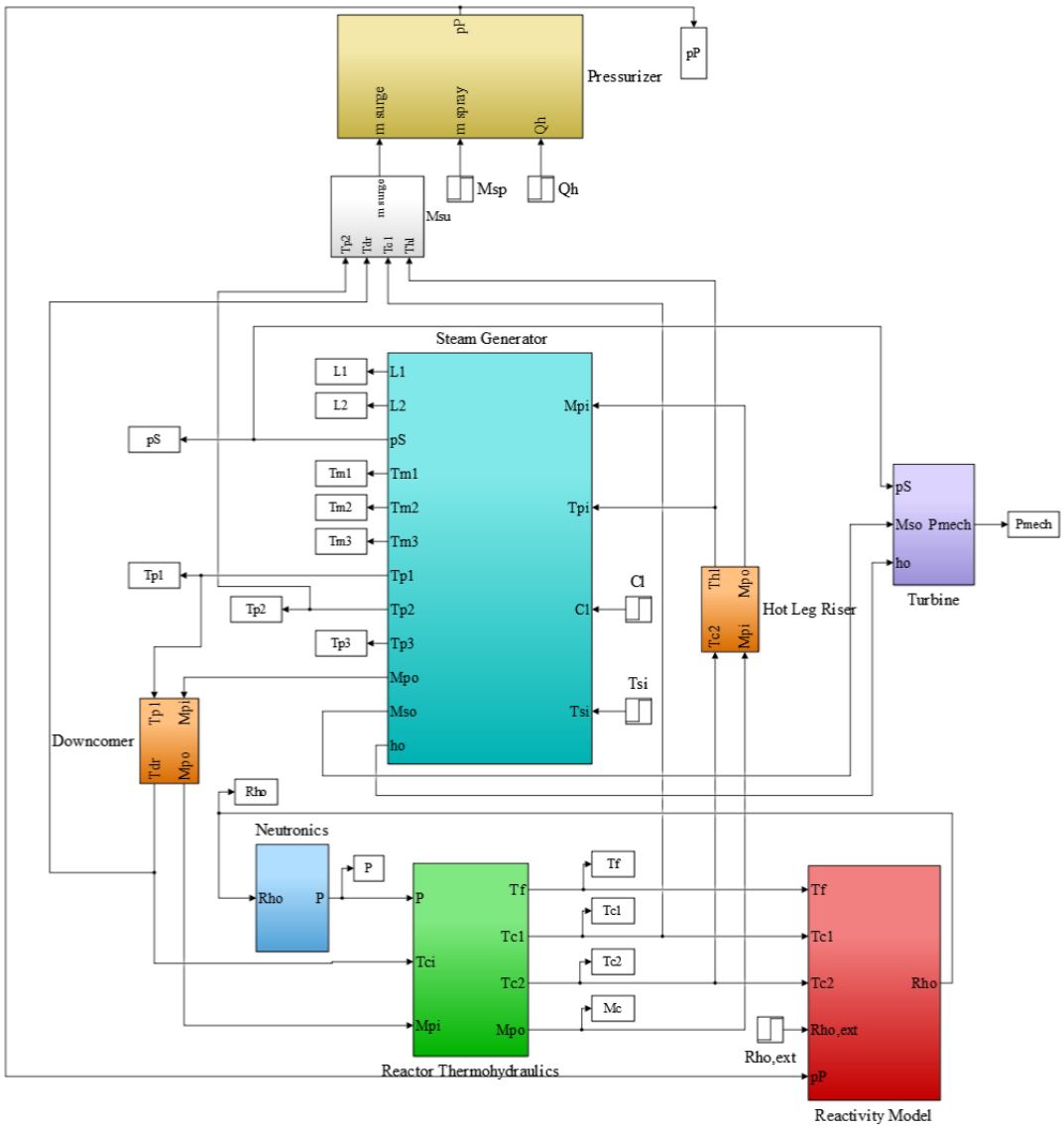

Figure 3.5 Simulink representation of overall reactor model.

3.6 Control Systems

3.6.1 Reactor control

The control of a reactor can be accomplished by three different modes in a PWR, any one of which alters reactor thermal power in accordance with changes in certain parameters, i.e., average primary coolant system temperature (T_{avg}), and steam pressure (p_S) [63].

3.6.1.1 Constant-average-temperature control mode

In this control mode, it is desired to keep the average temperature of the reactor coolant system (RCS) constant regardless of the power output. In the case of an increase in the load, the primary coolant average temperature decreases since the turbine extracts more energy from the primary system. The control system, then, senses the change in the RCS temperature and increases the system reactivity by withdrawing control rods. This control mode is in compliance with the natural behavior of a reactor with negative reactivity feedback coefficients and requires the least amount of control action.

The disadvantage of this program is that large variations in steam pressure and temperature occur, assuming the steam valve position is fixed, which is not preferred by the secondary system. However, it is preferred by the reactor since the constant-average-temperature control mode minimizes required pressurizer size because the volume of the water in the NSSS basically does not change. Figure 3.6 provides a depiction of this control mode.

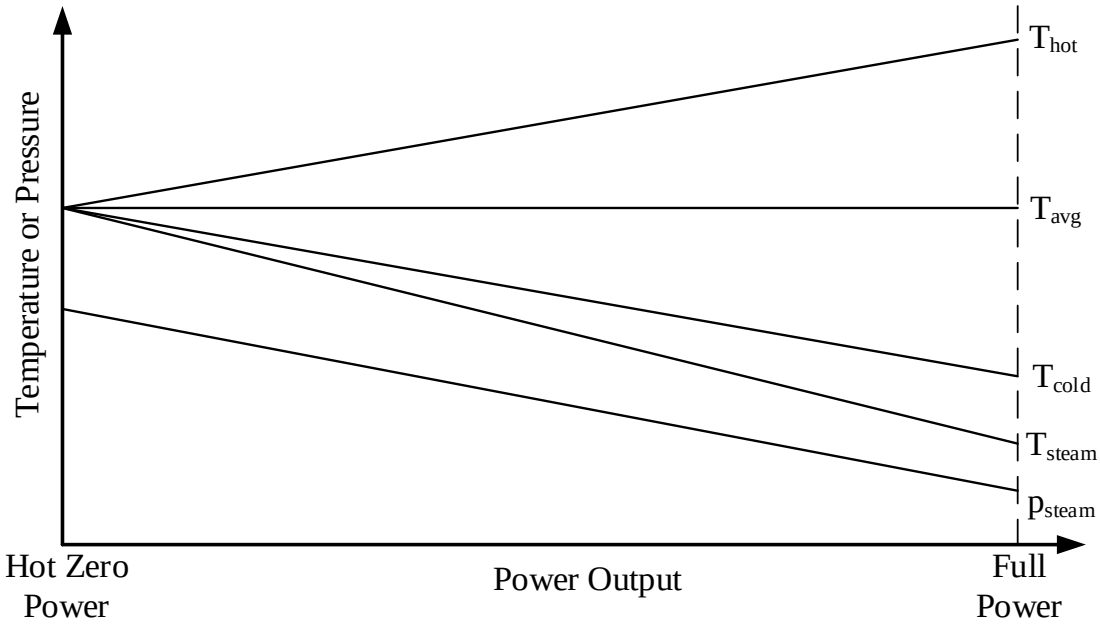

Figure 3.6 Characteristics of constant-average-temperature control model.

3.6.1.2 Constant-steam-pressure control mode

With this control mode, the reactivity of the reactor core is adjusted to maintain a constant secondary pressure as the turbine load is changed. This control scheme causes a rise in the temperature difference between primary and secondary sides by allowing the average RCS temperature to increase in order to keep the steam pressure constant (see Figure 3.7). The turbine favors the constant-steam-pressure control mode since excellent steam conditions are provided. Furthermore, some problems associated with automatic throttling devices and feedwater pumps are eliminated [64]. On the other hand, excessive control rod motion is required and the hot leg temperature can approach the saturation value corresponding to the primary coolant system pressure.

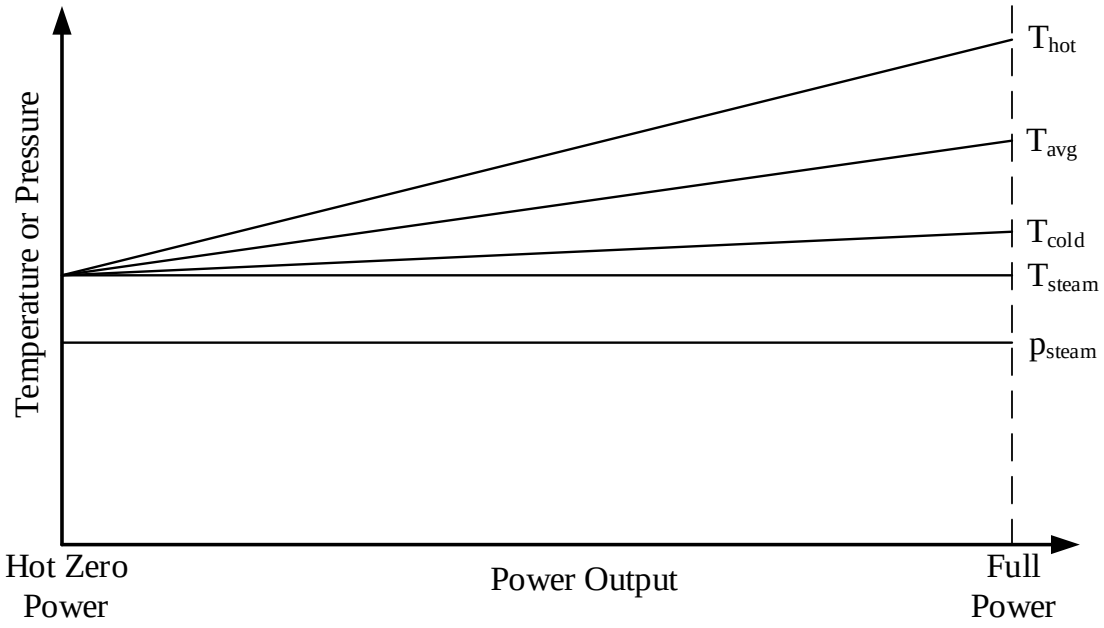

Figure 3.7 Characteristics of a constant-steam-pressure control mode.

3.6.1.3 Sliding-average-temperature control mode

For a slightly different mode from the aforementioned ones, the cold leg temperature (or downcomer temperature) is kept constant which lets the average and hot leg temperatures increase as the power output increases. The advantage of this program over the constant-average-temperature program is that the change in the steam pressure according to the power level is diminished. This program is also termed as a compromise program or non-constant program since it is intended to provide a balance between the needs of the primary and secondary systems. The relationship between temperatures and steam pressure for this control mode is illustrated in Figure 3.8 [65].

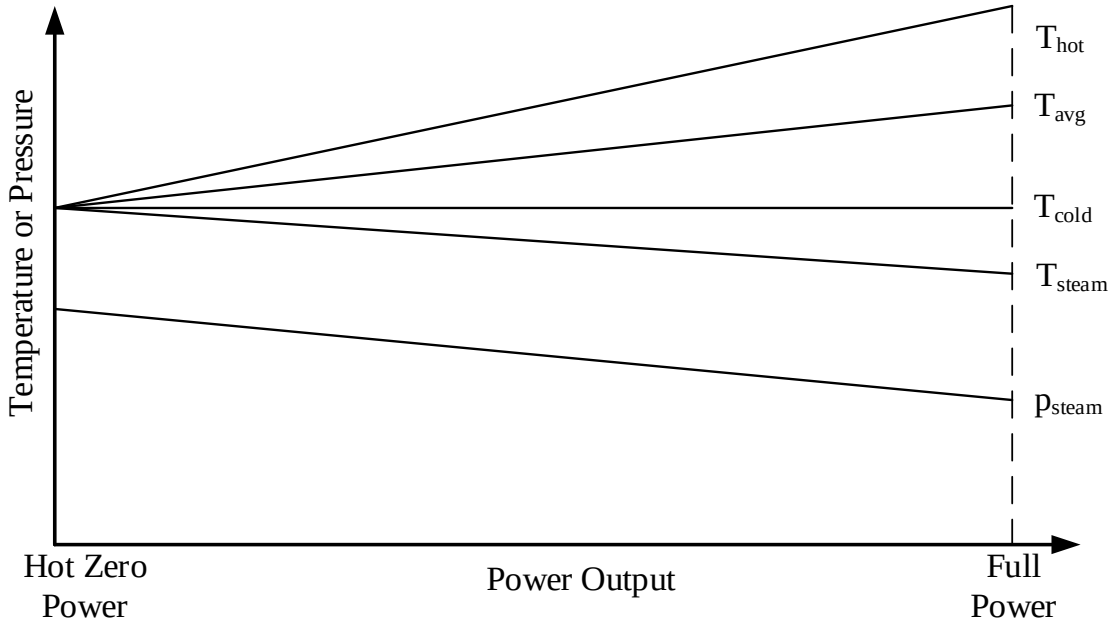

Figure 3.8 Characteristics of a sliding-average-temperature control mode.

As a final note, most large PWRs utilizes a sliding-average-temperature program [66] and for this reason, the same approach is adopted in this study. The control action in this mode is achieved by a proportional-integral (PI) transfer function which takes the mismatch between the setpoint and actual value of the cold leg temperature as the input and produces a positive or negative external reactivity depending on the polarity and magnitude of the mismatch, see Figure 3.9 and Equation (3.58).

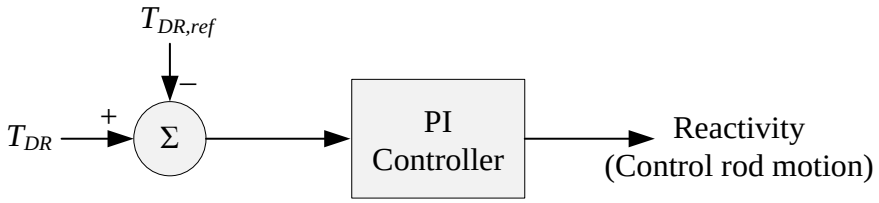

Figure 3.9 Block diagram of sliding-average-temperature controller.

$$\delta\rho_{ext} = \left[K_{P,T} + \frac{K_{I,T}}{s} \right] \left(T_{DR} - T_{DR,ref} \right) \tag{3.58}$$

where $T_{DR,ref}$ is the reference value of the downcomer temperature; $K_{P,T}$ and $K_{I,T}$ are the proportional and integral gain, respectively.

3.6.2 Primary coolant system pressure control

The control of the primary coolant system pressure is achieved by a bank of heaters which compensate steady-state heat losses from the pressurizer and also regulate the pressure under normal operating conditions. If the pressure is low, more power is applied to the heaters to increase the pressure, and in the case of high pressure, the power input to the heaters is decreased accordingly. When the pressure is below the control range, then, additional (auxiliary) heaters are turned on. For the reverse situation in which the pressure is too high and decreasing the heater power level is not sufficient, a spray flow from the chemical and volume control system provides cooling and reduces the pressure.

The controller model used in this study is a proportional-integral-derivative (PID) controller given by Figure 3.10 and Equation (3.59) and only acts on the normally operated heaters to keep the reactor coolant pressure constant.

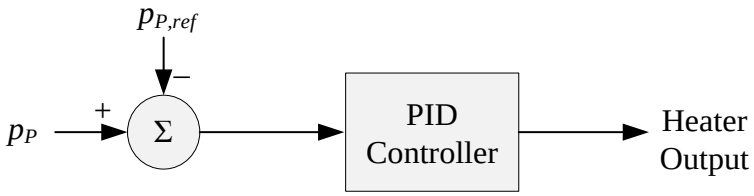

Figure 3.10 Block diagram of pressurizer pressure controller.

$$\delta Q_h = \left[K_{P,p} + \frac{K_{I,p}}{s} + K_{D,p} s \right] \left(p_P - p_{P,ref} \right) \tag{3.59}$$

where $p_{P,ref}$ is the reference value of the primary coolant system pressure; $K_{P,p}$, $K_{I,p}$, and $K_{D,p}$ are the proportional, integral and derivative gain, respectively.

CHAPTER 4 TESTING THE DYMAMIC MODELS IN MATLAB/SIMULINK

In this chapter, the mathematical models discussed in the previous chapter are tested and evaluated with the help of Matlab/Simulink v8.5 by applying common disturbances to them. First, the dynamic simulation results for isolated core, steam generator, and pressurizer models are presented, and then the response of the combination of these models with hot leg riser and downcomer which constitute the single SMR unit is presented.

4.1 Isolated Reactor Core Model

In order to test the isolated core model, small perturbations to reactivity and core inlet coolant temperature are applied separately, and changes in the reactor thermal power, core fuel and coolant temperatures, primary coolant flow rate and system reactivity are demonstrated in Figures 4.1-4.6. The obtained results are compared to the results from References [33].

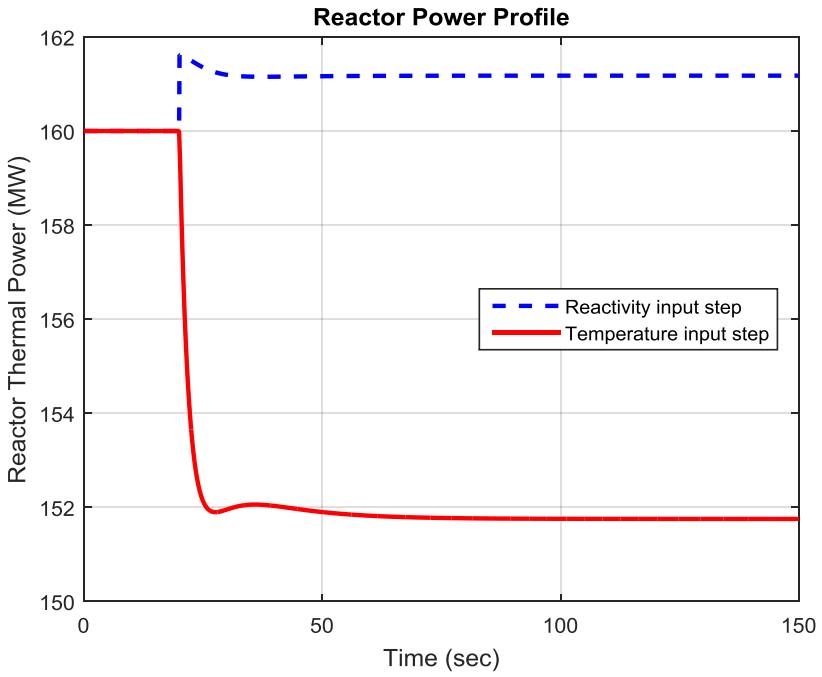

Figure 4.1 Reactor power (P) response to a step increase in the input variable for isolated reactor core model.

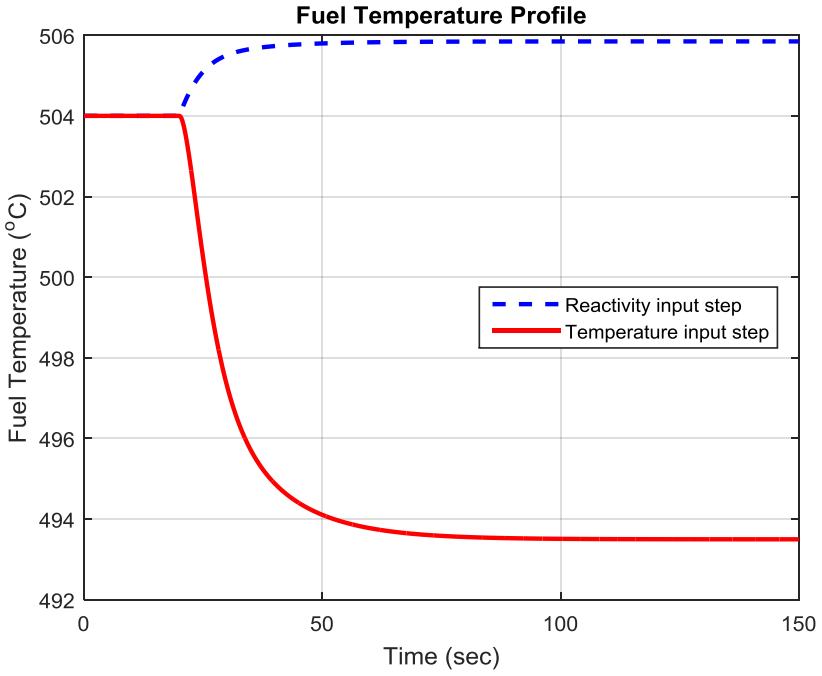

Figure 4.2 Fuel temperature (T_F) response to a step increase in the input variable for isolated reactor core model.

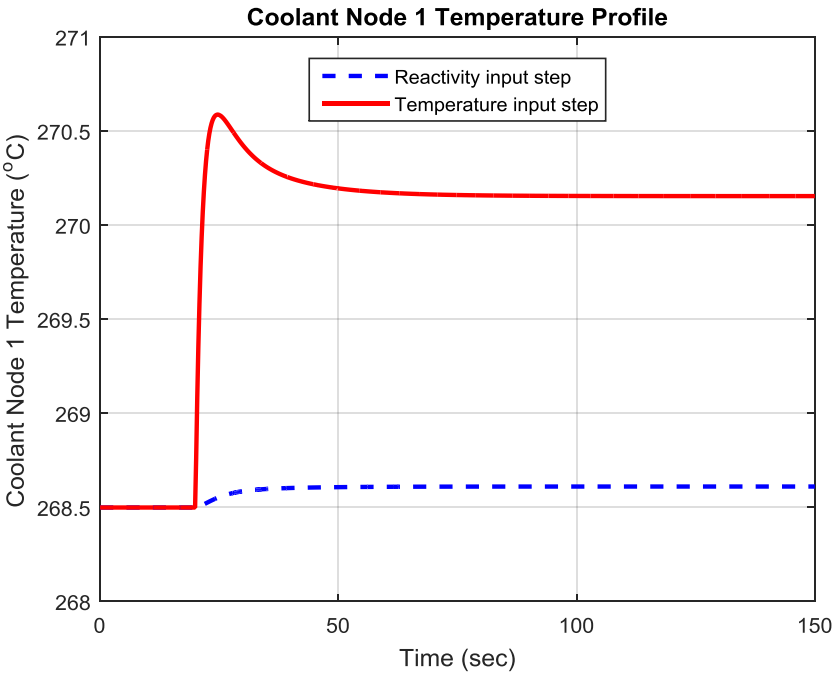

Figure 4.3 Reactor core coolant node 1 temperature (T_{C1}) response to a step increase in the input variable for isolated reactor core model.

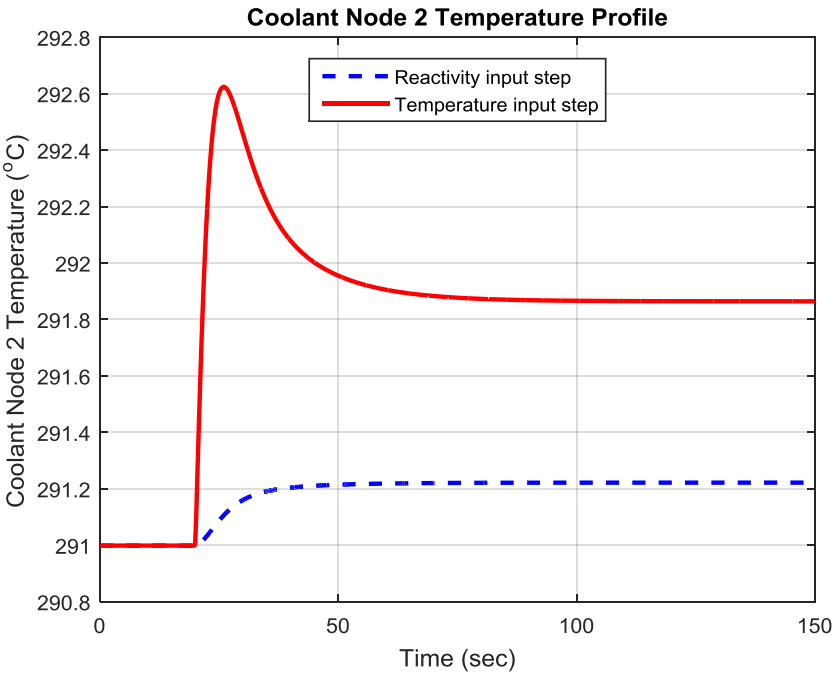

Figure 4.4 Reactor core coolant node 2 temperature (T_{C2}) response to a step increase in the input variable for isolated reactor core model.

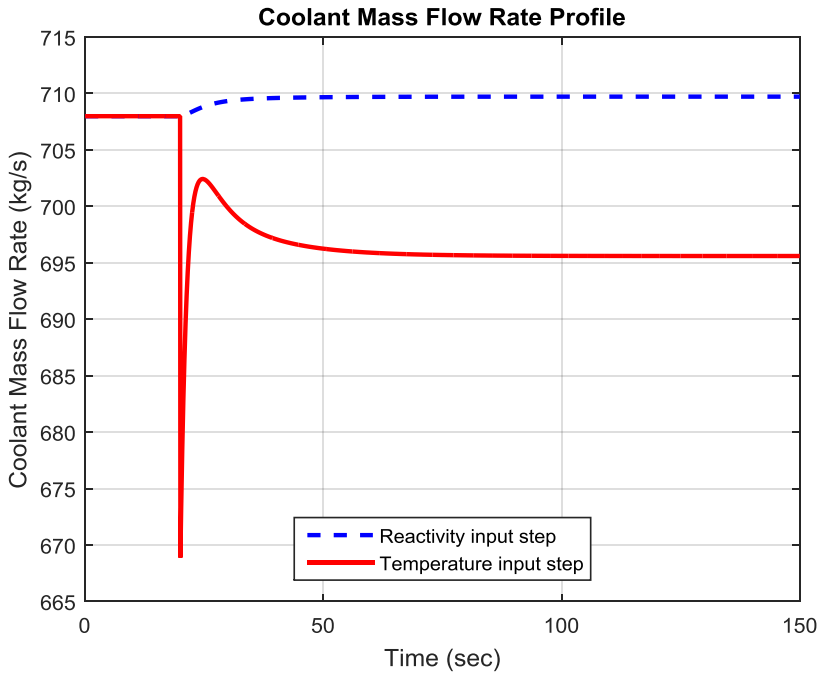

Figure 4.5 Primary coolant mass flow rate ($\dot{m}_C$) response to a step increase in the input variable for isolated reactor core model.

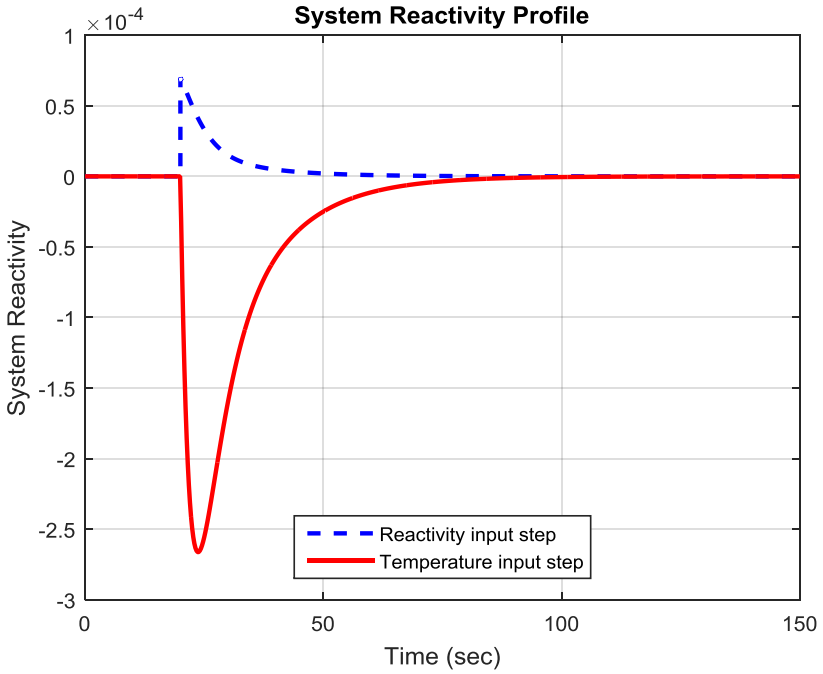

Figure 4.6 System reactivity (ρ) response to a step increase in the input variable for isolated reactor core model.

4.1.1 Response to a step change in external reactivity

A 7×10^{-5} (i.e., 1¢) increase in the reactivity due to control rod withdrawal is applied to the system at t = 20 s. This action causes an increase in the fission rate and neutron flux and, correspondingly, an initial rise in reactor thermal power, as shown in Figure 4.1. Following the increased power generation, the fuel temperature increases and more heat is transferred from the fuel region to the primary coolant in the core. The new steady-state fuel (T_F), coolant node 1 (T_{C1}) and 2 (T_{C2}) temperatures rise by 1.9 °C, 0.11 °C, and 0.22 °C, respectively, as shown in Figures. 4.2, 4.3 and 4.4. These temperature changes drive the negative reactivity feedback mechanisms thereby resulting in the new stable power level (P) of 161.2 MWt (see Figure 4.1). These results are consistent with those from Reference [33] where a 7.1¢ step change in external reactivity was applied to the linearized isolated core model developed for the H. B. Robinson Nuclear Plant. That study shows the responses of the reactor thermal power and reactor outlet temperature and their responses are identical with Figures 4.1 and 4.4 in terms of patterns of dynamic behavior.

The coolant mass flow rate exhibits a pattern similar to coolant temperature which is consistent with the theory since it is a function of temperature difference across the core. The increase in coolant temperature induces an increase in the flow rate ($\dot{m}_C$) as expected based on Equation (3.19) and it reaches a value of 709.6 kg/s at the new steady-state operating point as shown in Figure 4.5. In addition, as the transient is caused by a step change in external reactivity, a jump in system reactivity with a value of 7×10^{-5} is observed. After that, it starts to decrease due to negative temperature coefficients of the

fuel and coolant. When the new equilibrium is achieved, ρ goes to zero as it should be in Figure 4.6.

4.1.2 Response to a step change in primary coolant inlet temperature

As the second transient, a 2.45 ºC (i.e., 1%) increase in the core inlet coolant temperature is applied to the system, again, at t = 20 s. Due to this perturbation, the core coolant node 1 and 2 temperatures increase (see Figures 4.3 and 4.4). Correspondingly, the reactivity decreases due to the negative temperature coefficient of the moderator, which leads to a sharp decrease in the reactor thermal power as seen in Figure 4.1. As a result, the fuel temperature falls, and the heat transfer from fuel to coolant region decreases, and the increase in the coolant temperatures stops. When a new stable point is reached, the difference in the core thermal power compared to the initial condition is -8.2 MW as depicted in Figure 4.1. The average fuel temperature dips to 493.5 °C while the rises in the core coolant node 1 and 2 temperatures becomes stable around values of 291.9 °C and 270.2 °C, respectively.

A sudden decrease in the coolant flow rate is observed as shown in Figure 4.5 since an increase in core coolant temperature is implemented. Following that, it starts to recover as the coolant node 1 and 2 temperatures rise. However, the new steady-state value, which is 695.6 kg/s, is less than its initial value of 708 kg/s because the reactor operates with a lower thermal power output. Furthermore, the system produces negative reactivity as depicted in Figure 4.6 although there is no change in control rod position. This negative reactivity, an expected result of negative temperature coefficients, is due to

initial rises in coolant temperatures. The negative reactivity is eventually canceled by both the moderator and fuel temperature feedback coefficients.

4.2 Isolated Steam Generator Model

Testing the isolated nonlinear steam generator model is achieved by introducing positive step disturbances to temperature of the primary coolant at the steam generator inlet, primary coolant flow rate, feedwater inlet temperature and to steam valve position, individually. Hence, there are two perturbations to the primary and two to the secondary side. A comparison is made between results from the isolated steam generator and References [41], [43], and [56]. Figures 4.7-4.11 show the behavior of some of the state variables and the relevant discussion is provided afterwards.

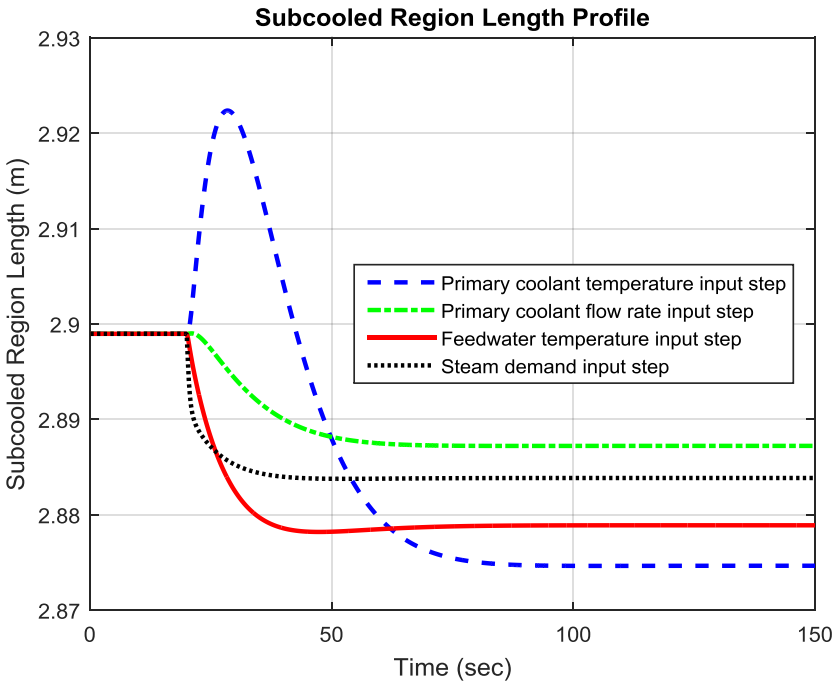

Figure 4.7 Subcooled region length (L_1) response to a step increase in the input variable for isolated steam generator model.

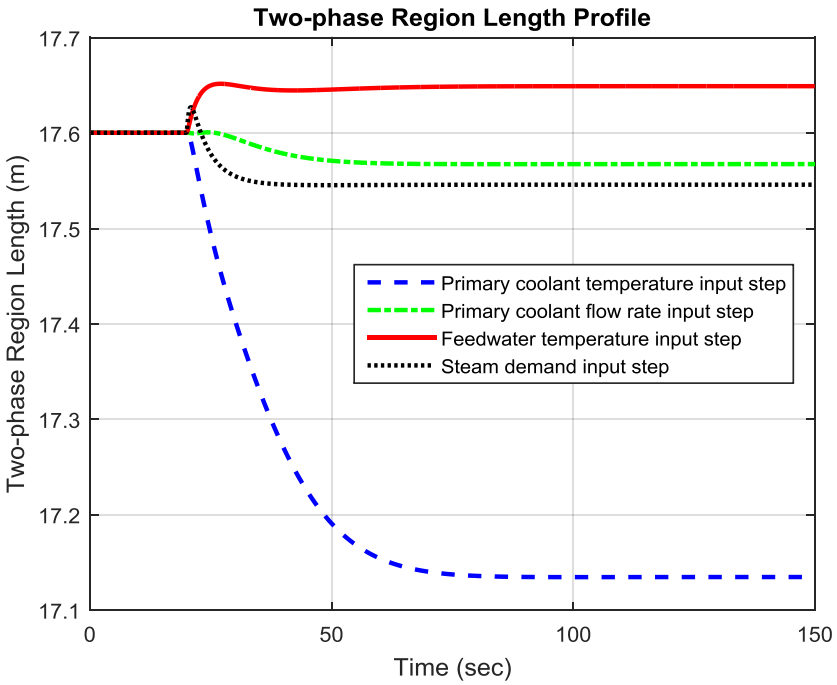

Figure 4.8 Two-phase region length (L_2) response to a step increase in the input variable for isolated steam generator model.

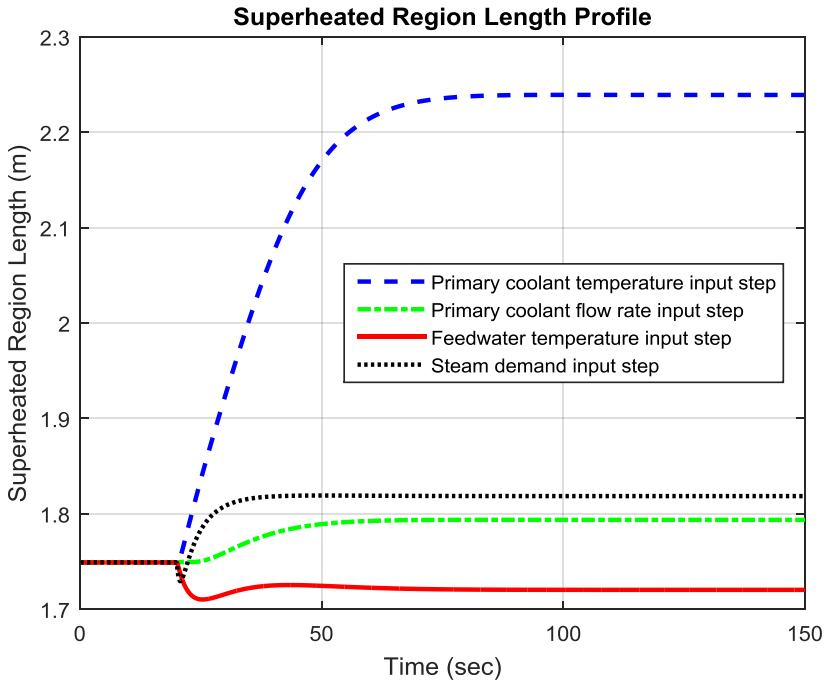

Figure 4.9 Superheated region length (L_3) response to a step increase in the input variable for isolated steam generator model.

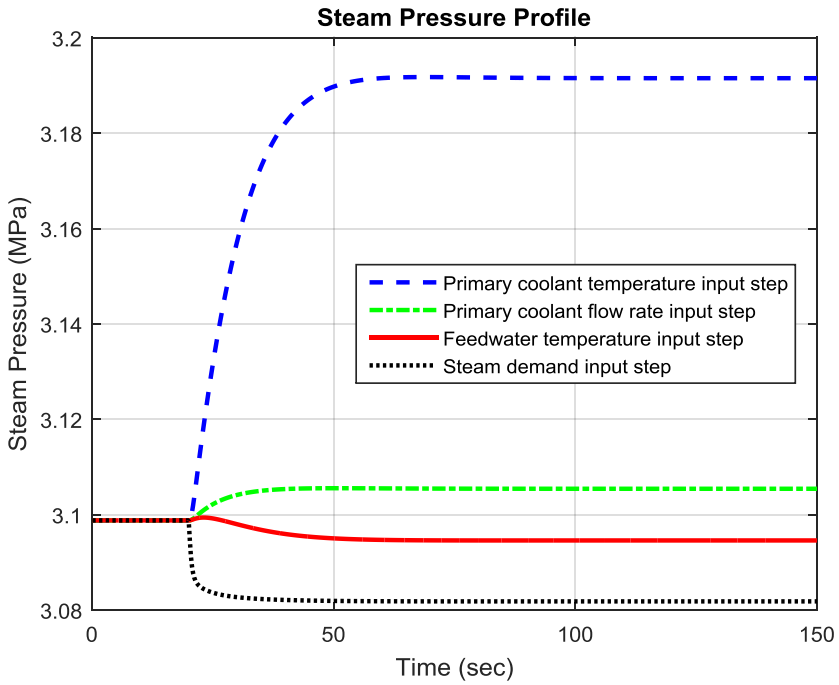

Figure 4.10 Steam pressure (p_S) response to a step increase in the input variable for isolated steam generator model.

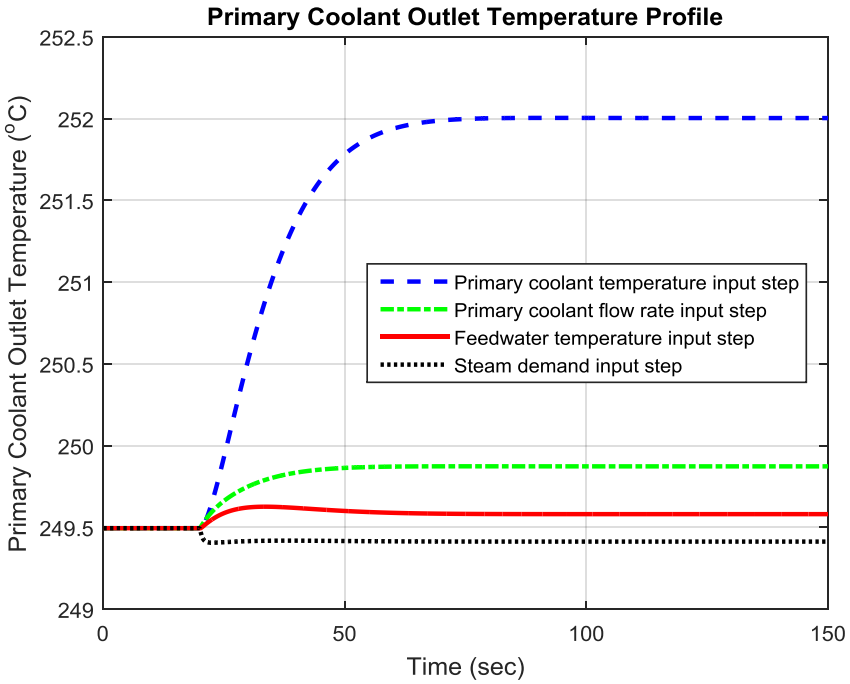

Figure 4.11 Primary coolant outlet temperature (T_{P1}) response to a step increase in the input variable for isolated steam generator model.

4.2.1 Response to a step change in primary coolant inlet temperature

For the first case, an increase of 2.9 °C (i.e., 1%) in the temperature of the primary coolant at the steam generator inlet is introduced at t = 20 sec. The change in the primary coolant temperature results in more heat transfer from the primary side to the secondary via tube metal walls. Since the steam generator considered in this study is a counter-flow heat exchanger, the disturbance is first felt by the superheated region of the secondary side. The increase in the heat transfer rate causes a rise in the steam production and, therefore, an elongation occurs in the superheated region length (L_3) as illustrated in Figure 4.9. Concurrently, the steam pressure (p_S) increases (constant steam valve position) and levels out at a new steady-state value of 3.19 MPa (see Figure 4.10). Figure 4.8 shows that two-phase region (boiling) length (L_2) has a declining trend throughout the simulation because the latent heat of evaporation (h_{fg}) decreases with an increase in the corresponding saturation pressure. The subcooled region length (L_1), however, exhibits an expansion initially and then starts decreasing as depicted in Figure 4.7. This behavior is a result of two different mechanisms acting on the subcooled region simultaneously. As the pressure rises the saturated liquid enthalpy (h_f) increases which explains the early response of the subcooled region length. Following that the increased heat transfer from the primary coolant starts to overcome the need of extra heat to reach the saturation point which accounts for the latter response. In their study, Ray and Bowman [41] tested the helical-coil once-through steam generator model under five different, independent perturbations. One of the perturbations is a 5% step change in the primary coolant inlet temperature. A comparison between the results shows that the dynamic behaviors of the

lengths of each region of the steam generators are very similar: a length decrease in the subcooled and two-phase regions, and an increased length in the superheated region.

Finally, a difference of around +2.5 °C is observed in the primary coolant temperature leaving the steam generator (T_{P1}) when a new equilibrium is achieved; see Figure 4.11.

4.2.2 Response to a step change in primary coolant flow rate

A 7 kg/s (i.e., 1%) step increase in the primary coolant flow rate is applied to the isolated steam generator model at t = 20 sec. Similar to the first case, this transient causes an increased heat transfer from the primary side to secondary side. Thus, the superheated region length expands whereas the lengths of subcooled and boiling regions diminish as seen in Figures 4.7-4.9. The difference in the initial behavior of the subcooled region is owed to a relatively small increase in the steam pressure compared to the previous case. The overall response of the steam generator model, however, is qualitatively similar with the response from the previous case except the fact that the system variables are quantitatively less perturbed.

Another comparison with Reference [41], in which a 5% step increase in the primary coolant flow applied to the steam generator model, shows that all three region lengths exhibit similar transient responses. Furthermore, Ray and Bowman also found in their study that primary coolant inlet temperature and primary coolant flow simulation scenarios are qualitatively similar, however, the system variables are more perturbed in the first scenario.

4.2.3 Response to a step change in feedwater inlet temperature

A 1.5 °C (i.e., 1%) step increase in the feedwater inlet temperature is introduced at t = 20 sec for third simulation case. This change reduces the difference between the feedwater temperature and saturation temperature corresponding to the steam pressure. In addition, the secondary coolant velocity increases due to the decrease in the density for a constant coolant flow rate. Therefore, the subcooled region length shrinks as depicted in Figure 4.7. Furthermore, a slight reduction is observed in the steam pressure (see Figure 4.10) since the higher velocity induces more pressure drop. The latent heat of vaporization increases with a decrease in the pressure which explains the rise in the two-phase region length as shown in Figure 4.8. The superheated region length, on the other hand, exhibits a small decline compared to the initial steady-state value; see Figure 4.9. Finally, the primary coolant outlet temperature increases as the heat transfer from the primary side to the secondary side diminishes due to the perturbation.

Before moving into next section, a comparison is made with Li et al. [43], where a helical-coil steam generator model with helium as coolant is developed. Li et al. presented dynamic behaviors of the (i) steam pressure, (ii) subcooled, two-phase, and superheated regions, and (iii) helium outlet temperature for a 5% step increase in the feedwater temperature. All these mentioned system variables respond similarly to the results herein except the superheated region which expands a very small amount. This difference is likely due to fact that Li et al. include momentum balance into modeling and the pressure drop in each section of the steam generator is different while this study assumes a uniform secondary side pressure.

4.2.4 Response to a step change in steam valve opening

A 1% increase in the steam demand is introduced to the system via a step change in the steam valve position at t = 20 sec. The perturbation engenders a sudden drop in the steam pressure as depicted in Figure 4.10. Concomitantly, the corresponding saturation temperature decreases whereas the latent heat of vaporization increases. These changes result in a decline in the subcooled and two-phase region lengths and an expansion in the superheated region length (see Figures 4.7-4.9). The primary coolant delivers more heat to the secondary side due to the increased temperature difference between both sides caused by the need of additional heat for steam demand. This is the reason that the primary coolant outlet temperatures reaches a new equilibrium value slightly lower than the initial value; Figure 4.11.

This simulation case shows a similarity with the dynamic simulation in Reference [56], in which a moving boundary heat exchanger model is tested under three consecutive perturbations: (1) a 5% increase in the speed of primary coolant pump speed at t = 0 s, (2) a 10% increase in the outer heat transfer coefficient at t = 30 s, and (3) a 10% increase in the nozzle coefficient (or steam valve) at t = 60 s. The comparison of these results after t = 60 s with the results above reveals that steam pressure, subcooled and superheated region lengths show similar dynamic responses. However, the responses for two-phase region lengths are different from each other; the two-phase region length in Reference [56] increases while it exhibits a declining trend over the course of the simulation herein. This difference can be explained by the fact that in Reference [56], the perturbations are

not applied independently and hence, the first and second perturbations may have some lingering effect when the last one is introduced to the system.

4.2.5 Comparison of results

Table 4.1 summarizes comparisons of the simulation results for the isolated steam generator model developed in this study against other references. The agreement of the results provides a basis for the validation of the model and allows it to be used as a part of the complete SMR model.

Table 4.1 Comparison of results for isolated steam generator model without control systems

Scenario	**Response of Isolated Steam Generator Model**	**Other References**
A step increase in primary coolant temperature	For a 1% change, a decrease in the subcooled and two-phase region lengths, and an increase in the superheated region length are observed.	In Reference [41], the dynamic response of the lengths of each region of the steam generators for 5% step change exhibit very similar behavior.
A step increase in primary coolant flow rate	The steam generator response is qualitatively similar with the response from the previous case except the fact that the system variables are quantitatively less perturbed.	It is also found in Reference [41] that the simulation results show a similar pattern with less deviation in system variables from initial equilibrium conditions.
A step increase in feedwater inlet temperature	A decline in the lengths of subcooled and superheated regions and an elongation in two-phase region length are observed for 1% step change. In	For a 5% increase, system variables in Reference [43] respond similarly except the superheated region which expands a very small amount. This difference is likely

	addition, a slight reduction in the steam pressure occurs, and the primary coolant outlet temperature increases as the heat transfer from the primary side to the secondary side diminishes.	due to fact that they include momentum balance into modeling and the pressure drop in each section of the steam generator is different.
A step increase in steam valve opening	Steam pressure decreases for a 1% increase in the valve opening. The subcooled and two-phase regions shrink, and superheated region length increases for this perturbation.	In Reference [56], steam pressure, subcooled and superheated region lengths show similar dynamic responses. However, the response for two-phase region length is different which might be due to the fact that the perturbations are not applied independently and hence, the first and second perturbations may have some lingering effect when the last one is introduced.

4.3 Isolated Pressurizer Model

The isolated pressurizer model has three inputs: (1) electric heater, (2) insurge (or outsurge) flow, and (3) spray flow. The model is tested by perturbing the input variable under investigation from its initial equilibrium value while keeping the others constant. Figure 4.12 shows the response of the pressurizer pressure for changes in aforementioned input variables. The pressure response is also compared with the response from Reference [34].

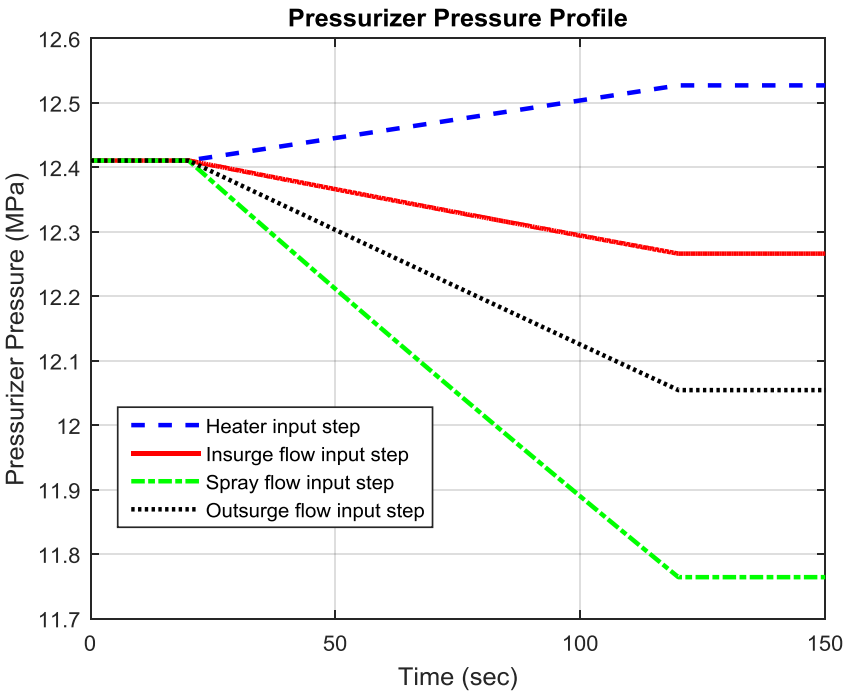

Figure 4.12 Pressurizer pressure (p_p) response to a step increase in the input variable for isolated pressurizer model without control system.

4.3.1 Response to a step change in electric heater input

A 100 kW step increase in the electric heater is applied to the isolated pressurizer model between t = 20 sec and t = 120 sec. As the pressurizer is under saturated conditions at the steady-state, vaporization starts because of the additional heat provided by the heaters. That is the reason that the pressurizer pressure increases during the time of disturbance as seen in Figure 4.12. After the electric heater is turned off, the pressure stays at that level which is 0.12 MPa higher that the initial equilibrium value. This result is congruent with the result from Reference [34], where a 100 kW step increase in the electric heat input is applied to the linearized pressurizer model.

4.3.2 Response to a step change in insurge flow rate

A 2 kg/s step increase in the surge flow (insurge) is introduced between t = 20 sec and t = 120 sec. The liquid inside the pressurizer and the subcooled liquid from the primary coolant system constitute a mixture that has a temperature lower than the saturation temperature. The decrease in the temperature causes the contraction of the liquid volume inside the pressurizer which accounts for the small gradual decrease in the pressure; see Figure 4.12. When this result is compared with the same perturbation case with a different magnitude in Reference [34], the dynamic responses do not agree each other. This is most likely due to the fact that the coefficient of the surge term for the linearized pressurized model in [34] is calculated by using only saturated liquid enthalpy ($h = h_f$). In this study, however, enthalpy term (h) in Equation (3.49) changes depending on whether the surge flow is an insurge or outsurge flow.

4.3.3 Response to a step change in outsurge flow rate

As the third case, an outsurge flow perturbation of 2 kg/s is applied at t = 20 sec and then the flow rate is reverted to its initial steady-state value at t = 120 sec. This perturbation causes a decline in the liquid volume inside the pressurizer. Hence, the pressurizer pressure shows a decreasing trend in Figure 4.12 and the overall pressure drop is bigger compared to the result from the preceding case as expected.

4.3.4 Response to a step change in spray flow rate

For the last case, a 2 kg/s positive step change in the spray flow is introduced into system between t = 20 sec and t = 120 sec. The temperature of the spray is lower than the temperature of the insurge flow from the previous case. Due to this fact, the liquid

mixture has a lower temperature compared to the mixture from the last case. This, then, theoretically implies that the pressure drop should be larger for this transient which is congruent with the pressure response as illustrated in Figure 4.12. The result from Reference [34], again, for the same disturbance but with a different magnitude, exhibits the same dynamic behavior with the result of the simulation case above.

As seen from the results for four different scenarios, only the increase in the electric heater input induces a rise in the pressurizer pressure, which may explain why no continuous spray exists in SMRs as stated earlier in Section 3.4.

4.3.5 Comparison of results

Table 4.2 summarizes comparisons of the simulation results for the isolated pressurizer model developed in this study against a MS thesis by Thakkar [34]. The agreement of the results provides a basis for the validation of the model and allows it to be used as a part of the complete SMR model.

Table 4.2 Comparison of results for isolated pressurizer model without control systems

Scenario	**Response of Isolated Pressurizer Model**	**Other Reference**
A 100 kW step increase in electric heater	As the pressurizer is under saturated conditions at the steady-state, vaporization starts because of the additional heat provided by the heaters and the pressurizer pressure increases.	The model result is congruent with the result from Reference [34], where a 100 kW step increase in the electric heat input is applied to the linearized pressurizer model.

A step increase in insurge flow rate	A 2 kg/s step increase in the surge flow (insurge) causes a small gradual decrease in the pressure.	The pressurizer response for a 50 lb/s step increase in Reference [34] does not agree with the result herein both qualitatively and quantitatively. This is most likely due to the fact that the coefficient of the surge term for the linearized pressurized model in [34] is calculated by using only saturated liquid enthalpy ($h = h_f$).
A step increase in spray flow rate	A 2 kg/s positive step change in the spray flow leads to a drop in the pressurizer pressure.	The result from Reference [34] for the same disturbance but with a different magnitude (50 lb/s), exhibits the same dynamic behavior with the result of the simulation case above.

4.4 Single SMR Unit Model

4.4.1 Steady-state performance of the model

The overall SMR model is first simulated under steady-state conditions at 100% power using Simulink. Some important simulation results are listed in Table 4.3, and the steady-state temperature profile of the steam generator is shown in Figure 4.13. A comparison of the results with the design data [28] and [30] shows that they are consistent with each other, which justifies further studying of the model under dynamic conditions. However, as no other researchers have published a complete SMR dynamic

model, there will be no comparisons to make other than checking congruence of the model response with theory.

Table 4.3 Steady-state values of important parameters

Parameter	**Value**
Reactor thermal power	160.1 MW
Net electrical output	45.3 MW
Pressurizer pressure	12.41 MPa
Primary coolant mass flow rate	708 kg/s
Hot leg riser temperature	291 °C
Downcomer region temperature	246 °C
Steam generator total tube length	22.25 m
Subcooled region length	2.90 m
Two-phase region length	17.60 m
Superheated region length	1.75 m
Feedwater temperature	148.5 °C
Steam temperature	264 °C
Steam pressure	3.1 MPa
Steam mass flow rate	71.25 kg/s

It is noteworthy that the primary and secondary pressure values for the NuScale SMR are considerably less than those for today's large PWRs. Typical values for a central station PWR are around 15.5 MPa and 7 MPa for the primary and secondary, respectively.

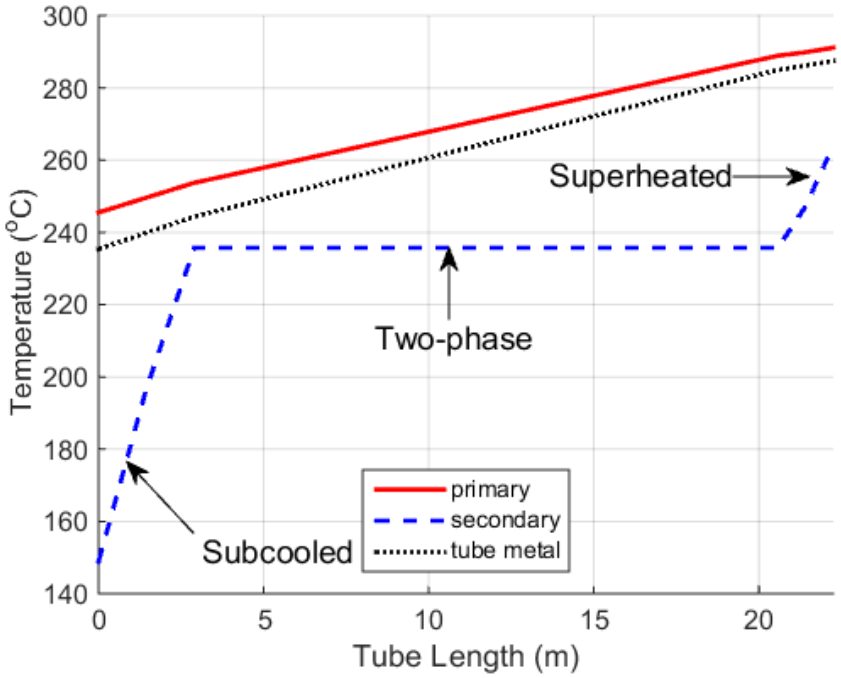

Figure 4.13 Steam generator temperature profile at steady-state (100% power).

4.4.2 Dynamic performance of the model

For the dynamic performance of the system, a step increase in each input variable, i.e., control rod position (withdrawal), steam demand, pressurizer electric heat, and feedwater temperature, is applied independently after 20 s of steady-state operation to demonstrate that the simulation starts from a stable point and so that the initial steady-state conditions can be seen clearly. The output of the electric heaters, however, reverts to its initial steady-state value at the simulation time of 120 s.

Figures 4.14-4.26 exhibit responses of the different output variables for the aforementioned perturbations. For each case, the input variable under investigation is perturbed from its initial steady-state value while the others are kept constant. The results are discussed in the following subsections according to the input step change.

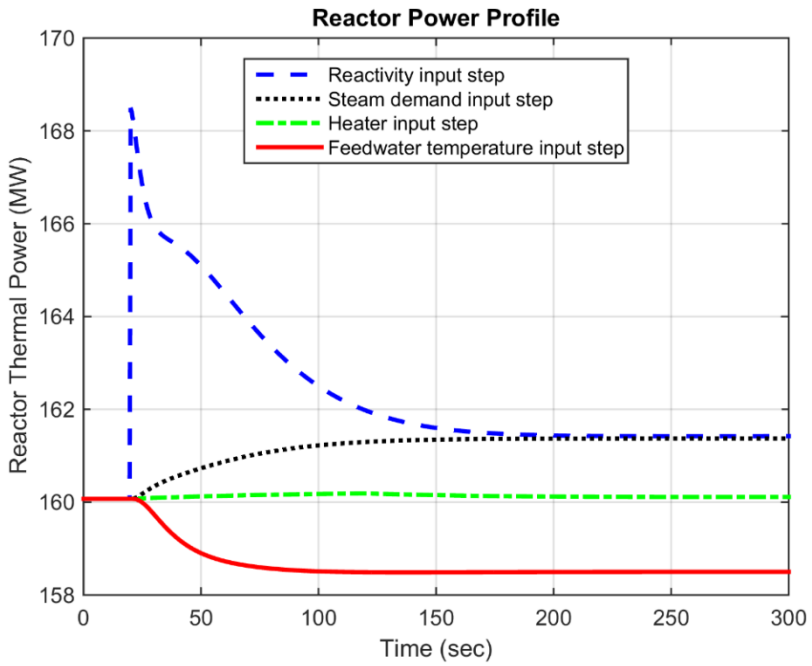

Figure 4.14 Reactor power (P) response to a step increase in the input variable for single SMR unit.

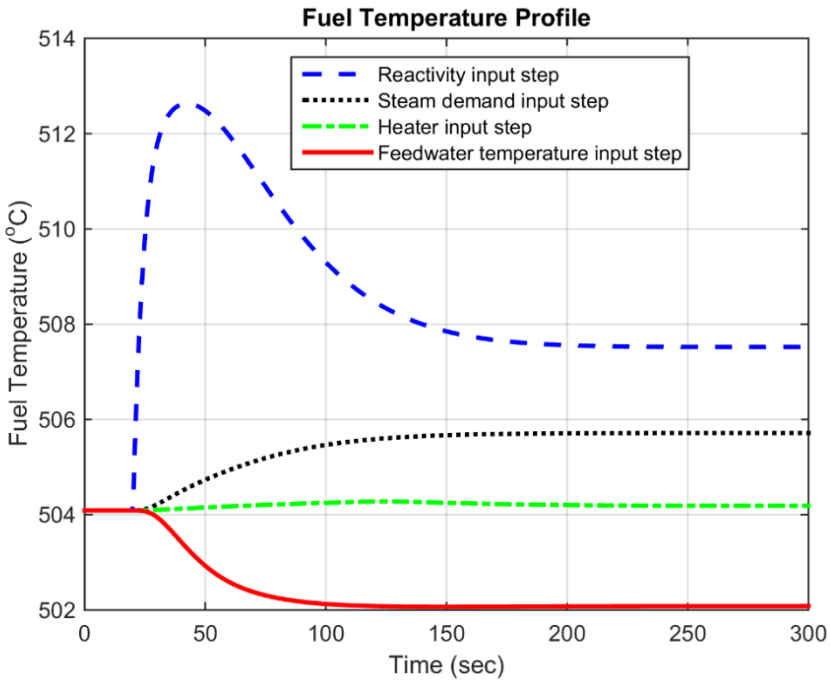

Figure 4.15 Fuel temperature (T_F) response to a step increase in the input variable for single SMR unit.

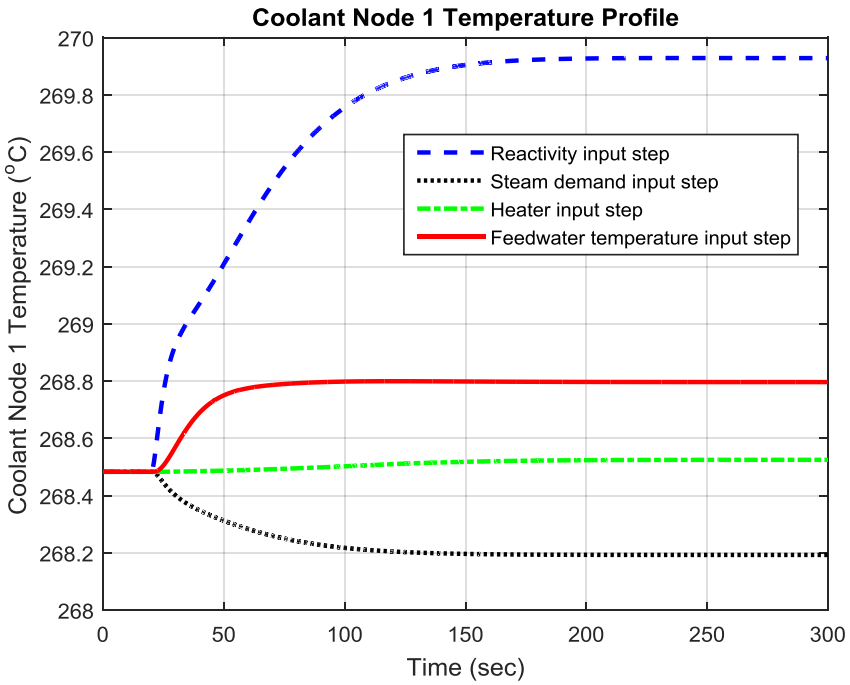

Figure 4.16 Reactor core coolant node 1 temperature (T_{C1}) response to a step increase in the input variable for single SMR unit.

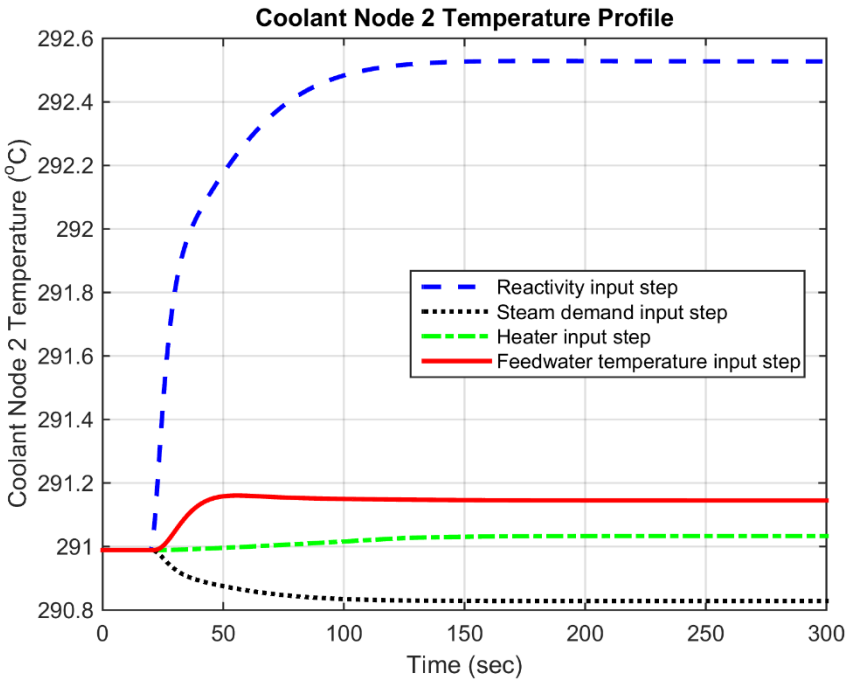

Figure 4.17 Reactor core coolant node 2 temperature (T_{C2}) response to a step increase in the input variable for single SMR unit.

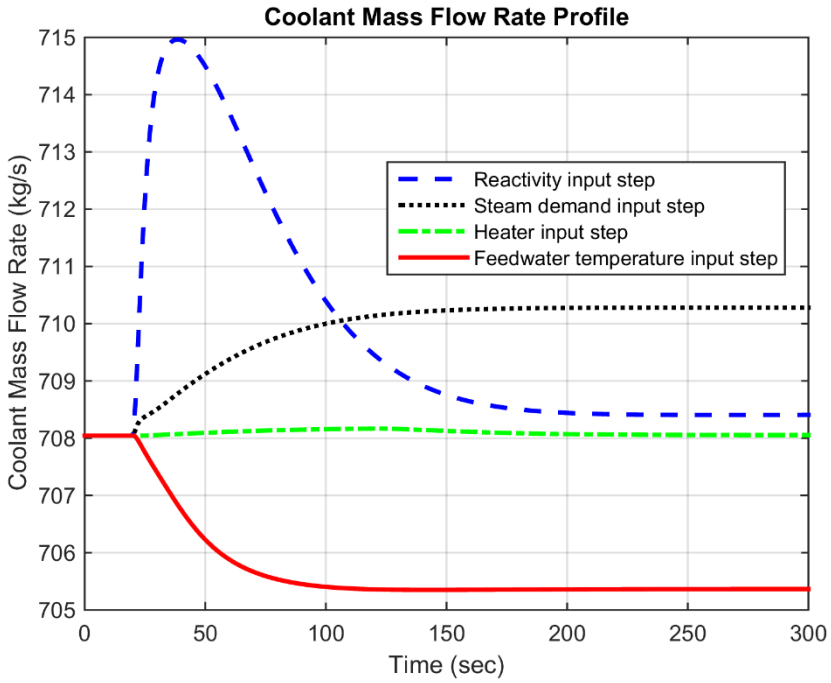

Figure 4.18 Primary coolant mass flow rate ($\dot{m}_C$) response to a step increase in the input variable for single SMR unit.

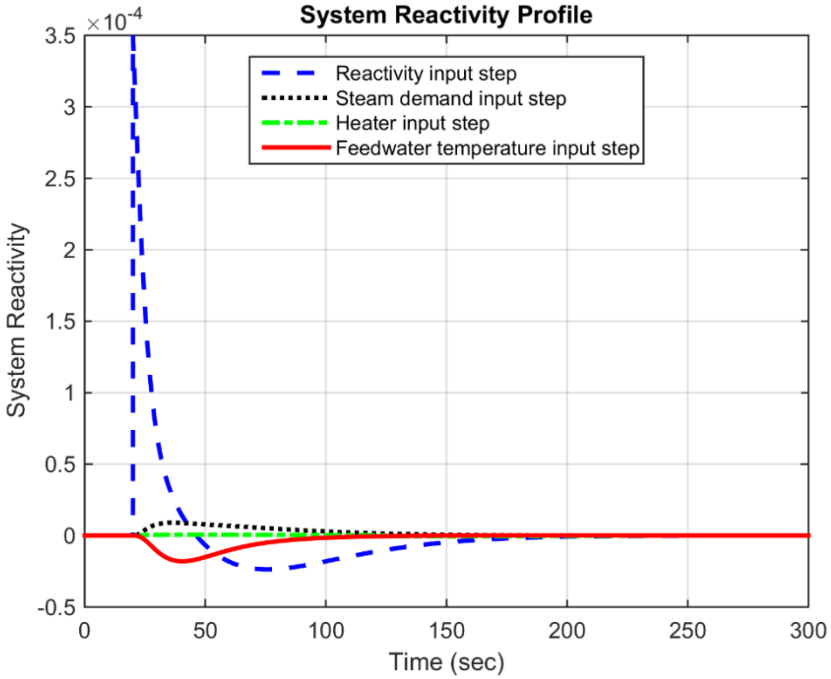

Figure 4.19 System reactivity (ρ) response to a step increase in the input variable for single SMR unit.

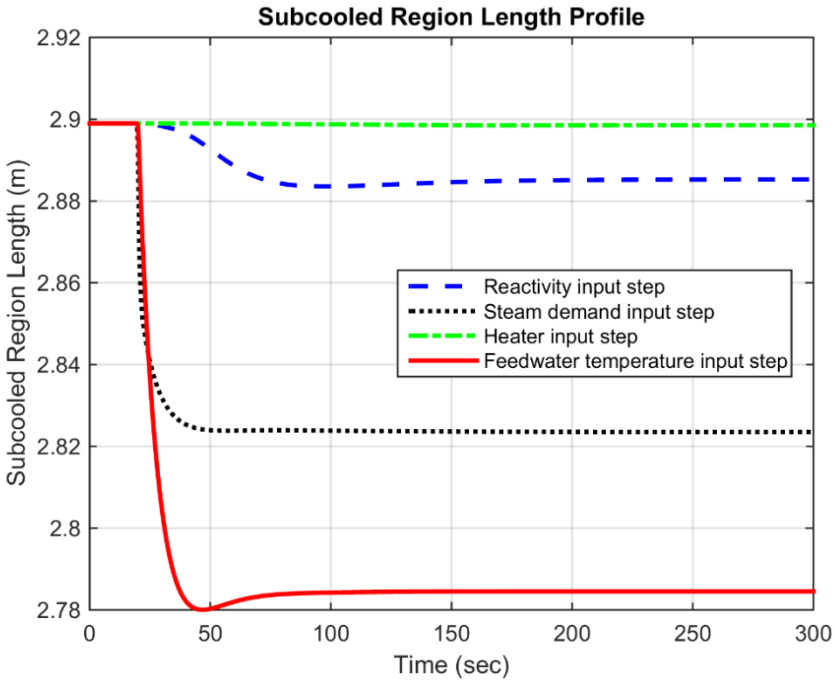

Figure 4.20 Subcooled region length (L_1) response to a step increase in the input variable for single SMR unit.

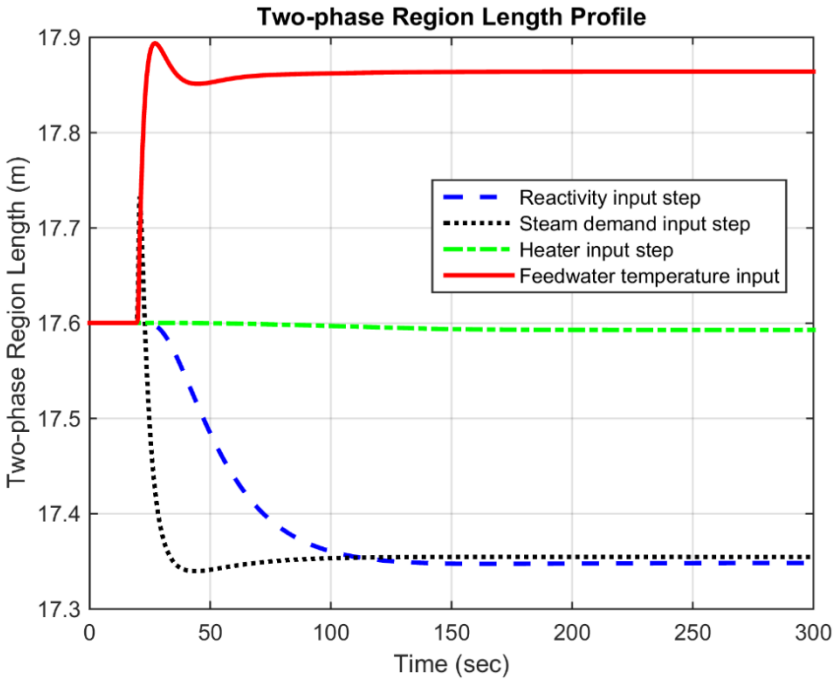

Figure 4.21 Two-phase region length (L_2) response to a step increase in the input variable for single SMR unit.

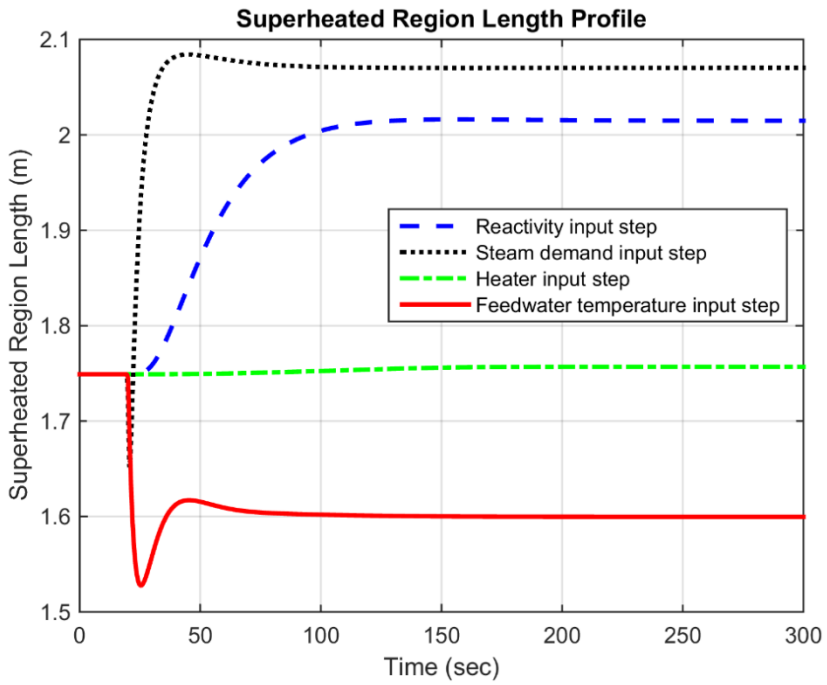

Figure 4.22 Superheated region length (L_3) response to a step increase in the input variable for single SMR unit.

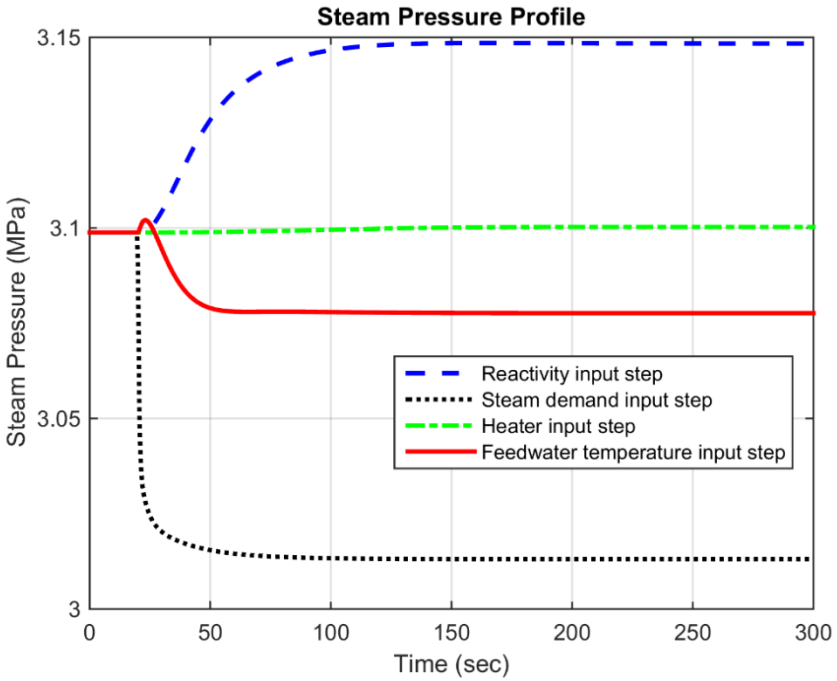

Figure 4.23 Steam pressure (p_S) response to a step increase in the input variable for single SMR unit.

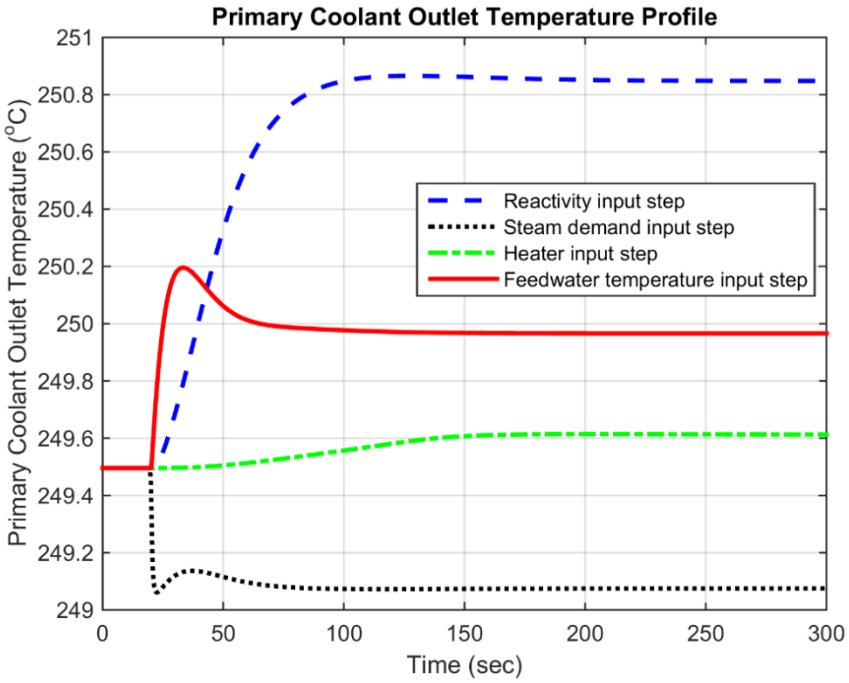

Figure 4.24 Primary coolant temperature (T_{P1}) response at the steam generator outlet to a step increase in the input variable for single SMR unit.

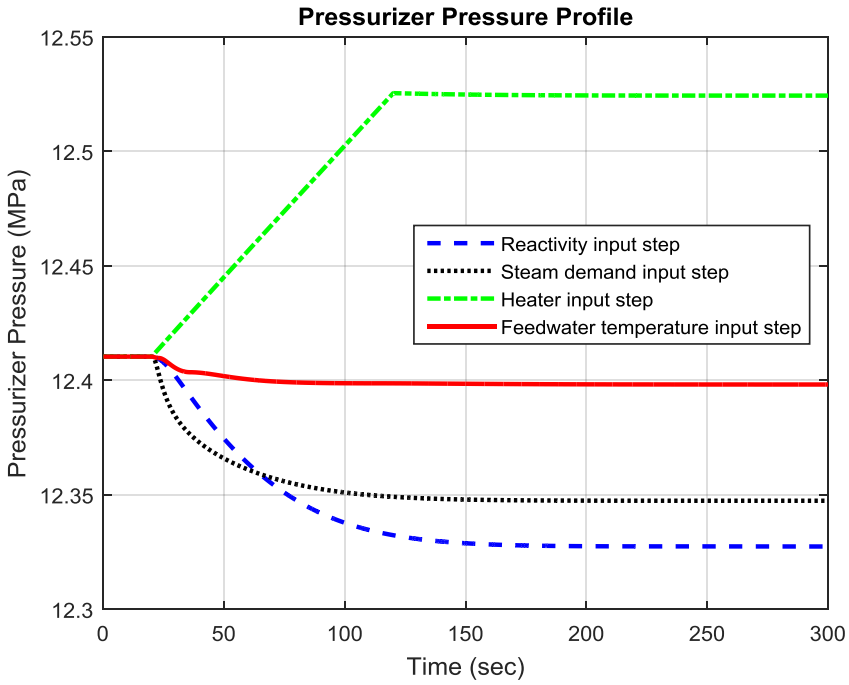

Figure 4.25 Pressurizer pressure (p_p) response to a step increase in the input variable for single SMR unit.

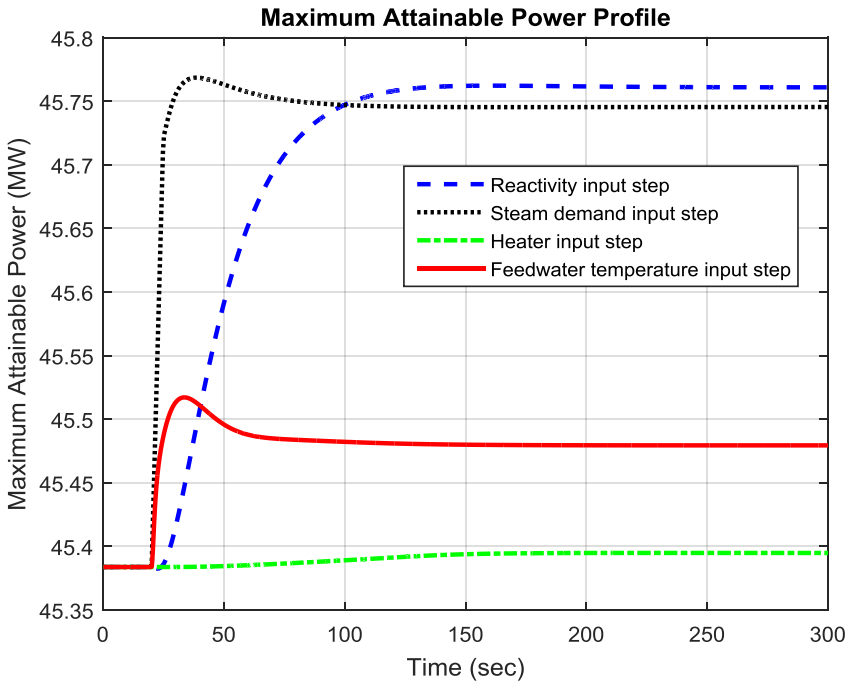

Figure 4.26 Maximum attainable power (P_m) response to a step increase in the input variable for single SMR unit.

4.4.2.1 Response to a step change in external reactivity

A 3.5×10^{-4} (i.e., 5¢) step increase in the reactivity due to control rod withdrawal is applied to the system at t = 20 s as seen in Figure 4.19. Since this perturbation causes a reduction in neutron absorption inside the core region, an upsurge in the fission rate and neutron flux occurs. Therefore, the reactor thermal power (P) exhibits an 8.3 MWt prompt jump as shown in Figure 4.14. Corresponding to the change in the thermal power, the fuel temperature (T_F) rises (Figure 4.15) which induces more heat transfer from the fuel region to the primary coolant in the core. This is congruent with the increase in the coolant node 1 (T_{C1}) and 2 (T_{C2}) temperatures as shown in Figures 4.16 and 4.17, respectively.

The increase in the temperature of the primary fluid at the steam generator inlet leads to an increase in the heat transfer from the primary side to the secondary side of the steam generator through the tube metal wall. More heat transfer raises the steam generation and results in an expansion in the superheated region length (L_3) as seen in Figure 4.22. Concomitantly, the secondary pressure (p_S) rises (see Figure 4.23) since no change is made to the steam valve opening. As the pressure increases, the corresponding saturation temperature of the secondary (feedwater) rises while the latent heat of vaporization (h_{fg}) declines which explains the decrease in the length of the two-phase region (L_2); see Figure 4.21. There is a competition between the increased heat delivery and the need for more heat to bring the feedwater to the saturation point, and as Figure 4.20 reveals, there is a small decrease in the subcooled region length (L_1) indicating that the first mechanism dominates.

The overall increase in the temperature of the primary coolant system causes an expansion of the coolant volume which, then, leads a surge flow into the pressurizer. The mixture of the saturated liquid inside the pressurizer and the subcooled liquid from the primary coolant system has a lower temperature than the saturation temperature corresponding to the pressurizer pressure at the initial steady-state condition. This causes a gradual decrease in the pressurizer pressure (p_p) due to the perturbation in the control rod position (see Figure 4.25).

All of these ensuing changes in the fuel and reactor coolant temperatures, and the primary coolant pressure drive the reactivity feedback mechanisms thereby resulting in the new stable power level of 161.4 MWt. The primary coolant mass flow rate ($\dot{m}_c$)

shows a similar trend with the response of the reactor power as seen in Figures 4.14 and 4.18 and as expected from Equation (3.20). As the disturbance is initiated at the primary side, the turbine starts to feel the associated effect after a time delay, which is approximately 10 s and in agreement with the initial steady-state time constant for the hot leg riser. The attainable power power (P_m) rises gradually and settles to a new steady-state value of 45.7 MW as depicted in Figure 4.26. Finally, the system reactivity ρ returns to zero, as it should, when the new equilibrium is achieved (Figure 4.19).

4.4.2.2 Response to a step change in feedwater inlet temperature

For the second scenario, a 7.425 °C (i.e., 5%) increase in the feedwater inlet temperature (T_{Si}) is introduced at t = 20 s. With this perturbation, the required heat for the feedwater to reach the saturation temperature diminishes and the length of the subcooled region is reduced as shown in Figure 4.20. In addition, the secondary fluid density decreases which results in higher velocity, correspondingly. The increase in the fluid velocity, then, engenders a larger pressure drop that accounts for the decline in the steam pressure (see Figure 4.23). Thus, the latent heat of vaporization rises and an increase in the length of the two-phase region is observed as depicted in Figure 4.21. Moreover, the superheated region length levels out at a new equilibrium value shorter that the initial one; see Figure 4.22.

This input perturbation raises the average secondary temperature such that there is a decrease in the heat transfer from the primary side to secondary side. This causes a rise in the temperature of the primary coolant at the steam generator outlet (T_{P1}) as well as the primary coolant temperature leaving the reactor core as seen in Figures 4.24 and 4.17,

respectively. When the aforementioned temperature change is felt by the reactor core, the system reactivity starts decreasing due to the negative reactivity temperature coefficients and shows a dip with a minimum value of -1.78×10^{-5} as exhibited in Figure 4.19. Thus, a reduction in both the reactor thermal power and fuel temperature is observed. At the new steady-state operating level, the reactor thermal power has declined to 158.4 MW (Figure 4.14). In addition, the coolant flow rate also shows a similar pattern and decreases by almost –2.6 kg/s. The attainable power power, however, exhibits a rise of about 0.2 MW at the new steady-state condition since the additional heat content of the feedwater exceeds the decrease in the reactor thermal power. This argument is supported by a simple heat balance. Considering the steam generator as a boiler

$$\delta P_m = n_{th}\ \delta Q_{boiler} \tag{4.1}$$

$$\delta Q_{boiler} = \delta Q_{RX} + \delta Q_{FW} = \delta Q_{RX} + \dot{m}_{S,i}\Delta h \tag{4.2}$$

where n_{th} is the Rankine cycle thermal efficiency (28%); δQ terms with subscripts (RX) and (FW) are the change in heat provided by the reactor core (–1.6 MW) and feedwater, respectively; Δh is the difference in the enthalpy of the feedwater before and after the disturbance (32.6 kJ/kg) and the new equilibrium value of the feedwater flow rate ($\dot{m}_{S,i}$) is 70.8 kg/s. After the calculation is performed, δP_m is 0.2 MW which agrees with the result in Figure 4.26.

The pressurizer pressure, in this case, shows a very similar behavior compared to the previous case and decreases due to the increase in the primary coolant temperature. However, the pressure decrement is smaller since the increase in the temperature is less compared to the first case.

4.4.2.3 Response to a step change in pressurizer heater input

For the third case, a 100 kW increase in the pressurizer heater is applied to the system, between t = 20 s and t = 120 s, so as to observe the effect of a disturbance initiated inside the pressurizer on the primary and secondary sides. As more heat is transferred to the saturated liquid inside the pressurizer, the pressurizer pressure starts to increase until the heaters are turned off; see Figure 4.25. The deviation of the pressure from the initial steady-state value causes a very small positive change in the reactor thermal power due to the positive reactivity feedback coefficient of the primary pressure. In similar manner, the fuel temperature also increases slightly. After the heaters are turned off, the reactivity feedback mechanisms bring the system reactivity back to its initial value. As understood from a careful examination of the plotted results, the reactor remains at a slightly elevated temperature and pressure compared to the initial equilibrium condition, but overall the disturbance does not have a significant impact on the system state variables.

4.4.2.4 Response to a step change in steam valve opening

A 5% step increase in the steam valve opening is introduced at t = 20 s. The action induces a sudden dip in the steam pressure, as depicted in Figure 4.23, as well as in the corresponding saturation temperature. Thus, an abrupt vaporization takes place in the steam generator, which is the underlying reason of the prompt jump in the apparent attainable power; see Figure 4.26. This behavior is a result of the turbine model simply calculating the attainable power as the product of associated variables used in the study. In reality, however, the turbine inertia would prevent such response. The aforementioned

momentary steam production cannot be maintained since the reactor core is not able to respond to the need for steam instantly. These changes in the thermodynamic properties lead to a decrease in the lengths of the subcooled and two-phase regions whereas an elongation occurs in the superheated region length, as shown in Figures 4.20, 4.21, and 4.22, respectively.

The bigger temperature difference among the primary and secondary sides is due to the increase in the steam demand causing more heat transfer to the secondary side from the primary side and a decrease in the average temperature of the primary coolant. Simultaneously, the coolant volume shrinks which results in a surge flow out of the pressurizer. As a result, the primary coolant pressure in the pressurizer diminishes and then settles down to a new equilibrium point; see Figure 4.25. The reactivity feedback coefficients of the fuel and coolant temperatures and the primary pressure increase the system reactivity, reaching a maximum value of 9×10^{-6}, and drive the reactor thermal power and fuel temperature up. The final steady-state value of the thermal power is around 161.4 MW which corresponds to a new stable value of the attainable power of 45.7 MW.

4.5 Single SMR Unit Model with Control Systems

The effect of the control systems on the dynamic response of the single SMR unit model is analyzed with two different scenarios:

1. Increase in steam valve opening, and
2. Increase in reactor thermal power.

4.5.1 Increase in steam valve opening

For the first scenario, a 5% step increase in the load is applied to the system at t = 20 s, which results in a change in the steam valve opening. For comparison, two different simulations under the same disturbance are run with and without the control systems.

Figures 4.27-4.33 exhibit the changes in the important state variables of the system and the relevant discussion is provided afterwards.

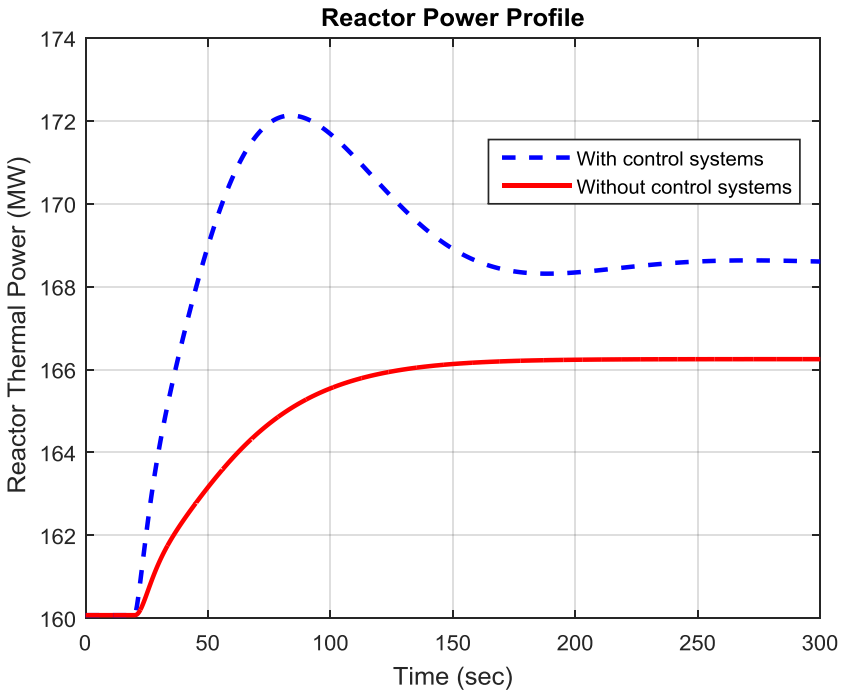

Figure 4.27 Reactor power (P) response for a step increase in the load for single SMR unit with and without control systems.

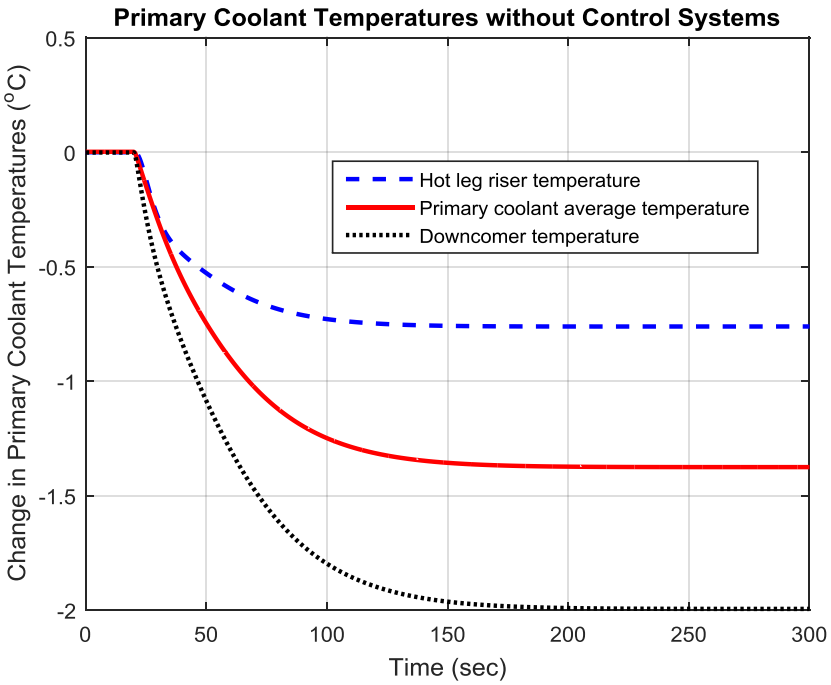

Figure 4.28 Change in primary coolant temperatures for a step increase in the load for single SMR unit without control systems.

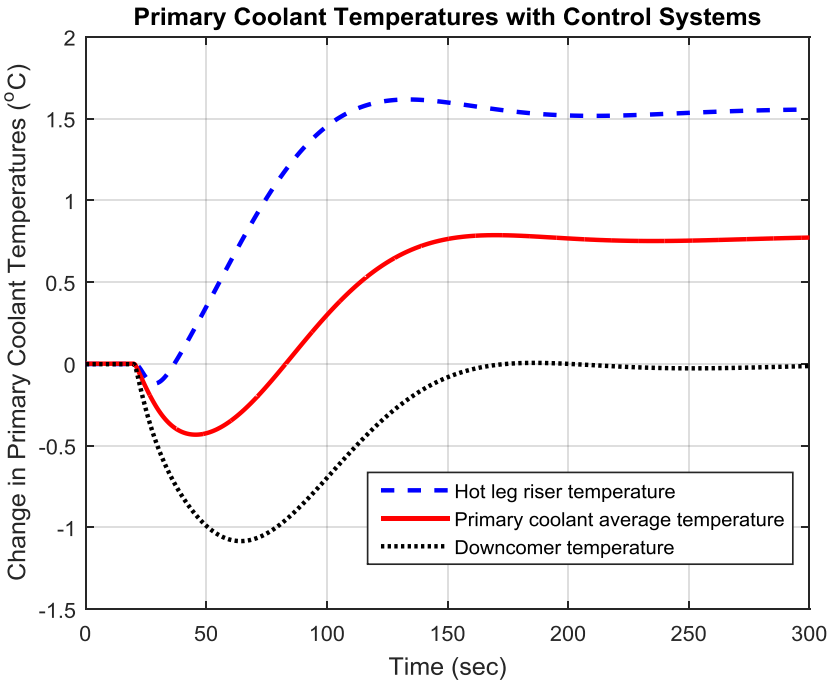

Figure 4.29 Change in primary coolant temperatures for a step increase on the load for single SMR unit with control systems.

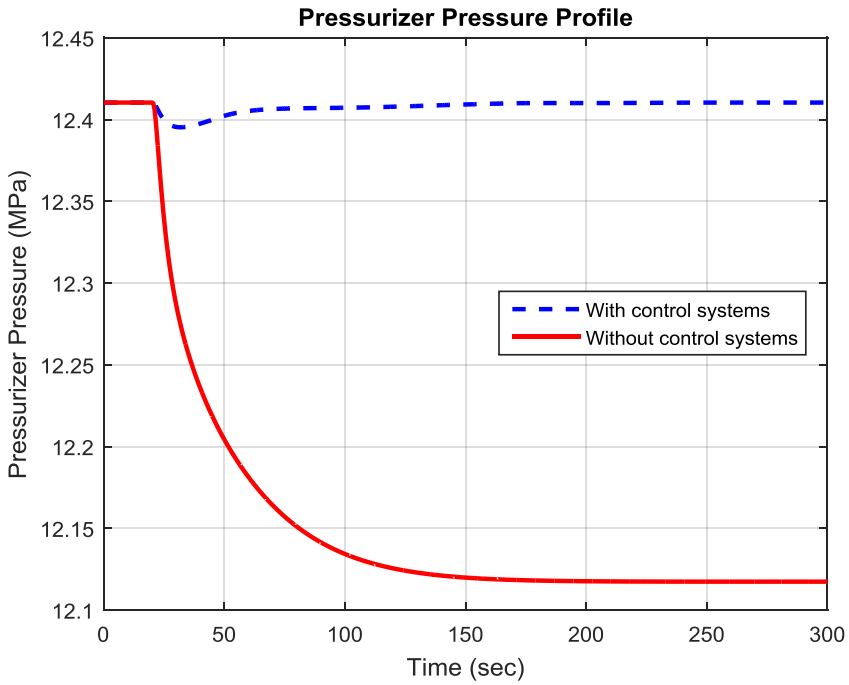

Figure 4.30 Pressurizer pressure (p_P) response for a step increase in the load for single SMR unit with and without control systems.

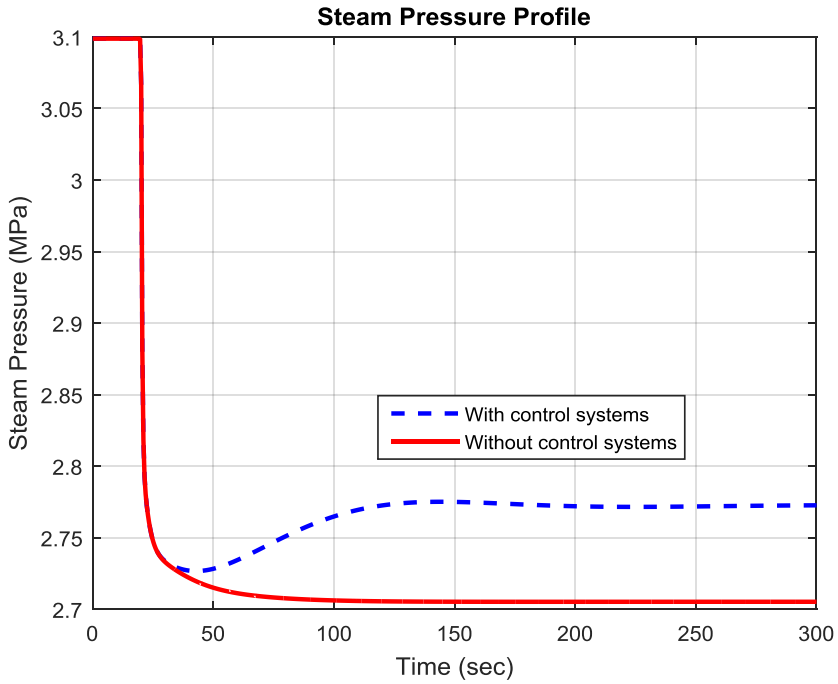

Figure 4.31 Steam pressure (p_S) response for a step increase in the load for single SMR unit with and without control systems.

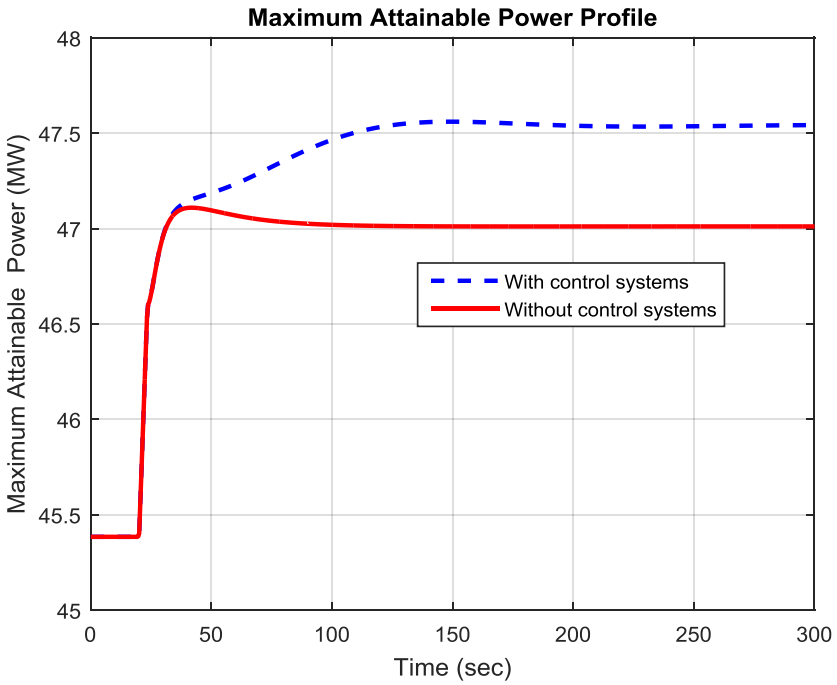

Figure 4.32 Maximum attainable power (P_m) response for a step increase in the load for single SMR unit with and without control systems.

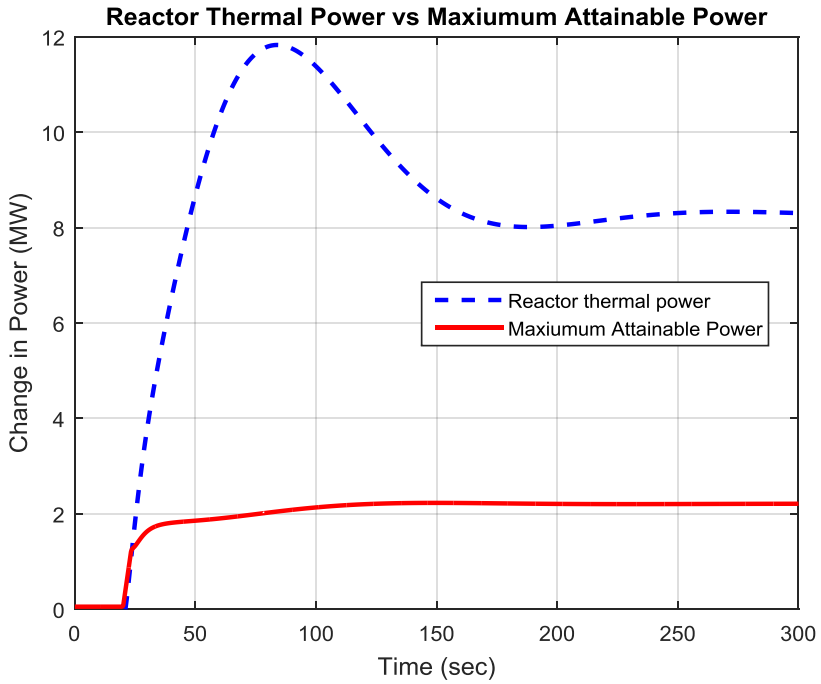

Figure 4.33 Change in thermal and maximum attainable power for a step increase in the load for single SMR unit with control systems.

When the disturbance is introduced without control systems, the steam pressure decreases (see Figure 4.31) and flash steam is produced momentarily as explained previously in Section 4.4.2.4. The rise in the steam demand causes more heat transfer from the primary side to secondary. Thus, the primary coolant temperatures decrease as shown in Figure 4.28 if no control action is taken. The reactivity feedback mechanisms induce a positive reactivity into the system due to the reduction in the temperatures, thereby leading to a gradual increase in the reactor thermal power (see Figure 4.27) even though no adjustment to the control rod positions is made. However, the increase does not satisfy the demand as the new steady-state value is around 166 MW, which is 3.5% higher than the initial steady-state value but a reactor power of 8.2 MW is needed to meet the demand. The attainable power also goes up by 1.7 MW and reaches a value of 47 MW accordingly, as depicted in Figure 4.32, at the new equilibrium operating point.

The decrease in the primary coolant temperatures reduces the coolant volume in the primary loop and, therefore, an outsurge flow from the pressurizer via the baffle is observed. As the liquid-vapor balance inside the pressurizer is lost, the pressure diminishes with no active control on heaters until a new equilibrium is established (see Figure 4.30).

If the same disturbance is applied while the control systems are active, the initial decrease in the downcomer temperature (see Figure 4.29) produces an error signal for the sliding-average-temperature controller. Following that the control rods are withdrawn accordingly, thereby introducing a positive external reactivity. The external reactivity results in a faster increase in the thermal power compared to the no-control case as shown

in Figure 4.27. After an overshoot, the power level settles down to a value of 168.3 MW which is congruent with the new setpoint established by the change in the load. Furthermore, the downcomer temperature starts increasing, after the initial dip, and reaches the pre-transient steady-state value (Figure 4.29), which is the desired behavior achieved by the sliding-average-temperature controller. Finally, a small recovery is noticed in the steam pressure with the reactor control as seen in Figure 4.31. These latter observations are in agreement with the theory discussed in Section 3.6.1.3.

In a similar manner, the pressurizer pressure controller senses the difference between the reference and actual values of the pressure after the transient is initiated, and then applies more power to the heaters to keep the pressure constant. Figure 4.30 reveals that around 60 s after the disturbance, the primary pressure is returned to its initial steady-state value.

The attainable power rises in accordance with the thermal power and reaches a value of 47.56 MW as desired in the control case (Figure 4.32). Figure 4.33 shows the equilibrium deviation of the thermal (+8.2 MW) and attainable (+2.3 MW) power which yields a thermal efficiency of 28%.

4.5.2 Increase in reactor thermal power

The other scenario to test the effectiveness of the control system is to increase (or decrease) the reactor thermal power to a certain level within a desired time period when it is necessary.

For this simulation case, the reference value of the sliding-average-temperature controller is set to a new value of 253.3 °C , which was 245 °C initially, by a ramp

function between t =20 s and t = 320 s. And the set point is kept at this new value for the rest of the simulation (t > 320 s). A ramp is used instead of applying a step function to avoid large power overshoot. This is congruent with the industry practice for PWRs [65]. This control action is intended to reach a new thermal power level of 5% higher than the initial power level.

Figures 4.34-4.42 depict how some of the important system variables changes over time for this simulation case.

Figure 4.34 Reactor power (P) response for a ramp increase in reactor power controller reference value for single SMR unit.

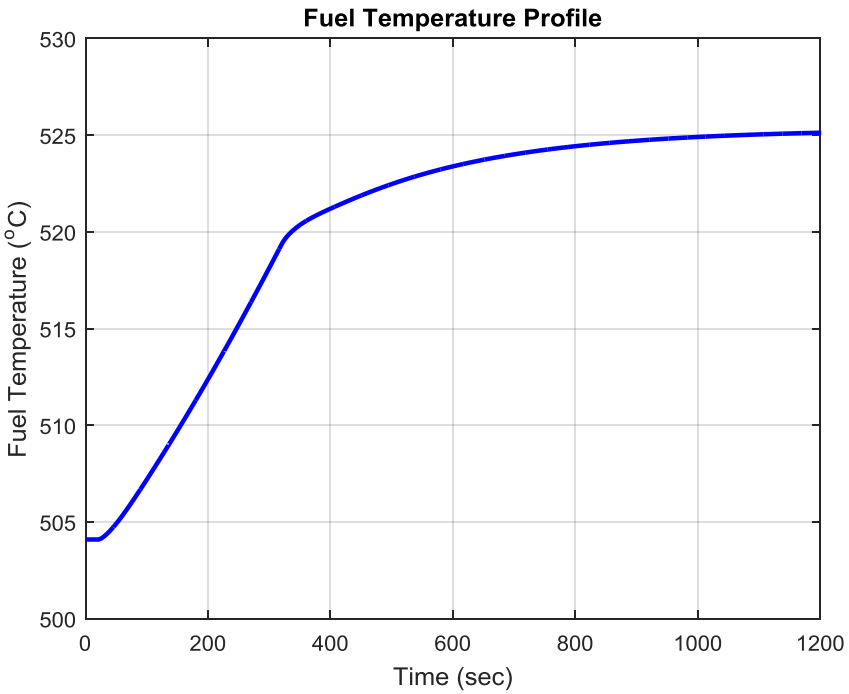

Figure 4.35 Fuel temperature (T_F) response for a ramp increase in reactor power controller reference value for single SMR unit.

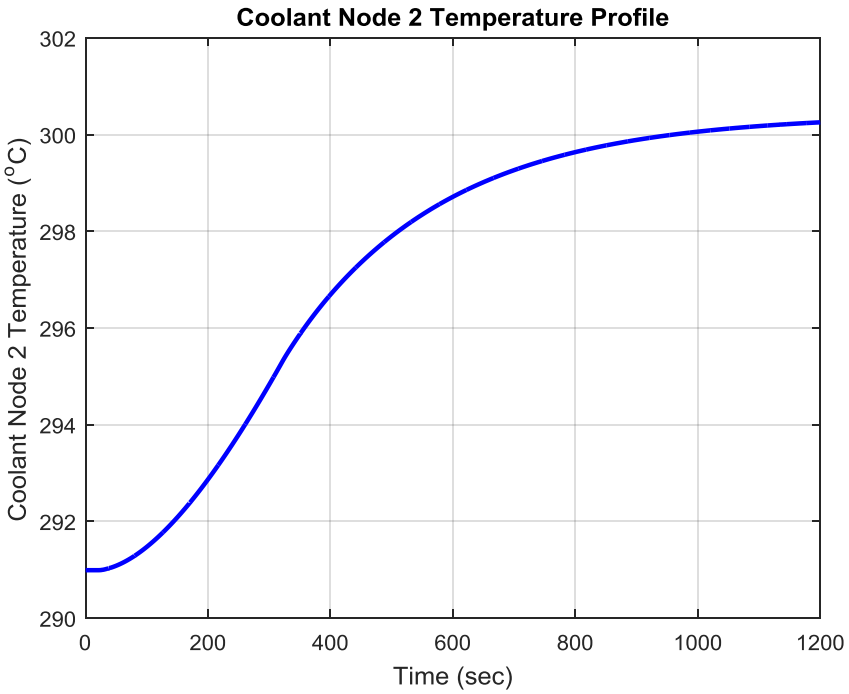

Figure 4.36 Reactor core coolant node 2 temperature (T_{C2}) response for a ramp increase in reactor power controller reference value for single SMR unit.

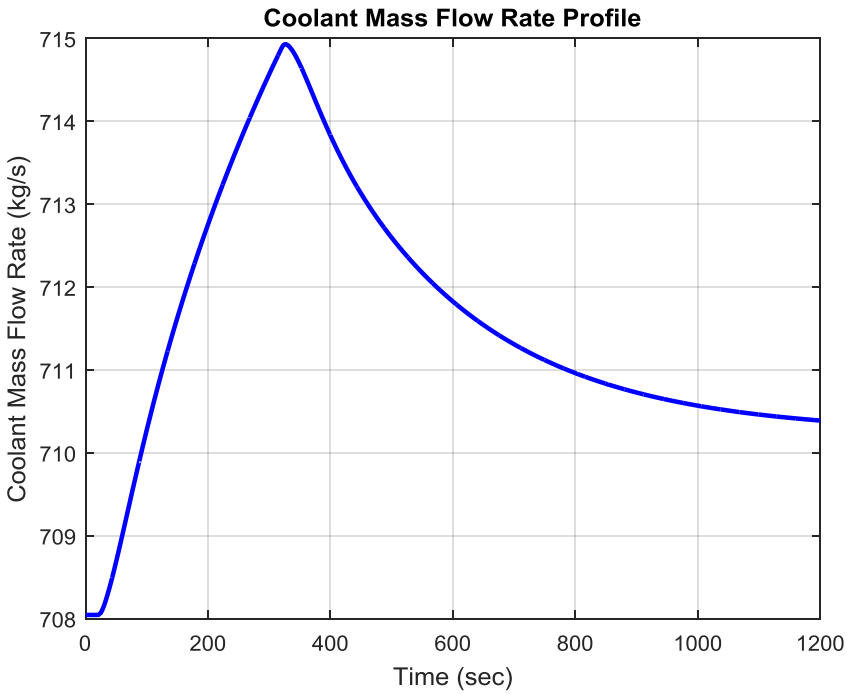

Figure 4.37 Primary coolant mass flow rate ($\dot{m}_C$) response for a ramp increase in reactor power controller reference value for single SMR unit.

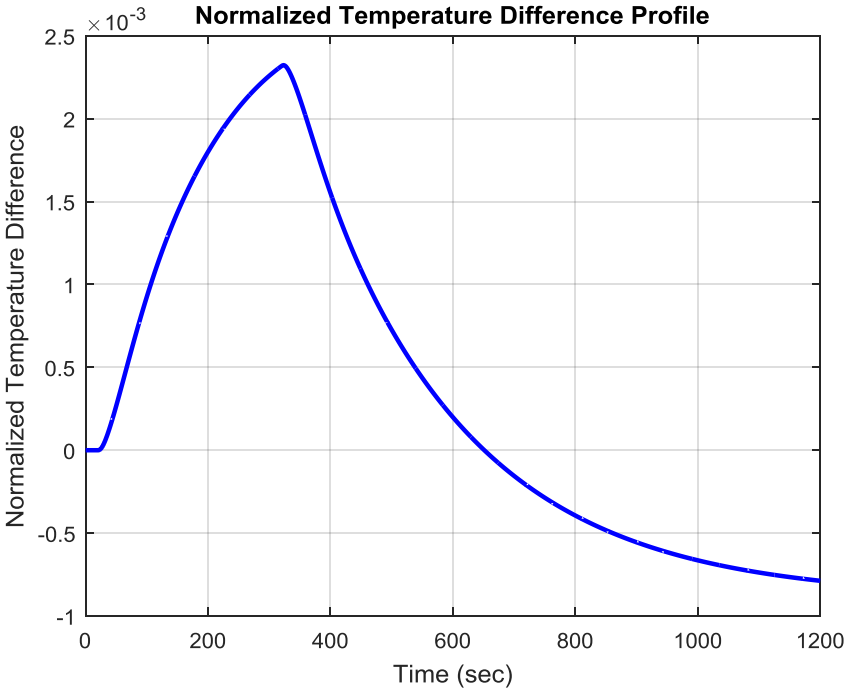

Figure 4.38 Normalized temperature difference ($T_{C2}/T_{C2,0} - T_{Ci}/T_{Ci,0}$) for a ramp increase in reactor power controller reference value for single SMR unit.

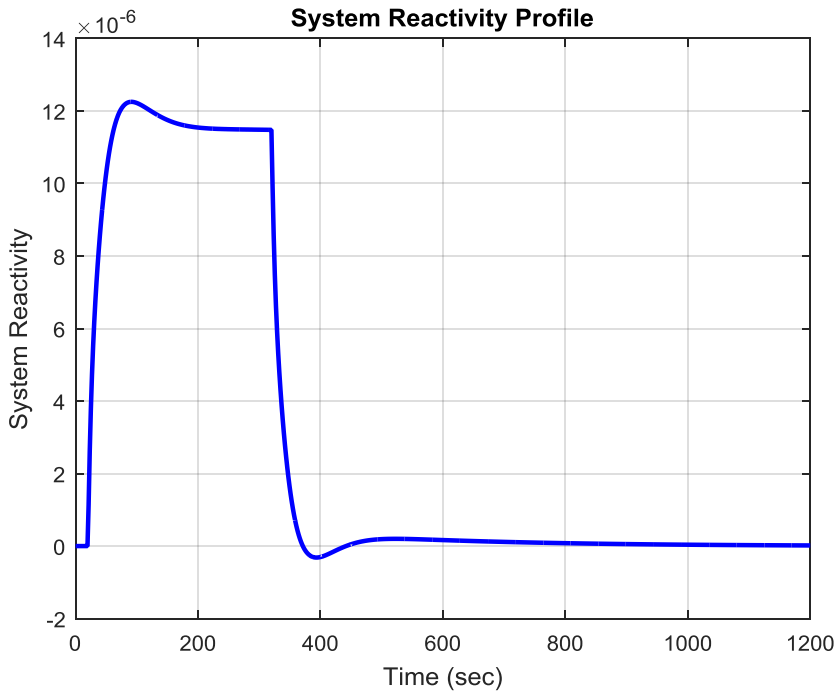

Figure 4.39 System reactivity (ρ) response for a ramp increase in reactor power controller reference value for single SMR unit.

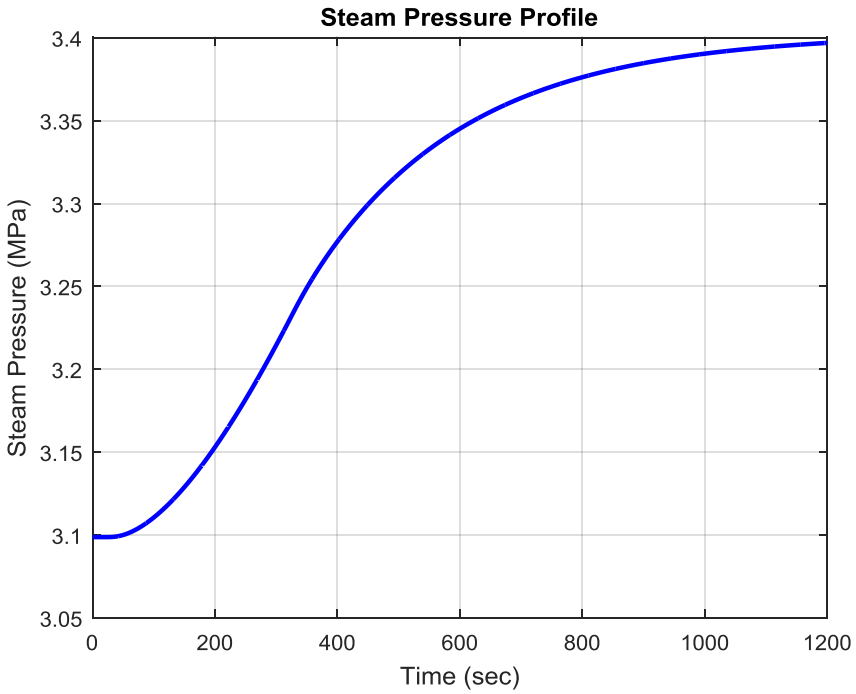

Figure 4.40 Steam pressure (p_S) response for a ramp increase in reactor power controller reference value for single SMR unit.

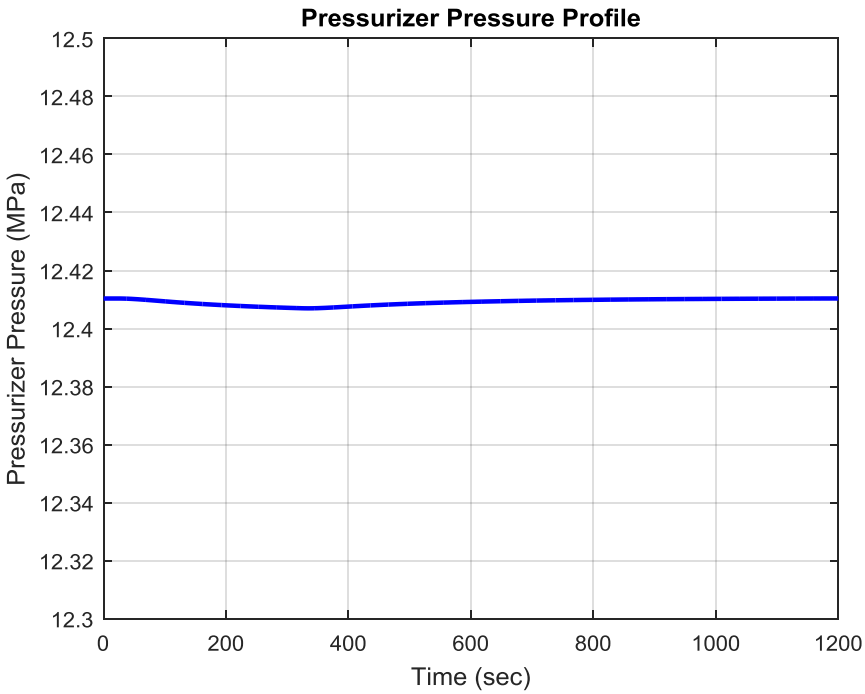

Figure 4.41 Pressurizer pressure (p_p) response for a ramp increase in reactor power controller reference value for single SMR unit.

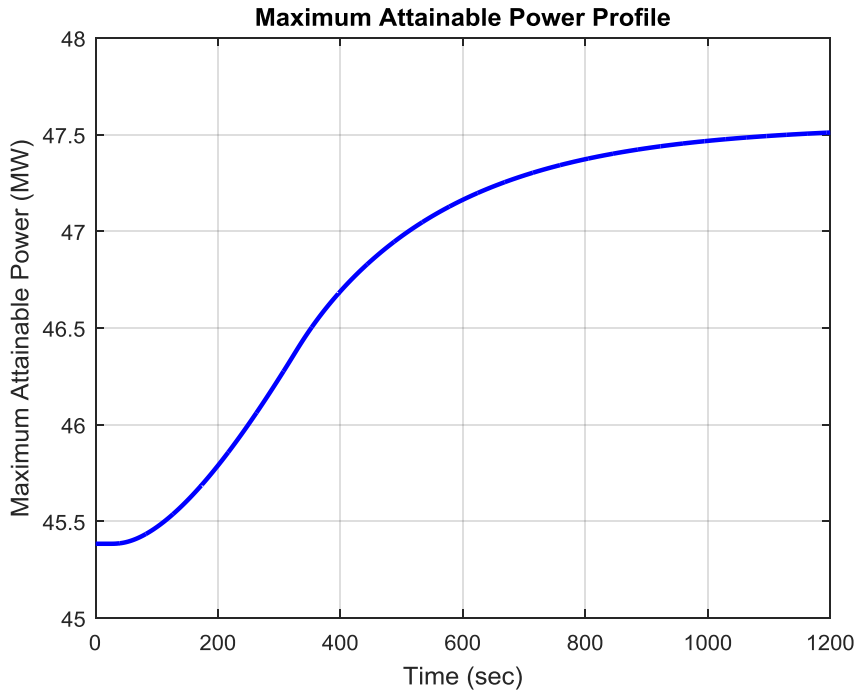

Figure 4.42 Maximum attainable power (P_m) response for a ramp increase in reactor power controller reference value for single SMR unit.

As the controller reference value starts increasing, the difference between the actual and reference values introduces an error signal to the controller which then causes the movement of the control rods to induce a positive reactivity insertion (see Figure 4.39). Accordingly, the reactor thermal power and fuel temperatures show a rise as seen in Figures 4.34 and 4.35. Following that the fuel-to-coolant heat transfer increases which explains the increase in the reactor core coolant node 2 temperature in Figure 4.36. Furthermore, the coolant mass flow rate exhibits an upward trend over the course of the ramp increase and then a downward trend for the constant controller setpoint as seen in Figure 4.37. This latter behavior is a result of the temperature difference in the primary system (see Figure 4.38) which is the main driving mechanism for the coolant mass flow rate as discussed in Section 3.1.2.3.3 by Equation (3.19).

With the increased temperature of the primary coolant, the temperature difference between the primary and secondary sides of the steam generator expands, thereby resulting in more heat transfer to the secondary side. The latter changes cause a growth in the steam generation. Thus, steam pressure increases as shown in Figure 4.40. The attainable power rises gradually and settles to a new steady-state value of 47.56 MW as depicted in Figure 4.42 which is congruent with the new, desired operation conditions discussed earlier.

The system reactivity exhibits a response similar to a square pulse shape (see Figure 4.39). This is the result of external reactivity (control rods) and internal reactivity (reactivity feedback mechanisms) acting together on the system. In other words, when the disturbance is initiated, the external reactivity is dominant and the system reactivity

increases. However, reactivity feedback mechanisms level off at a positive value after a while. When the disturbance stops, since there is no external reactivity due to the control rod movement, reactivity feedback mechanisms bring the system reactivity back to its initial, pre-transient value. Finally, Figure 4.41 shows that this perturbation has minimal impact on the pressurizer pressure.

CHAPTER 5 CONCLUSIONS AND FUTURE WORK

5.1 Research Summary

Over the last decade, there has been a growing trend in the development and commercialization of SMRs throughout the world. This interest is partially due to the smaller initial capital investment required for SMRs compared to typical power reactors. SMRs can be utilized to supply the electricity needs of remote areas with a lack of transmission infrastructure. However, this is not the only option; water desalination, general process heat for chemical or manufacturing processes, and district heating are other possible applications that can make use of SMRs with minor design alterations.

With the integral type design of SMRs, generally the reactor vessel houses not only the reactor core but also steam generators and pressurizer, and heat removal from the reactor core is accomplished by natural circulation. This feature increases safety since the primary coolant pumps, and associated failure modes are eliminated from the system.

The dynamic modeling of SMRs needs special attention and treatment due to aforementioned unique features. That is the reason that, in this work, a detailed analytical model for a passively cooled SMR is developed. The nuclear steam supply system (NSSS) model includes representations for reactor core, steam generator, pressurizer, hot leg riser and downcomer. The point kinetics equations with a single combined neutron precursor group and the models for an overall heat transfer resistance and single-phase natural circulation account for the neutronics and thermohydraulics in the reactor core region, respectively. A lumped parameter, moving-boundary approach is adopted for the once-through helical-coil heat exchanger in which boundaries between regions of

different fluid states (i.e., subcooled, boiling, and superheated) can vary over time. For the pressurizer model, an expression for the pressurizer pressure is derived from the fundamental mass, volume and energy balances. Hot leg riser and downcomer are treated as first-order lags. The NSSS model is incorporated with a turbine model which allows to observe the attainable power with given steam flow, pressure, and enthalpy as input. The overall nonlinear system is implemented in the Simulink dynamic environment. Various simulation cases are run to test the capability of the developed model to predict the dynamic response of the SMR. Finally, steady-state control programs for reactor power and pressurizer pressure are also introduced. The obtained results and the relevant discussion are presented.

5.2 Main Results of the Study

A nonlinear dynamic model for a passively cooled SMR is developed in this study. Investigation into the components (i.e., reactor core, steam generator, and pressurizer) of the model is carried out, separately, by applying perturbations to the input parameters. Comparison between the obtained simulations results and the results from References [33], [34], [41], [43], and [56] yields that the individual components of the complete model are realistic, and able to predict the dynamic response. After the validation, the combination of these models with hot leg riser and downcomer which constitute the complete model for the single SMR unit is presented. Then, the single SMR unit model is also tested by applying independent step changes into input variables. Although there is no available data for the comparison since this is an original work, the results are in good agreement with the theory.

A sliding-average-temperature control mode is adopted and a PID controller is used for reactor power and pressurizer pressure control, respectively. Dynamic simulations show that proposed control schemes are able to keep the related state variables at the desired values.

5.3 Future Work

The presented study can be extended in several directions. Possible areas in which future work may be carried out include

- A reduced order model for the linearized representation of the overall model can be obtained to develop a model based controller.
- The model developed in this study can be utilized for future studies where the goal is an analysis and control of multiple SMRs coupled to a single steam turbine−generator set.

REFERENCES

[1] International Atomic Energy Agency, Advances in Small Modular Reactor Technology Developments, p. 1, Sept. 2014.

[2] U.S. Department of Energy, Office of Nuclear Energy, Science and Technology, The history of nuclear energy, DOE/NE-0088, p. 15, 2006.

[3] S. F. Burton, and A. G. Hosler, "Small Nuclear Power Plants, Volume One, Design, Construction, and Operating Experience," U. S. Atomic Energy Commission, Tech. Rep. COO-284, Oct. 1966.

[4] World Nuclear Association, "Nuclear Power in the USA," [Online]. Available: http://www.world-nuclear.org/info/Country-Profiles/Countries-T-Z/USA--Nuclear-Power/ [Accessed: 29 Sept. 2015].

[5] U.S. Nuclear Regulatory Commission (NRC), Information Digest, 2013-2014, NUREG-1350, vol. 25, Aug. 2013.

[6] U.S. Energy Information Administration, Annual Energy Outlook 2018, U.S. Department of Energy, DOE/EIA-0383, Jun. 2008.

[7] U.S. Department of Energy, Office of Nuclear Energy, "Small Modular Nuclear Reactors," [Online]. Available: http://energy.gov/ne/nuclear-reactor-technologies/small-modular-nuclear-reactors [Accessed: 29 Sept. 2015].

[8] U.S. Department of Energy, Office of Nuclear Energy. "Energy Department Announces New Investment in Innovative Small Modular Reactor," [Online]. Available: http://energy.gov/articles/energy-department-announces-new-investment-innovative-small-modular-reactor#! [Accessed: 29 Sept. 2015].

[9] Nuclear Energy Institute, "DOE Selects NuScale Power for SMR Development Funds," [Online]. Available: http://www.nei.org/News-Media/News/News-Archives/DOE-Selects-NuScale-Power-for-SMR-Development-Fund [Accessed: 29 Sept. 2015].

[10] J. Vujić, R. M. Bergmann, R. Škoda, and M. Miletić, "Small modular reactors: Simpler, safer, cheaper?," *Energy*, vol. 45, pp. 288-295, Mar. 2012.

[11] D. T. Ingersoll, "Deliberately small reactors and the second nuclear era," *Progress in Nuclear Energy*, vol. 51, pp. 589-603, 2009.

[12] Locatelli G. SMR economics evaluation, The 4th Asia-Pacific forum on nuclear technology: the small and medium reactors. Berkeley: UC; June 17-19, 2010.

[13] World Nuclear Association, “Small Nuclear Power Reactors,” [Online]. Available: http://www.world-nuclear.org/info/Nuclear-Fuel-Cycle/Power-Reactors/Small-Nuclear-Power-Reactors/#Note_f [Accessed: 29 Sept. 2015].

[14] R. Mazzi, "CAREM: an innovative-integrated PWR," in *Proc. 18th International Conference on Structural Mechanics in Reactor Technology (SMiRT-18), Beijing, China*, pp. 4407-4415, 2005.

[15] C. P. Marcel, F. M. Acuña, P. G. Zanocco, and D. F. Delmastro, "Stability of self-pressurized, natural circulation, low thermo-dynamic quality, nuclear reactors: The stability performance of the CAREM-25 reactor," *Nuclear Engineering and Design* 265, pp. 232-243, 2013.

[16] H. Li, X. Huang, and L. Zhang, "A simplified mathematical dynamic model of the HTR-10 high temperature gas-cooled reactor with control system design purposes," *Annals of Nuclear Energy* 35, no. 9, pp. 1642-1651, 2008.

[17] Z. Wu, D. Lin, and D. Zhong, "The design features of the HTR-10," *Nuclear Engineering and Design* 218, no. 1, pp. 25-32, 2002.

[18] K. M. Kim, B. I. Lee, H. H. Cho, J. S. Park, and Y. J. Chung, "Numerical study on thermo-hydrodynamics in the reactor internals of SMART," *Nuclear Engineering and Design* 241, no. 7, pp. 2536-2543, 2011.

[19] M. H. Chang, S. K. Sim, and D. J. Lee, "SMART behavior under over-pressurizing accident conditions," *Nuclear Engineering and Design* 199, no. 1, pp. 187-196, 2000.

[20] “B&W mPower Reactor Design Overview”, BW-JAH-2010-214, Babcock & Wilcox Nuclear Energy, Lynchburg, Virginia, Jun. 2010.

[21] Z. Liu, and J. Fan, "Technology readiness assessment of small modular reactor (SMR) designs," *Progress in Nuclear Energy* 70, pp. 20-28, 2014.

[22] J. A. Halfinger, and M. D. Haggerty, "The B&W mPower™ Scalable, Practical Nuclear Reactor Design," *Nuclear Technology* 178, no. 2, pp. 164-169, 2011.

[23] R. J. Fetterman, A. W. Harkness, M. C. Smith, and C. Taylor, “An overview of the Westinghouse small modular reactor,” in *Proc. ASME 2011 Small Modular Reactors Symposium*, Washington, DC, USA, pp. 75-82.

[24] M. J., Memmott, A. W. Harkness, and J. Van Wyk, “Westinghouse Small Modular Reactor nuclear steam supply system design,” in *Proc. 2012 International Congress on Advances in Nuclear Power Plants*, Chicago, IL, USA.

[25] B. S. Triplett, E. P. Loewen, and B. J. Dooies, "PRISM: a competitive small modular sodium-cooled reactor," *Nuclear Technology* 178, no. 2, pp. 186-200, 2012.

[26] A. Makhijani, "Light water designs of small modular reactors: facts and analysis," Takoma Park: Institute for Energy and Environmental Research, 2013.

[27] J. N. Reyes Jr, and P. Lorenzini, "NuScale Power: A modular, scalable approach to commercial nuclear power," *Nuclear News* 53, no. 7, pp. 97-104, 2010.

[28] "NuScale Plant Design Overview," RP-1114-9375, Rev. 0, NuScale Power, LLC, Corvallis, Oregon, Nov. 2014.

[29] International Atomic Energy Agency (IAEA), "NuScale Power Modular and Scalable Reactor," Advanced Reactor Information System database, [Online]. Available: https://aris.iaea.org/PDF/NuScale.pdf [Accessed: 2 Oct. 2015].

[30] "Trial Application of the Facility Safeguardibility Assessment Process to the NuScale SMR Design," DE-AC05-76RL01830, Rev 1, Pacific Northwest National Laboratory, Jan. 2013.

[31] "Multi-Application Small Light Water Reactor Final Report," INEEL/EXT-04-01626, Idaho National Engineering and Environmental Laboratory, Idaho Falls, Idaho, Dec. 2003.

[32] NuScale Power, "NuScale International Test Programs," [Online]. Available: http://www.nuscalepower.com/our-technology/test-programs/international-test-programs [Accessed: 26 Oct. 2015].

[33] T. W. Kerlin, E. M. Katz, J. G. Thakkar, and J. E. Strange, "Theoretical and experimental dynamic analysis of the H. B. Robinson nuclear plant," *Nuclear Technology*, vol. 30, pp. 299-316, Sept. 1976.

[34] J. G. Thakkar, "Correlation of theory and experiment for the dynamics of a pressurized water reactor," M.S. thesis, Dept. Nuc. Eng., Univ. Tennessee, Knoxville, 1975.

[35] R. J. Onega, and K. E. Karcher, "Nonlinear dynamics of a pressurized water reactor core," *Nuclear Science and Engineering* 61, no. 2, pp. 276-282, 1976.

[36] Y. Zvirin, "A review of natural circulation loops in pressurized water reactors and other systems," *Nuclear Engineering and Design* 67, pp. 203-225, 1981.

[37] C. P. Marcel, H. F. Furci, D. F. Delmastro, and V. P. Masson, "Phenomenology involved in self-pressurized, natural circulation, low thermo-dynamic quality, nuclear reactors: The thermal–hydraulics of the CAREM-25 reactor," *Nuclear Engineering and Design* 254, pp. 218-227, 2013.

[38] B. Jang, M. H. Kim, and G. Jeun, "Experimental and computational investigation of a natural circulation system in Regional Energy Reactor-10MW th," *Nuclear Engineering and Design* 241, no. 6, pp. 2214-2223, 2011.

[39] A. Cammi, R. Ponciroli, A. B. di Tigliole, G. Magrotti, M. Prata, D. Chiesa, and E. Previtali, "A zero dimensional model for simulation of TRIGA Mark II dynamic response." *Progress in Nuclear Energy* 68, pp. 43-54, 2013.

[40] D. Chiesa, M. Clemenza, M. Nastasi, S. Pozzi, E. Previtali, G. Scionti, M. Sisti, M. Prata, A. Salvini, and A. Cammi, "Measurement and simulation of the neutron flux distribution in the TRIGA Mark II reactor core," *Annals of Nuclear Energy* 85, pp. 925-936, 2015.

[41] A. Ray, and H. F. Bowman, "A nonlinear dynamic model of a once-through subcritical steam generator," *Journal of Dynamic Systems, Measurement, and Control* 98, no. 3, pp. 332-339, 1976.

[42] M. A. Abdalla, "A four-region, moving-boundary model of a once-through, helical-coil steam generator," *Annals of Nuclear Energy* 21, no. 9, pp. 541-562, 1994.

[43] H. Li, X. Huang, and L. Zhang, "A lumped parameter dynamic model of the helical coiled once-through steam generator with movable boundaries," *Nuclear Engineering and Design* 238, no. 7, pp. 1657-1663, 2008.

[44] Z. Dong, "A Differential-Algebraic Model for the Once-Through Steam Generator of MHTGR-Based Multimodular Nuclear Plants," *Mathematical Problems in Engineering*, vol. 2015, pp. 1-12, 2015.

[45] K. E. Holbert, and N. Venkatesh, "Valid ranges for using the cross-power spectral density phase angle for moderator temperature coefficient sign determination," *Nuclear Science and Engineering* 119, no. 3, pp. 203-211, 1995.

[46] T. W. Kerlin, "Dynamic Analysis and Control of Pressurized Water Reactors," *Control and Dynamic Systems, Advances in Theory and Applications*, edited by C.T. Leondes, Academic Press, vol. 14, 1978, pp. 103-212.

[47] J. J. Duderstadt, and L. J. Hamilton, *Nuclear Reactor Analysis*, New York: John Wiley and Sons, Inc., 1976.

[48] "NuScale Codes and Methods Framework Description Report", NP-TR-0812-1682, Rev. 0, NuScale Power, LLC, Corvallis, Oregon, Jan. 2013.

[49] J. R. Lamarsh, and A. J. Baratta, *Introduction to Nuclear Engineering*, 3rd edition, New Jersey: Prentice-Hall, 2001.

[50] N. E. Todreas, and M. S. Kazimi, *Nuclear Systems: Thermal Hydraulic Fundamentals*. vol. 1. CRC Press, 2011.

[51] T. L. Bergman, A. S. Lavine, F. P. Incropera, and D. P. Dewit, *Fundamentals of Heat and Mass Transfer*. John Wiley & Sons, 2007.

[52] M. M. El-Wakil, *Powerplant Technology*, New York: McGraw-Hill, 2002. pp. 404-407.

[53] X. He, S. Liu, and H. Asada, "Modeling of vapor compression cycles for advanced controls in HVAC systems," in *Proc. American Control Conference*, Seattle, WA, USA, vol. 5, pp. 3664-3668, 1995.

[54] M. Willatzen, N. B. O. L. Pettit, and L. Ploug-Sørensen, "A general dynamic simulation model for evaporators and condensers in refrigeration. Part I: moving-boundary formulation of two-phase flows with heat exchange," *International Journal of Refrigeration* 21, no. 5, pp. 398-403, 1998.

[55] L. Zhao, L. Guo, B. Bai, Y. Hou, and X. Zhang, "Convective boiling heat transfer and two-phase flow characteristics inside a small horizontal helically coiled tubing once-through steam generator," *International Journal of Heat and Mass Transfer* 46, no. 25, pp. 4779-4788, 2003.

[56] J. M. Jensen, and H. Tummescheit, "Moving boundary models for dynamic simulations of two-phase flows," in *Proc. 2nd International Modelica Conference*, Oberpfaffenhofen, Germany, pp. 235-244, Mar. 2002.

[57] M. R. A. Ali, "Lumped parameter, state variable dynamic models for U-tube circulation type nuclear steam generators," Ph.D. dissertation, Dept. Nuc. Eng., Univ. Tennessee, Knoxville, 1976.

[58] B. P. Rasmussen, and A. G. Alleyne, "*Dynamic modeling and advanced control of air conditioning and refrigeration systems*" Air Conditioning and Refrigeration Center, College of Engineering. University of Illinois at Urbana-Champaign, 2006.

[59] R. J. Belles, "Key reactor system components in integral pressurized water reactors (iPWRs)," *Handbook of Small Modular Nuclear Reactors*, edited by M. D. Carelli, and D. T. Ingersoll, Woodhead Publishing, 2014, pp. 109-111.

[60] T. W. Kerlin, and E. M. Katz, "Pressurized water reactor modeling for long-term power system dynamics simulation," Electric Power Research Institute (EPRI), Palo Alto, CA, Tech. Rep. EL-3087, May 1983.

[61] U.S. Environmental Protection Agency (EPA), Combined Heat and Power Partnership (CHP), Catalog of CHP Technologies, Mar. 2015.

[62] Mathworks, “SIMULINK Dynamic System Simulation Language User’s Guide,” 2008.

[63] “Westhinghouse Technology Systems Manual Section 1.2,” [Online]. Available: pbadupws.nrc.gov/docs/ML1122/ML11223A195.pdf [Accessed: 25 Feb. 2013].

[64] M. A. Schultz, *Control of Nuclear Reactors and Power Plants*, New York: McGraw-Hill, 1955, pp. 128-179.

[65] L. E. Weaver, “Reactor Control,” *Nuclear Power Safety*, edited by J. H. Rust, and L. E. Weaver, Pergamon Press, 1976, pp. 169-207.

[66] “Part 1: Introduction to Reactor Technology – PWR,” [Online]. Available: http://pbadupws.nrc.gov/docs/ML1215/ML12159A222.pdf [Accessed: 25 Feb. 2016].

[67] Y. E. Kim, J. W. Park, and J. Cleveland, “Thermophysical properties database of materials for light water and heavy water reactors,” International Atomic Energy Agency, Vienna, Austria, Tech. Rep. IAEA-TECDOC-1496, Jun. 2006.

[68] S. E. Arda, "Implementing a Nuclear Power Plant Model for Evaluating Load-Following Capability on a Small Grid," M.S. thesis, School of Elect., Comput. and Energy Eng., Arizona State Univ., 2013.

[69] Mathworks, “X Steam, Thermodynamic properties of water and steam,” 2007.

[70] “Inconel alloy 690,” [Online]. Available: http://www.specialmetals.com/assets/documents/alloys/inconel/inconel-alloy-690.pdf [Accessed: 20 Oct. 2015].

APPENDIX A

REACTOR CORE PARAMETERS AND CALCULATIONS

A.1 Rector Core Parameters

Table A.1 Reactor core parameters

Variable	Description	Value	Source
P	Reactor thermal power	160 MWt	Reference [29]
β	Delayed neutron fraction	0.007	References [33], [45]
Λ	Neutron generation time	20 μs	References [33], [45]
λ	Delayed neutron precursor decay constant	0.1 s^{-1}	References [33], [45]
α_F	Fuel temperature coefficient of reactivity	-2.16×10^{-5}/°C	References [33], [45]
α_C	Coolant temperature coefficient of reactivity	-1.8×10^{-4}/°C	References [33], [45]
α_P	Primary pressure coefficient of reactivity	1.08×10^{-6}/°C	References [33], [45]
$c_{p,F}$	Specific heat of fuel	0.467 kJ/(kg·°C)	Reference [67]
f_d	Fraction of power produced in fuel	0.975	Reference [68]
p	Pin pitch	1.26 cm	Reference [48]
d	Fuel rod outside diameter	0.95 cm	Reference [48]
H	Active core height	2 m	Reference [48]
n_r	Total number of rods	10693	Reference [48]
ρ_C	Coolant density (12.76 MPa and 268.3 °C)	780.3 kg/m^3	Reference [69]
V_C	Coolant volume in core	1.879 m^3	Calculated
m_C	Coolant mass in core	1466 kg	Calculated
r_f	Fuel pellet radius	0.409 cm	Reference [48]
n_{fr}	Total number of fuel rods	9768	Reference [48]
ρ_F	Fuel density	10.96 g/cm^3	Reference [67]

m_F	Total fuel mass	11252 kg	Calculated
h_g	Fuel gap heat transfer coefficient	5678 W/(m^2·°C)	Reference [49]
k_f	Fuel thermal conductivity	4.15 W/m·°C	Reference [49]
k_c	Cladding thermal conductivity	19.04 W/m·°C	Reference [49]
t_g	Gap thickness	0.057 cm	Reference [48]
t_c	Cladding thickness	0.95 cm	Reference [48]
D_e	Equivalent diameter	1.178 cm	Calculated
$\dot{m}_C$	Coolant flow rate	708 kg/s	Reference [30]
v	Mean coolant velocity	0.966 m/s	Calculated
μ	Coolant dynamic viscosity (12.76 MPa and 268.3 °C)	0.361 kg/(m·hr)	Reference [69]
k	Coolant thermal conductivity (12.76 MPa and 268.3 °C)	0.598 W/(m·°C)	Reference [69]
$c_{p,C}$	Specific heat of coolant (12.76 MPa and 268.3 °C)	4.96 kJ/(kg·°C)	Reference [69]
T_{C1}	Average core coolant temperature	268.3 °C	Reference [30]
h_s	Cladding surface heat transfer coefficient	13730 W/(m^2·°C)	Calculated
A_{FC}	Effective heat transfer area	583 m^2	Calculated
U_{FC}	Fuel-to-coolant heat transfer coefficient	1135 W/(m^2·°C)	Calculated
T_F	Average fuel temperature	504 °C	Calculated

A.1.1 Coolant mass in reactor core

Figure A.1 shows the equivalent coolant channels in the reactor core for a square fuel lattice. Based on this configuration, the calculation of the coolant flow in the core is performed as follows:

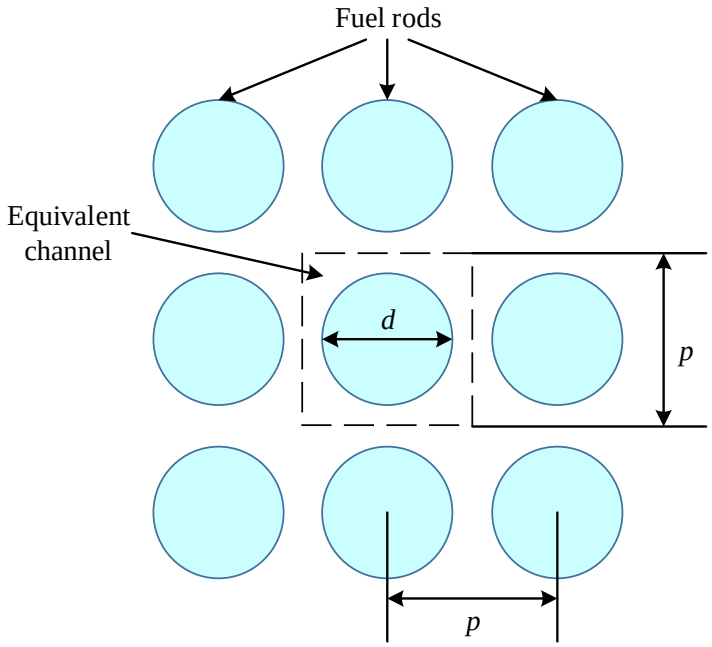

Figure A.1 Equivalent coolant channels in a square fuel lattice.

$$V_C = \left(p^2 - \pi \frac{d^2}{4} \right) H n_r = \left[(1.26\,\text{cm})^2 - \pi (0.475\,\text{cm})^2 \right] \times 200\,\text{cm} \times 10693 = 1.879\,\text{m}^3 \quad \text{(A.1)}$$

$$m_C = V_C \rho_C = 1.879\,\text{m}^3 \times 780.3 \frac{\text{kg}}{\text{m}^3} = 1466\,\text{kg} \quad \text{(A.2)}$$

A.1.2 Fuel mass in reactor core

The mass of the fuel inside the core is calculated by

$$m_F = \left(\pi r_f^2 H \right) n_{fr} \rho_F = \left[\pi (0.409\,\text{cm})^2 \times 200\,\text{cm} \right] \times 9768 \times 10.96 \frac{\text{g}}{\text{cm}^3} = 11252\,\text{kg} \quad \text{(A.3)}$$

A.1.3 Fuel-to-coolant heat transfer coefficient

The overall heat transfer resistance is defined in Section 3.1.2.2 as $R = 1/(UA)_{FC}$ and Equation (3.9) gives an expression to calculate the heat transfer resistance. The only unknown variable in that equation is the cladding surface heat transfer coefficient which can be determined by Equation (3.10). However, the equivalent diameter (D_e) and the Reynolds (Re) and Prandtl (Pr) numbers should be calculated.

$$D_e = 4\frac{\left[p^2 - \pi\left(\frac{d}{2}\right)^2\right]}{\pi d} = 4\frac{\left[(1.26\,\text{cm})^2 - \pi(0.475\,\text{cm})^2\right]}{\pi(0.95\,\text{cm})} = 1.178\,\text{cm} \tag{A.4}$$

$$v = \frac{\dot{m}_C H}{m_C} = \frac{(708\,\text{kg}\cdot\text{s}^{-1})\times(2\,\text{m})}{1466\,\text{kg}} = 0.966\frac{\text{m}}{\text{s}} \tag{A.5}$$

$$\text{Re} = \frac{D_e v \rho_C}{\mu} = \frac{(1.178\,\text{cm})\times(0.966\,\text{m}\cdot\text{s}^{-1})\times(780.3\,\text{kg}\cdot\text{m}^{-3})}{(0.361\,\text{kg}\cdot\text{m}^{-1}\cdot\text{hr}^{-1})} = 88548 \tag{A.6}$$

$$\text{Pr} = \frac{c_{p,C}\mu}{k} = \frac{(4.96\,\text{kJ}\cdot\text{kg}^{-1}\cdot^{\circ}\text{C}^{-1})\times(0.361\,\text{kg}\cdot\text{m}^{-1}\cdot\text{hr}^{-1})}{(0.598\,\text{W}\cdot\text{m}^{-1}\cdot^{\circ}\text{C}^{-1})} = 0.8317 \tag{A.7}$$

Replacing all parameters in Equation (3.10) with their values yields that

$$h_s = 0.0317\frac{(0.598\,\text{W}\cdot\text{m}^{-1}\cdot^{\circ}\text{C}^{-1})}{1.178\,\text{cm}}88548^{0.3}0.8317^{1/3} = 13730\,\text{W}\cdot\text{m}^{-2}\cdot^{\circ}\text{C}^{-1} \tag{A.8}$$

then by utilizing Equation (3.9), $1/R = 661705\ \text{W}\cdot^{\circ}\text{C}^{-1}$. The effective heat transfer area and fuel-to-coolant heat transfer coefficient can be calculated as

$$A_{FC} = (\pi d H)\times n_{fr} = \pi(0.95\,\text{cm})\times(200\,\text{cm})\times 9768 = 583\,\text{m}^2 \tag{A.9}$$

$$U_{FC} = \frac{1}{RA_{FC}} = 661705\,\mathrm{W}\cdot^{\circ}\mathrm{C}^{-1} \times \frac{1}{583\,\mathrm{m}^2} = 1135\,\mathrm{W}\cdot\mathrm{m}^{-2}\cdot^{\circ}\mathrm{C}^{-1} \tag{A.10}$$

Finally, average fuel temperature can be found by Equation (3.7)

$$T_F = f_d PR - T_{C1} = 0.975 \times 160 \cdot 10^6\,\mathrm{W} \times \frac{1}{661705\,\mathrm{W}\cdot^{\circ}\mathrm{C}^{-1}} + 268.3\,^{\circ}\mathrm{C} = 504^{\circ}\mathrm{C} \tag{A.11}$$

APPENDIX B

STEAM GENERATOR PARAMETERS AND CALCULATIONS

B.1 Derivation of Secondary Side Equations

B.1.1 Subcooled region

Integration of the mass balance equation (Equation 3.24) over the subcooled region yields that

$$\int_0^{L_1} \frac{\partial A_S \rho}{\partial t} \partial z + \int_0^{L_1} \frac{\partial \dot{m}_S}{\partial z} \partial z = 0 \tag{B.1}$$

$$A_S \frac{d}{dt} \int_0^{L_1} \rho dz - A_S \rho_{(L_1)} \frac{dL_1}{dt} + \dot{m}_{S,12} - \dot{m}_{S,i} = 0 \tag{B.2}$$

where $\rho_{(L1)}$ is the saturated liquid density ρ_f. In addition, it is assumed that average enthalpy and density of the liquid for the subcooled region equal $h_1 = 0.5(h_i + h_f)$ and $\rho_1 = \rho(p_S, h_1)$, respectively.

The rate of change of mass in the liquid region, first term of Equation (B.2), can be evaluated as:

$$A_S \frac{d}{dt} \int_0^{L_1} \rho dz = A_S \frac{d}{dt} \left[L_1 \rho_1 - 0 \right] = A_S \rho_1 \frac{dL_1}{dt} + A_S L_1 \frac{d\rho_1}{dt} \tag{B.3}$$

then Equation (B.2) can be rewritten as:

$$A_S \left\{ \left(\rho_1 - \rho_f \right) \frac{dL_1}{dt} + L_1 \frac{d\rho_1}{dt} \right\} = \dot{m}_{S,i} - \dot{m}_{S,12} \tag{B.4}$$

The time derivative of the average liquid density equals the following expression by using the chain rule.

$$\begin{aligned}\frac{d\rho_1}{dt} &= \left.\frac{\partial\rho_1}{\partial p_S}\right|_{h_1}\frac{dp_S}{dt} + \left.\frac{\partial\rho_1}{\partial h_1}\right|_{\rho_S}\frac{dh_1}{dt} \\ &= \left.\frac{\partial\rho_1}{\partial p_S}\right|_{h_1}\frac{dp_S}{dt} + \left.\frac{\partial\rho_1}{\partial h_1}\right|_{\rho_S}\frac{d}{dt}\left[\frac{1}{2}\left(h_i + h_f\right)\right] \\ &= \left(\left.\frac{\partial\rho_1}{\partial p_S}\right|_{h_1} + \frac{1}{2}\left.\frac{\partial\rho_1}{\partial h_1}\right|_{\rho_S}\frac{\partial h_f}{\partial p_S}\right)\frac{dp_S}{dt} + \frac{1}{2}\left.\frac{\partial\rho_1}{\partial h_1}\right|_{\rho_S}\frac{dh_i}{dt}\end{aligned} \tag{B.5}$$

Finally, inserting Equation (B.5) into Equation (B.4) gives the mass balance equation for the subcooled region which is

$$A_S\left\{(\rho_1-\rho_f)\frac{dL_1}{dt} + L_1\left(\left.\frac{\partial\rho_1}{\partial p_S}\right|_{h_1} + \frac{1}{2}\left.\frac{\partial\rho_1}{\partial h_1}\right|_{p_S}\frac{\partial h_f}{\partial p_S}\right)\frac{dp_S}{dt} + \frac{1}{2}L_1\left.\frac{\partial\rho_1}{\partial h_1}\right|_{p_S}\frac{dh_i}{dt}\right\} = \dot{m}_{S,i} - \dot{m}_{S,12} \tag{B.6}$$

In a similar manner, integration of the energy balance equation (Equation 3.25) over the subcooled region gives that

$$\int_0^{L_1}\frac{\partial\left(A_S\rho h - A_S p\right)}{\partial t} + \int_0^{L_1}\frac{\partial\dot{m}_S h}{\partial z} = \int_0^{L_1}\pi d_i\alpha_i\left(T_M - T_S\right) \tag{B.7}$$

$$A_S\frac{d}{dt}\int_0^{L_1}(\rho h - p)dz - A_S\left[\rho_{(L_1)}h_{(L_1)} - p_{(L_1)}\right]\frac{dL_1}{dt} + \dot{m}_{S,12}h_f - \dot{m}_{S,i}h_i = \pi\, d_i\alpha_{i1}(T_{M1} - T_{S1}) \tag{B.8}$$

and evaluating the first term of Equation (B.8) results in

$$\begin{aligned}A_S\frac{d}{dt}\int_0^{L_1}\left(\rho h - p\right)dz = A_S\frac{d}{dt}\left[\left(\rho_1 h_1 - p_S\right)L_1 - 0\right] &= A_S\frac{d}{dt}\left(\rho_1 h_1 L_1\right) - A_S p_S\frac{dL_1}{dt} - A_S L_1\frac{dp_S}{dt} \\ &= A_S\left(\rho_1 h_1\frac{dL_1}{dt} + L_1\frac{d}{dt}\left(\rho_1 h_1\right) - p_S\frac{dL_1}{dt} - L_1\frac{dp_S}{dt}\right) \\ &= A_S\left(\rho_1 h_1\frac{dL_1}{dt} + L_1 h_1\frac{d\rho_1}{dt} + L_1\rho_1\frac{dh_1}{dt} - p_S\frac{dL_1}{dt} - L_1\frac{dp_S}{dt}\right)\end{aligned} \tag{B.9}$$

then, replacing the average liquid enthalpy and the rate of change of the average liquid density in Equation (B.9) with their equivalences yields the equation below.

$$A_S \frac{d}{dt}\int_0^{L_1}(\rho h - p)dz = A_S\left\{(\rho_1 h_1 - p_S)\frac{dL_1}{dt} - L_1\frac{dp_S}{dt}\right\} + A_S\left\{L_1 h_1\left[\left(\left.\frac{\partial\rho_1}{\partial p_S}\right|_{h_1} + \frac{1}{2}\left.\frac{\partial\rho_1}{\partial h_1}\right|_{\rho_S}\frac{\partial h_f}{\partial p_S}\right)\frac{dp_S}{dt} + \frac{1}{2}\left.\frac{\partial\rho_1}{\partial h_1}\right|_{\rho_S}\frac{dh_i}{dt}\right] + \frac{1}{2}L_1\rho_1\left(\frac{dh_i}{dt} + \frac{dh_f}{dt}\right)\right\} \quad \text{(B.10)}$$

Combining Equations (B.8) and (B.10) gives the energy balance equation for the subcooled region.

$$A_S\left\{(\rho_1 h_1 - p_S)\frac{dL_1}{dt} + L_1 h_1\left[\left(\left.\frac{\partial\rho_1}{\partial p_S}\right|_{h_1} + \frac{1}{2}\left.\frac{\partial\rho_1}{\partial h_1}\right|_{\rho_S}\frac{\partial h_f}{\partial p_S}\right)\frac{dp_S}{dt} + \frac{1}{2}\left.\frac{\partial\rho_1}{\partial h_1}\right|_{\rho_S}\frac{dh_i}{dt}\right] + \frac{1}{2}L_1\rho_1\left(\frac{dh_i}{dt} + \frac{dh_f}{dt}\right)\right\} - A_S L_1\frac{dp_S}{dt} - A_S\rho_f h_f\frac{dL_1}{dt} + A_S p_S\frac{dL_1}{dt} = -\dot{m}_{S,12}h_f + \dot{m}_{S,i}h_i + \pi d_i\alpha_{i1}(T_{M1} - T_{S1}) \quad \text{(B.11)}$$

After algebraic manipulations, the final form of the energy conservation equation is obtained as:

$$A_S\left\{(\rho_1 h_1 - \rho_f h_f)\frac{dL_1}{dt} + \frac{1}{2}L_1\left(\rho_1 + h_1\left.\frac{\partial\rho_1}{\partial h_1}\right|_{p_S}\right)\frac{dh_i}{dt} + L_1\left(\frac{\rho_1}{2}\frac{\partial h_f}{\partial p_S} + h_1\left(\left.\frac{\partial\rho_1}{\partial p_S}\right|_{h_1} + \frac{1}{2}\left.\frac{\partial\rho_1}{\partial h_1}\right|_{p_S}\frac{\partial h_f}{\partial p_S}\right) - 1\right)\frac{dp_S}{dt}\right\} = \dot{m}_{S,i}h_i - \dot{m}_{S,12}h_f + \pi d_i\alpha_{i1}(T_{M1} - T_{S1}) \quad \text{(B.12)}$$

B.1.2 Two-phase region

The mass balance equation for the two-phase region is derived by integrating the general mass balance equation over the region and, then, applying *Leibnitz theorem*.

$$\int_{L_1}^{L_1+L_2}\frac{\partial A_S\rho}{\partial t}\partial z + \int_{L_1}^{L_1+L_2}\frac{\partial\dot{m}_S}{\partial z}\partial z = 0 \quad \text{(B.13)}$$

$$A_S\frac{d}{dt}\int_{L_1}^{L_1+L_2}\rho dz + A_S\rho_{(L_1)}\frac{dL_1}{dt} - A_S\rho_{(L_1+L_2)}\frac{d(L_1+L_2)}{dt} + \dot{m}_{S,23} - \dot{m}_{S,12} = 0 \quad \text{(B.14)}$$

where $\rho_{(L1+L2)}$ is the saturated vapor density ρ_g.

The rate of change of mass in the two-phase region, first term of Equation (B.14), can be evaluated as:

$$A_S \frac{d}{dt}\int_{L_1}^{L_1+L_2} \rho dz = A_S \frac{d}{dt}\left[(L_1+L_2)\rho_2 - L_1\rho_2\right] = A_S\rho_2\frac{dL_2}{dt} + A_S L_2 \frac{d\rho_2}{dt} \tag{B.15}$$

where ρ_2 is the two-phase region mean density and equals to $\rho_2 = \bar{\gamma}\rho_g + (1-\bar{\gamma})\rho_f$. Using this equity, Equation (B.15) can be rewritten as:

$$A_S \frac{d}{dt}\int_{L_1}^{L_1+L_2} \rho dz = A_S\rho_2\frac{dL_2}{dt} + A_S L_2\left[\bar{\gamma}\frac{\partial\rho_g}{\partial p_S} + (1-\bar{\gamma})\frac{\partial\rho_f}{\partial p_S}\right]\frac{dp_S}{dt} \tag{B.16}$$

and, the combination of Equations (3.14) and (3.16) gives the mass balance equation in the form of

$$\begin{aligned} A_S\rho_2\frac{dL_2}{dt} + A_S L_2\left[\bar{\gamma}\frac{\partial\rho_g}{\partial p_S} + (1-\bar{\gamma})\frac{\partial\rho_f}{\partial p_S}\right]\frac{dp_S}{dt} + A_S\rho_f\frac{dL_1}{dt} - A_S\rho_g\frac{dL_1}{dt} - A_S\rho_g\frac{dL_2}{dt} \\ = \dot{m}_{S,12} - \dot{m}_{S,23} \end{aligned} \tag{B.17}$$

and, after substituting ρ_2 with its equivalence result in the final form of the mass balance equation for the two-phase region.

$$A_S\left\{(\rho_f-\rho_g)\frac{dL_1}{dt} + (1-\bar{\gamma})(\rho_f-\rho_g)\frac{dL_2}{dt} + L_2\left(\bar{\gamma}\frac{\partial\rho_g}{\partial p_S} + (1-\bar{\gamma})\frac{\partial\rho_f}{\partial p_S}\right)\frac{dp_S}{dt}\right\} = \dot{m}_{S,12} - \dot{m}_{S,23} \tag{B.18}$$

The same methodology is applied to the general energy balance equation in order to obtain the energy conservation equation of the two-phase region.

$$\int_{L_1}^{L_1+L_2}\frac{\partial(A_S\rho h - A_S p)}{\partial t} + \int_{L_1}^{L_1+L_2}\frac{\partial\dot{m}_S h}{\partial z} = \int_{L_1}^{L_1+L_2}\pi d_i\alpha_i(T_M - T_S) \tag{B.18}$$

$$A_S \frac{d}{dt}\int_{L_1}^{L_1+L_2}(\rho h - p)dz - A_S\left[\rho_{(L_2+L_1)}h_{(L_2+L_1)} - p_{(L_2+L_1)}\right]\frac{d(L_2+L_1)}{dt} + A_S\left[\rho_{(L_1)}h_{(L_1)} - p_{(L_1)}\right]\frac{dL_1}{dt} + \dot{m}_{S,23}h_g - \dot{m}_{S,12}h_f = \pi d_i \alpha_{i2}(T_{M2} - T_{S2}) \quad \text{(B.19)}$$

An expression can be obtained for the integral term of Equation (B.19) as follows:

$$A_S \frac{d}{dt}\int_{L_1}^{L_1+L_2}(\rho h - p)dz = A_S \frac{d}{dt}\left[\left(\bar{\gamma}\rho_g h_g + (1-\bar{\gamma})\rho_f h_f - p_S\right)L_2\right]$$
$$= A_S\left(L_2\left[\bar{\gamma}\frac{\partial(\rho_g h_g)}{\partial p_S} + (1-\bar{\gamma})\frac{\partial(\rho_f h_f)}{\partial p_S}\right]\right)\frac{dp_S}{dt} + \quad \text{(B.20)}$$
$$A_S\left(\bar{\gamma}\rho_g h_g + (1-\bar{\gamma})\rho_f h_f\right)\frac{dL_2}{dt} - A_S p_S \frac{dL_2}{dt} - A_S L_2 \frac{dp_S}{dt}$$

where $\frac{\partial(\rho_g h_g)}{\partial p_S} = h_g \frac{\partial \rho_g}{\partial p_S} + \rho_g \frac{\partial h_g}{\partial p_S}$, and $\frac{\partial(\rho_f h_f)}{\partial p_S} = h_f \frac{\partial \rho_f}{\partial p_S} + \rho_f \frac{\partial h_f}{\partial p_S}$. The combination of Equations (B.19) and (B.20) results in the energy balance equation.

$$A_S\left(L_2\left[\bar{\gamma}\frac{\partial(\rho_g h_g)}{\partial p_S} + (1-\bar{\gamma})\frac{\partial(\rho_f h_f)}{\partial p_S}\right]\right)\frac{dp_S}{dt} + A_S\left(\bar{\gamma}\rho_g h_g + (1-\bar{\gamma})\rho_f h_f\right)\frac{dL_2}{dt}$$
$$- A_S p_S \frac{dL_2}{dt} - A_S L_2 \frac{dp_S}{dt} - A_S\left[\rho_g h_g - p_S\right]\frac{d(L_1+L_2)}{dt} + A_S\left[\rho_f h_f - p_S\right]\frac{dL_1}{dt} + \quad \text{(B.21)}$$
$$\dot{m}_{S,23}h_g - \dot{m}_{S,12}h_f = \pi d_i \alpha_{i2}(T_{M2} - T_{S2})$$

After rearranging Equation (B.21), the final form of the energy balance equation is

$$A_S\left\{(\rho_f h_f - \rho_g h_g)\frac{dL_1}{dt} + (1-\bar{\gamma})(\rho_f h_f - \rho_g h_g)\frac{dL_2}{dt} + L_2\left(\bar{\gamma}\frac{\partial(\rho_g h_g)}{\partial p_S} + (1-\bar{\gamma})\frac{\partial(\rho_f h_f)}{\partial p_S} - 1\right)\frac{dp_S}{dt}\right\} = \dot{m}_{S,12}h_f - \dot{m}_{S,23}h_g + \pi d_i \alpha_{i2}(T_{M2} - T_{S2}) \quad \text{(B.22)}$$

B.1.3 Superheated region

The mass balance equation for the superheated region is obtained after the following steps:

$$\int_{L_1+L_2}^{L} \frac{\partial A_S \rho}{\partial t} \partial z + \int_{L_1+L_2}^{L} \frac{\partial \dot{m}_S}{\partial z} \partial z = 0 \tag{B.23}$$

$$A_S \frac{d}{dt} \int_{L_1+L_2}^{L} \rho dz + A_S \rho_{(L_1+L_2)} \frac{d(L_1+L_2)}{dt} + \dot{m}_{S,o} - \dot{m}_{S,23} = 0 \tag{B.24}$$

It is assumed that average enthalpy and density of the vapor for the superheated region equal $h_3 = 0.5(h_o + h_g)$ and $\rho_3 = \rho(p_S, h_3)$, respectively.

The rate of change of mass in the superheated region, first term of Equation (B.2), can be evaluated as:

$$A_S \frac{d}{dt} \int_{L_1+L_2}^{L} \rho dz = A_S \frac{d}{dt} \left[(L - L_1 - L_2) \rho_3 \right] = -A_S \rho_3 \frac{d(L_1+L_2)}{dt} + A_S L_3 \frac{d\rho_3}{dt} \tag{B.25}$$

then Equation (B.24) can be rewritten as:

$$A_S L_3 \frac{d\rho_3}{dt} + A_S (\rho_g - \rho_3) \frac{dL_1}{dt} + A(\rho_g - \rho_3) \frac{dL_2}{dt} = \dot{m}_{S,23} - \dot{m}_{S,o} \tag{B.26}$$

The time derivative of the average liquid density equals the following expression by using the chain rule.

$$\begin{aligned}\frac{d\rho_3}{dt} &= \left.\frac{\partial\rho_3}{\partial p_S}\right|_{h_3}\frac{dp_S}{dt} + \left.\frac{\partial\rho_3}{\partial h_3}\right|_{\rho_S}\frac{dh_3}{dt} \\ &= \left.\frac{\partial\rho_3}{\partial p_S}\right|_{h_3}\frac{dp_S}{dt} + \left.\frac{\partial\rho_3}{\partial h_3}\right|_{\rho_S}\frac{d}{dt}\left[\frac{1}{2}\left(h_o + h_g\right)\right] \\ &= \left(\left.\frac{\partial\rho_3}{\partial p_S}\right|_{h_3} + \frac{1}{2}\left.\frac{\partial\rho_3}{\partial h_3}\right|_{\rho_S}\frac{\partial h_g}{\partial p_S}\right)\frac{dp_S}{dt} + \frac{1}{2}\left.\frac{\partial\rho_3}{\partial h_3}\right|_{\rho_S}\frac{dh_o}{dt}\end{aligned} \tag{B.27}$$

Finally, inserting Equation (B.27) into Equation (B.26) gives the mass balance equation for the superheated region which is

$$A_S\left\{(\rho_g - \rho_3)\frac{d(L_1+L_2)}{dt} + L_3\left(\left.\frac{\partial\rho_3}{\partial p_S}\right|_{h_3} + \frac{1}{2}\left.\frac{\partial\rho_3}{\partial h_3}\right|_{p_S}\frac{\partial h_g}{\partial p_S}\right)\frac{dp_S}{dt} + \frac{1}{2}L_3\left.\frac{\partial\rho_3}{\partial h_3}\right|_{p_S}\frac{dh_o}{dt}\right\} = \dot{m}_{S,23} - \dot{m}_{S,o} \tag{B.28}$$

In a similar manner, integration of the energy balance equation (Equation 3.25) over the superheated region gives that

$$\int_{L_1+L_2}^{L}\frac{\partial\left(A_S\rho h - A_S p\right)}{\partial t} + \int_{L_1+L_2}^{L}\frac{\partial\dot{m}_S h}{\partial z} = \int_{L_1+L_2}^{L}\pi d_i\alpha_i\left(T_M - T_S\right) \tag{B.29}$$

$$\begin{aligned}A_S\frac{d}{dt}\int_{L_1+L_2}^{L}\left(\rho h - p\right)dz + A_S\left[\rho_{(L_1+L_2)}h_{(L_1+L_2)} - p_{(L_1+L_2)}\right]\frac{d\left(L_1+L_2\right)}{dt} + \dot{m}_{S,o}h_o - \dot{m}_{S,23}h_g \\ = \pi d_i\alpha_{i3}(T_{M3} - T_{S3})\end{aligned} \tag{B.30}$$

and evaluating the first term of Equation (B.30) results in

$$\begin{aligned}A_S\frac{d}{dt}\int_{L_1+L_2}^{L}\left(\rho h - p\right)dz &= A_S\frac{d}{dt}\left[\left(\rho_3 h_3 - p_S\right)L_3\right] = A_S\frac{d}{dt}\left(\rho_3 h_3 L_3\right) - A_S p_S\frac{dL_3}{dt} - A_S L_3\frac{dp_S}{dt} \\ &= A_S\left(-\rho_3 h_3\frac{d\left(L_1+L_2\right)}{dt} + L_3\frac{d}{dt}\left(\rho_3 h_3\right) + p_S\frac{d\left(L_1+L_2\right)}{dt} - L_3\frac{dp_S}{dt}\right) \\ &= A_S\left(-\rho_3 h_3\frac{d\left(L_1+L_2\right)}{dt} + L_3 h_3\frac{d\rho_3}{dt} + L_3\rho_3\frac{dh_3}{dt} + p_S\frac{d\left(L_1+L_2\right)}{dt} - L_3\frac{dp_S}{dt}\right)\end{aligned} \tag{B.31}$$

then, replacing the average vapor enthalpy and the rate of change of the average vapor density in Equation (B.31) with their equivalences yields the equation below.

$$A_S \frac{d}{dt}\int_{L_1+L_2}^{L} (\rho h - p)dz = A_S\left\{-(\rho_3 h_3 - p_S)\frac{d(L_1+L_2)}{dt} - L_3\frac{dp_S}{dt}\right\} + A_S\left\{L_3 h_3\left[\left(\left.\frac{\partial\rho_3}{\partial p_S}\right|_{h_3} + \frac{1}{2}\frac{\partial\rho_3}{\partial h_3}\right|_{\rho_S}\frac{\partial h_g}{\partial p_S}\right)\frac{dp_S}{dt} + \frac{1}{2}\left.\frac{\partial\rho_3}{\partial h_3}\right|_{\rho_S}\frac{dh_o}{dt}\right] + \frac{1}{2}L_3\rho_3\left(\frac{dh_o}{dt}+\frac{dh_g}{dt}\right)\right\} \quad \text{(B.32)}$$

Combining Equations (B.30) and (B.32) gives the energy balance equation for the subcooled region.

$$A_S\left\{-(\rho_3 h_3 - p_S)\frac{d(L_1+L_2)}{dt} + L_3 h_3\left[\left(\left.\frac{\partial\rho_3}{\partial p_S}\right|_{h_3} + \frac{1}{2}\frac{\partial\rho_3}{\partial h_3}\right|_{\rho_S}\frac{\partial h_g}{\partial p_S}\right)\frac{dp_S}{dt} + \frac{1}{2}\left.\frac{\partial\rho_3}{\partial h_3}\right|_{\rho_S}\frac{dh_o}{dt}\right]\right\} +$$
$$\frac{1}{2}A_S L_3\rho_3\left(\frac{dh_o}{dt}+\frac{dh_g}{dt}\right) - A_S L_3\frac{dp_S}{dt} + A_S\rho_g h_g\frac{d(L_1+L_2)}{dt} - A_S p_S\frac{d(L_1+L_2)}{dt} \quad \text{(B.33)}$$
$$= -\dot{m}_{S,o}h_o + \dot{m}_{S,23}h_g + \pi d_i\alpha_{i3}(T_{M3}-T_{S3})$$

After algebraic manipulations, the final form of the energy conservation equation is obtained as:

$$A_S\left\{(\rho_g h_g - \rho_3 h_3)\frac{d(L_1+L_2)}{dt} + \frac{1}{2}L_3\left(\rho_3 + h_3\left.\frac{\partial\rho_3}{\partial h_3}\right|_{p_S}\right)\frac{dh_o}{dt} + \right.$$
$$\left. L_3\left(\frac{\rho_3}{2}\frac{\partial h_g}{\partial p_S} + h_3\left(\left.\frac{\partial\rho_3}{\partial p_S}\right|_{h_3} + \frac{1}{2}\left.\frac{\partial\rho_3}{\partial h_3}\right|_{p_S}\frac{\partial h_g}{\partial p_S}\right) - 1\right)\frac{dp_s}{dt}\right\} = \dot{m}_{S,23}h_g - \dot{m}_{S,o}h_o + \pi d_i\alpha_{i3}(T_{M3}-T_{S3}) \quad \text{(B.34)}$$

B.2 Steam Generator Parameters

Table B.1 Steam generator parameters at full power

Variable	Description	Value	Source
L	Steam generator tube length	22.25 m	Reference [31]
L_1	Subcooled region length	1.75 m	Calculated
L_2	Two-phase region length	17.6 m	Calculated
L_3	Superheated region length	2.9 m	Calculated
d_o	Tube outside diameter	1.6 cm	Reference [31]
d_i	Tube inner diameter	1.42 cm	Reference [31]
S_t	Transverse pitch	2.88 cm	Reference [31]
S_l	Longitudinal pitch	2.4 cm	Reference [31]
N	Total number of tubes	1012	Reference [31]
$\dot{m}_{S,o}$	Steam flow rate	71.25 kg/s	Reference [30]
p_S	Steam pressure	3.1 MPa	Reference [30]
T_{Si}	Feedwater inlet temperature	149 °C	Reference [30]
T_{So}	Steam outlet temperature	264 °C	Reference [30]
A_{pht}	Total tube outer heat transfer area	1123 m^2	Calculated
A_{sht}	Total tube inner heat transfer area	1004.5 m^2	Calculated
k_t	Thermal conductivity of Inconel 690 at 280 °C	16.92 W/(m·°C)	Reference [70]
C_L	Steam valve coefficient	2.2983 kg/(s·bar)	Calculated

The steam generator heat transfer process involve three mechanisms: (1) convective heat transfer between the primary coolant and the steam generator tube outer surface, (2) conductive heat transfer within the steam generator tube metal, and (3) convective heat transfer between the steam generator tube inner surface and the secondary coolant. Equations (3.41) and (3.42) give the correlations to calculate heat transfer coefficients for the first and third mechanisms. Reference [70], on the other hand, provides thermal conductivity data of Inconel 690 to determine the conductive heat transfer coefficient. Since the steam generator model consists of three regions, these calculations should be performed for each region. The MATLAB code in the following subsection describes the heat transfer in the steam generator and generates a plot showing the steady-state temperature profile for the steam generator (see Figure 4.13)

B.2.1 MATLAB code for steam generator heat transfer calculations

```
%% Checking heat balance between primary and secondary
% Heat given by primary coolant
G_p = 708; % kg/s
P_p = 124.1; % bar
T_pi = 291.1; % C
T_po = 245.5; % C
h_pi = XSteam('h_pT',P_p,T_pi); % kJ/kg
h_po = XSteam('h_pT',P_p,T_po); % kJ/kg
Q_p = G_p*(h_pi - h_po)/1000; % MWt

% Heat picked up by secondary coolant
G_s = 71.25; % kg/s
P_s = 31; % bar
T_so = 263.8; % C
T_si = 148.9; % C
h_so = XSteam('h_pT',P_s,T_so); % kJ/kg
h_si = XSteam('h_pT',P_s,T_si); % kJ/kg
Q_s = G_s*(h_so - h_si)/1000; % MWt

%% Tp12 - Primary Coolant Temperature at Boundary of Region 1

h_s12 = XSteam('hL_p',P_s); %
Q_s1 = -(h_si - h_s12)*G_s; %
Q_p1 = Q_s1; %

c_p1= XSteam('Cp_pt',P_p,249);

T_p12 = Q_p1/(c_p1*G_p) + T_po;

%% Tp23 - Primary Coolant Temperature at Boundary of Region 2
```

```
h_s23 = XSteam('hV_p',P_s);
Q_s2 = -(h_s12 -h_s23)*G_s; %
Q_p2 = Q_s2; %

c_p2= XSteam('Cp_pt',P_p,278);

T_p23 = Q_p2/(c_p2*G_p) + T_p12;

%% Tpi - Primary Coolant Temperature at Boundary of Region 3

Q_s3 = -(h_s23 -h_so)*G_s; %
Q_p3 = Q_s3; %

c_p3= XSteam('Cp_pt',P_p,290);

T_pi_cal = Q_p3/(c_p3*G_p) + T_p23;
%% Average Primary Coolant Temperature for Each Region
L_1 = 2.89; % subcooled section length (m)
L_2 = 17.6; % boiling section length (m)
L_3 = 1.76; % superheated section length (m)


T_p1 = (T_po + T_p12)/2;
T_p2 = (T_p12*(L_1+L_2) - T_p1*L_2)/L_1;
T_p3 = (T_p23*(L_2+L_3) - T_p2*L_3)/L_2;

%% SUBCOOLED REGION
%% Heat Transfer from Primary Coolant to Tube Outer Surface, Subcooled
do = 1.5875; % tube outside diameter (cm)
St = do*1.8; % transverse pitch (cm)
Sl = do*1.5; % longitudinal pitch (cm)
N = 1012; % total number of steam generator tubes
G_pc = G_p/N; % primary flow rate per channel (kg/s)
de = 4*((St*Sl - pi*(do/2)^2) / (pi*do)); % equivalent  diameter (cm)
rho_p1 = XSteam('rho_pT',P_p,T_p1); % density of water (kg/m^3)
A_pc = St*Sl - pi*(do/2)^2; % primary coolant flow area per channel (cm^2)
V_pc1 = L_1*A_pc/10000; % primary coolant volume per channel (m^3)
m_p1 = V_pc1*rho_p1; % primary coolant mass per channel (kg)
v_p1 = (G_pc*L_1)/m_p1; % primary coolant velocity (m/s)
v_mp1 = (St/(St-do))*v_p1; % primary coolant max velocity (m/s)
mu_p1 = XSteam('my_pT',P_p,T_p1); % viscosity of water (kg/m-s)
k_p1 = 0.630075; % thermal conductivity of water (W/m-C)
Re_p1 = (0.01*do*v_mp1*rho_p1/mu_p1); % Reynolds number
Pr_p1 = 1000*c_p1*mu_p1/k_p1; % Prandtl number
Nu_p1 = 0.021*Re_p1^0.84*Pr_p1^0.36; % Nusselt number
H1 = (Nu_p1*k_p1/(do*0.01)); % heat transfer coefficient (W/m^2-C)
A_ph1 = (pi*do*L_1)/100; % heat transfer area per tube (m^2)
A_pht1 = N*A_ph1; % total heat transfer area (m^2)

T_m1o = T_p1 - (Q_p1/(H1*A_pht1))*1000; % tube metal outside temperature (C)

%% Heat Transfer from Tube Outer Surface to Tube Inner Surface, Subcooled

k_t1 = 16.16; % thermal conductivity of Inconel 690 at 240 C (W/m-C)
di = 1.42; % tube inner diameter (cm)
t = 0.09; % tube thickness (cm)
R_t1 = (1/(2*pi*k_t1*L_1))*log((di/2 + t)/(di/2)); % thermal resistance (W/C)^-1
H_t1 = 1/(R_t1*A_ph1); % heat transfer coefficient (W/m^2-C)

T_m1i = T_m1o - (Q_p1/(H_t1*A_pht1))*1000; % tube metal inside temperature (C)

%% Heat Transfer from Tube Inner Surface to Secondary Coolant, Subcooled
G_st = G_s/N; % secondary coolant flow per tube (kg/s)
rho_s1 = XSteam('rho_pT',P_s,194); % density of water(kg/m^3)
A_sc = pi*(di/2)^2/10000; % secondary coolant flow are per tube (m^2)
V_sc1 = L_1*(A_sc); % secondary coolant volume per tube (m^3)
m_s1 = V_sc1*rho_s1; % secondary coolant mass per tube (kg)
v_s1 = (G_st*L_1)/m_s1; % secondary coolant velocity (m/s)
mu_s1 = XSteam('my_pT',P_s,194); % viscosity of water (kg/m-s)
```

```
k_s1 = 0.657239; % thermal conductivity of water (W/m-C)
c_s1 = XSteam('Cp_pt',P_s,194); % specific heat of water (kJ/kg-C)
Re_s1 = (0.01*di*v_s1*rho_s1/mu_s1); % Reynolds number
Pr_s1 = 1000*c_s1*mu_s1/k_s1; % Prandtl number
Nu_s1 = 0.023*Re_s1^0.8*Pr_s1^0.4; % Nusselt number
H_s1 = (Nu_s1*k_s1/(di*0.01)); %heat transfer coefficient (W/m^2-C)
A_sh1 = (pi*di*L_1)/100; % heat transfer area per tube (m^2)
A_sht1 = N*A_sh1; % total heat transfer area (m^2)

T_s12 = XSteam('Tsat_p',P_s); % saturation temperature at 31 bar
T_s1 = T_m1i - (Q_p1/(H_s1*A_sht1))*1000;


%% BOILING REGION
%% Heat Transfer from Primary Coolant to Tube Outer Surface, Boiling
rho_p2 = XSteam('rho_pT',P_p,T_p2); % density of water (kg/m^3)
V_pc2 = L_2*A_pc/10000; % primary coolant volume per channel (m^3)
m_p2 = V_pc2*rho_p2; % primary coolant mass per channel (kg)
v_p2 = (G_pc*L_2)/m_p2; % primary coolant velocity (m/s)
v_mp2 = (St/(St-do))*v_p2; % primary coolant max velocity (m/s)
mu_p2 = XSteam('my_pT',P_p,T_p2); % viscosity of water (kg/m-s)
k_p2 = 0.601028; % thermal conductivity of water (W/m-C)
Re_p2 = (0.01*do*v_mp2*rho_p2/mu_p2); % Reynolds number
Pr_p2 = 1000*c_p2*mu_p2/k_p2; % Prandtl number
Nu_p2 = 0.021*Re_p2^0.84*Pr_p2^.36; % Nusselt number
H2 = (Nu_p2*k_p2/(do*0.01)); % heat transfer coefficient (W/m^2-C)
A_ph2 = (pi*do*L_2)/100; % heat transfer area per tube (m^2)
A_pht2 = N*A_ph2; % total heat transfer area (m^2)

T_m2o = T_p2 - (Q_p2/(H2*A_pht2))*1000; % tube metal outside temperature (C)

%% Heat Transfer from Tube Outer Surface to Tube Inner Surface, Boiling

k_t2 = 16.73; % thermal conductivity of Inconel 690 at 270 C (W/m-C)
R_t2 = (1/(2*pi*k_t2*L_2))*log((di/2 + t)/(di/2)); % thermal resistance (W/C)^-1
H_t2 =  1/(R_t2*A_ph2); % heat transfer coefficient (W/m^2-C)

T_m2i = T_m2o - (Q_p2/(H_t2*A_pht2))*1000; % tube metal inside temperature (C)

%% SUPERHEATER REGION
%% Heat Transfer from Primary Coolant to Tube Outer Surface, Superheated
rho_p3 = XSteam('rho_pT',P_p,T_p3); % density of water (kg/m^3)
V_pc3 = L_3*A_pc/10000; % primary coolant volume per channel (m^3)
m_p3 = V_pc3*rho_p3; % primary coolant mass per channel (kg)
v_p3 = (G_pc*L_3)/m_p3; % primary coolant velocity (m/s)
v_mp3 = (St/(St-do))*v_p3; % primary coolant max velocity (m/s)
mu_p3 = XSteam('my_pT',P_p,T_p3); % viscosity of water (kg/m-s)
k_p3 = 0.573095; % thermal conductivity of water (W/m-C)
Re_p3 = (0.01*do*v_mp3*rho_p3/mu_p3); % Reynolds number
Pr_p3 = 1000*c_p3*mu_p3/k_p3; % Prandtl number
Nu_p3 = 0.021*Re_p3^0.84*Pr_p3^.36; % Nusselt number
H3 = (Nu_p3*k_p3/(0.01*do)); % heat transfer coefficient (W/m^2-C)
A_ph3 = (pi*do*L_3)/100; % heat transfer area per tube (m^2)
A_pht3 = N*A_ph3; % total heat transfer area (m^2)

T_m3o = T_p3 - (Q_p3/(H3*A_pht3))*1000; % tube metal outside temperature (C)

%% Heat Transfer from Tube Outer Surface to Tube Inner Surface, Superheated

k_t3 = 16.92; % thermal conductivity of Inconel 690 at 280 C (W/m-C)
R_t3 = (1/(2*pi*k_t3*L_3))*log((di/2 + t)/(di/2)); % thermal resistance (W/C)^-1
H_t3 = 1/(R_t3*A_ph3); % heat transfer coefficient (W/m^2-C)

T_m3i = T_m3o - (Q_p3/(H_t3*A_pht3))*1000; % tube metal inside temp (C)

%% Heat Transfer from Tube Inner Surface to Secondary Coolant, Superheated
rho_s3 = XSteam('rho_pT',P_s,250); % density of steam (kg/m^3)
V_sc3 = L_3*(A_sc); % secondary coolant volume per tube (m^3)
m_s3 = V_sc3*rho_s3; % secondary coolant mass per tube (kg)
```

```
v_s3 = (G_st*L_3)/m_s3; % secondary coolant velocity (m/s)
mu_s3 = 0.000017321; % viscosity of steam (kg/m-s)
k_s3 = 0.047217458; % thermal conductivity of steam (W/m-C)
c_s3 = XSteam('Cp_pt',P_s,250); % specific heat of water (kJ/kg-C)
Re_s3 = (0.01*di*v_s3*rho_s3/mu_s3); % Reynolds number
Pr_s3 = 1000*c_s3*mu_s3/k_s3; % Prandtl number
Nu_s3 = 0.023*Re_s3^0.8*Pr_s3^0.4; % Nusselt number
H_s3 = (Nu_s3*k_s3/(0.01*di)); %heat transfer coefficient (W/m^2-C)
A_sh3 = (pi*di*L_3)/100; % heat transfer area per tube (m^2)
A_sht3 = N*A_sh3; % total heat transfer area (m^2)

T_s3 = T_m3i - (Q_p3/(H_s3*A_sht3))*1000;
T_s23 = T_s12;

%% Plotting the Steady-State Temperature Profile
L = 22.25; % length of single tube (m)
T_m1 =(T_m1i+T_m1o)/2;
T_m2 =(T_m2i+T_m2o)/2;
T_m3 =(T_m3i+T_m3o)/2;
T_m12 = (L_2*T_m1+L_1*T_m2)/(L_1+L_2);
T_m23 = (L_3*T_m2+L_2*T_m3)/(L_2+L_3);
T_mi = 2*T_m1 - T_m12;
T_mo = 2*T_m3 - T_m23;

T_p = [T_po T_p1 T_p12 T_p23 T_p3 T_pi]
T_m = [T_mi T_m1 T_m12 T_m23 T_m3 T_mo]
T_s = [T_si T_s1 T_s12 T_s23 T_s3 T_so]
Length = [0 L_1/2 L_1 L_1+L_2 (L+L_1+L_2)/2 L];

figure(2)
set(gca,'Fontsize',12);
hold on
plot(Length,T_p,'r','LineWidth',2);
plot(Length,T_s,'--b','LineWidth',2);
plot(Length,T_m,':k','Linewidth', 2)
grid on
xlabel('Tube Length (m)')
ylabel('Temperature (^oC)');
title('');
xlim([0 22.25])
legend('primary','secondary','tube metal','Location','South');

x = [0.23 0.16];
y = [0.2 0.3];
a = annotation('textarrow',x,y,'String','Subcooled');
a.FontSize = 14;

x1 = [0.5 0.5];
y1 = [0.5 0.6];
b = annotation('textarrow',x1,y1,'String','Two-phase');
b.FontSize = 14;

x2 = [0.8 0.88];
y2 = [0.7 0.7];
c = annotation('textarrow',x2,y2,'String','Superheated');
c.FontSize = 14;
```

APPENDIX C

HOT LEG RISER, DOWNCOMER, PRESSURIZER, AND STEAM TURBINE PARAMATERS

C.1 Hot Leg Riser, Downcomer, Pressurizer, and Steam Turbine Parameters

Table C.1 Hot leg riser, downcomer, pressurizer, and steam turbine parameters

Variable	Description	Value	Source
V_{HL}	Primary coolant volume in hot leg riser	9.7 m^3	Reference [31]
ρ_{HL}	Primary coolant density in hot leg riser (12.76 MPa & 291 °C)	739.6 kg/m^3	Reference [69]
m_{HL}	Primary coolant mass in hot leg riser	7174 kg	Calculated
V_{DR}	Primary coolant volume in downcomer	26.8 m^3	Reference [31]
ρ_{DR}	Primary coolant density in downcomer (12.41 MPa & 246 °C)	814 kg/m^3	Reference [69]
m_{DR}	Primary coolant mass in downcomer	21815 kg	Calculated
V_v	Vapor volume inside pressurizer	2.9 m^3	Reference [31]
V_l	Liquid volume inside pressurizer	2.9 m^3	Estimated
p_p	Pressurizer pressure	12.41 MPa	Calculated
h_o	Steam enthalpy at steam turbine inlet (3.1 MPa & 264 °C)	2893 kJ/kg	Reference [69]
p_c	Steam turbine exhaust (or condenser) pressure	0.2 bar	Reference [61]
x	Ideal Rankine cycle steam exit quality	0.78	Calculated
n_{Turb}	Isentropic turbine efficiency	0.83	Reference [61]
h_c	Steam enthalpy at steam turbine outlet	2226 kJ/kg	Calculated
$K_{P,T}$	Proportional gain for sliding-average-temperature controller	0.9	Calculated

$\boldsymbol{K_{I,T}}$	Integral gain for sliding-average-temperature controller	0.023	Calculated
$\boldsymbol{K_{P,p}}$	Proportional gain for pressurizer pressure controller	–200	Calculated
$\boldsymbol{K_{I,p}}$	Integral gain for pressurizer pressure controller	–0.02	Calculated
$\boldsymbol{K_{D,p}}$	Derivate gain for pressurizer pressure controller	–3000	Calculated

C.2 PI Controller Tuning

The PI controller parameters for the sliding-average-temperature control mode are tuned with the help of MATLAB/Simulink PID Tuner [62] and the nominal values for proportional ($K_{P,T}$) and integral ($K_{I,T}$) gains are found to be 0.9 and 0.023, respectively, as shown in Table C.1.

This section includes the necessary plots to exhibit the effect of different values of these gains on important state variables, i.e., the reactor thermal power and downcomer temperature, and provide a basis for the author's choice on the aforementioned values.

C.2.1 Effect of proportional gain

The effect of the proportional gain on important state variables, i.e., the reactor thermal power and downcomer temperature, is investigated by keeping the integral gain constant and altering the proportional gain within a range of $0.5 \leq K_{P,T} \leq 1.5$. However, the results for only three different values of $K_{P,T}$ are shown in Figures C.1 and C.2.

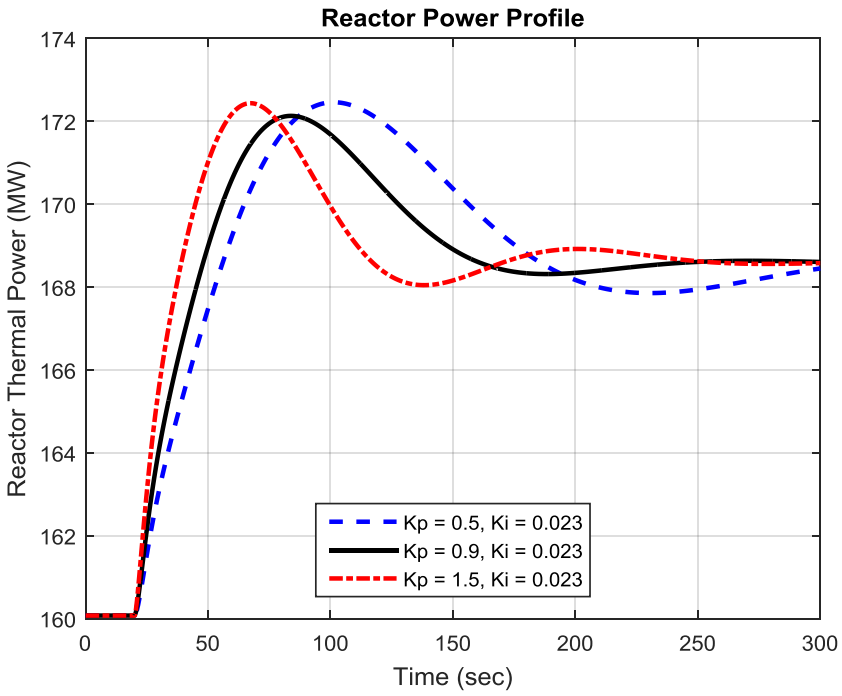

Figure C.1 Effect of proportional gain ($K_{P,T}$) on reactor thermal power.

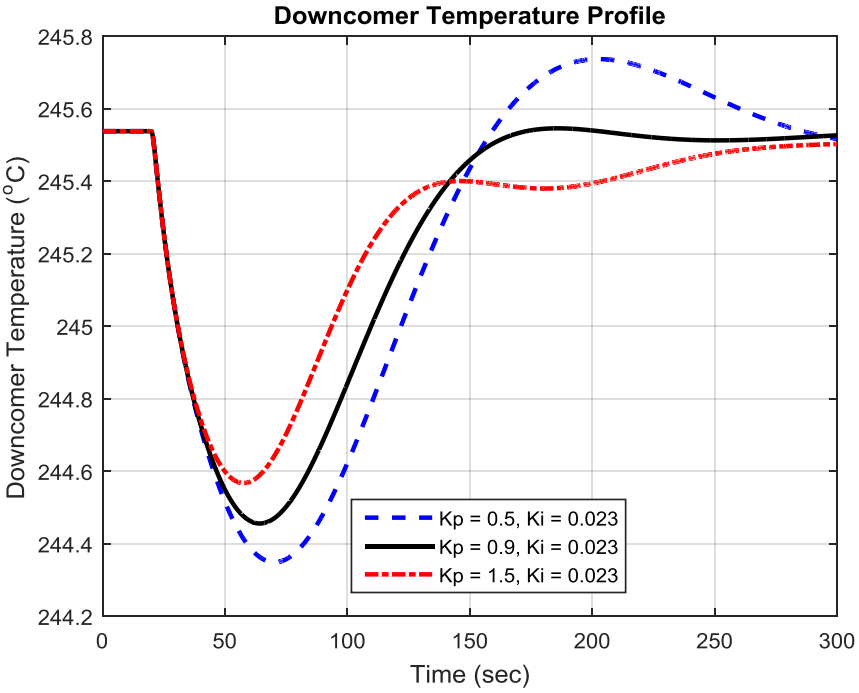

Figure C.2 Effect of proportional gain ($K_{P,T}$) on downcomer temperature.

C.2.2 Effect of integral gain

In a similar manner, the effect of the proportional gain on the reactor thermal power and downcomer temperature is investigated by keeping the proportional gain constant and altering the integral gain within a range of $0.01 \leq K_{P,T} \leq 0.03$. However, the results for only three different values of $K_{P,I}$ are shown in Figures C.3 and C.4.

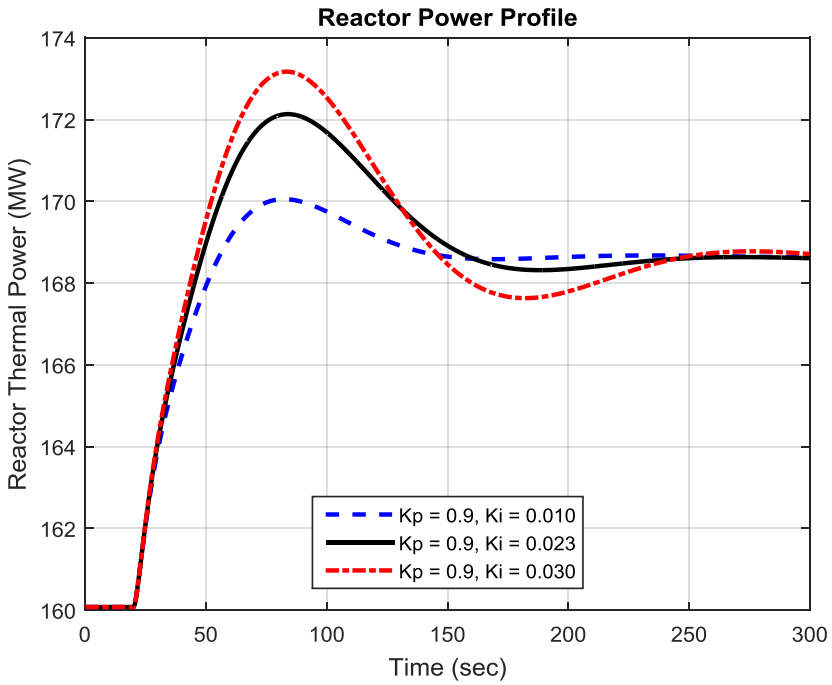

Figure C.3 Effect of integral gain ($K_{I,T}$) on reactor thermal power.

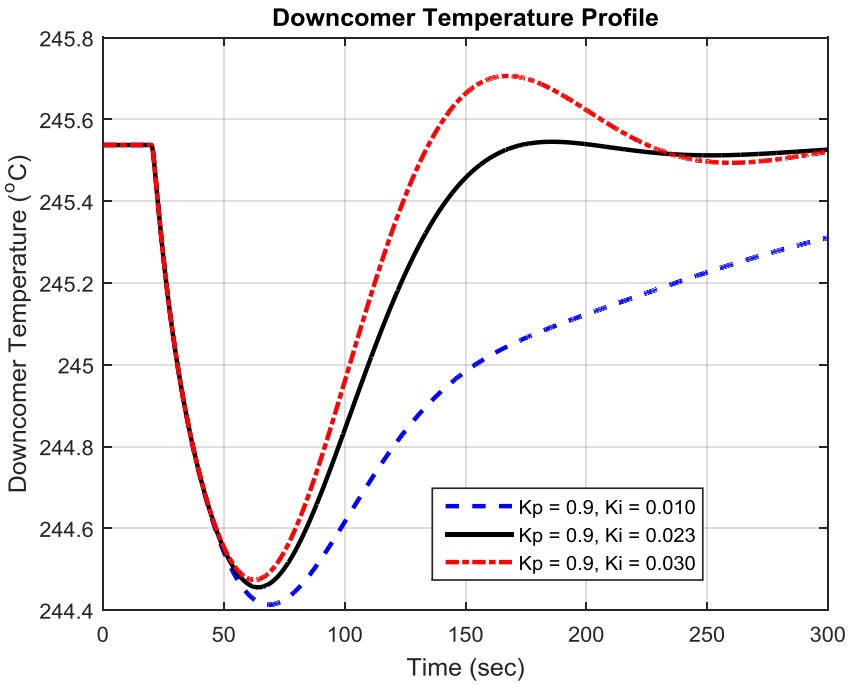

Figure C.4 Effect of integral gain ($K_{I,T}$) on downcomer temperature.

APPENDIX D

LINEARIZATION

In this study, a small perturbation method, $\delta x = x - x_0$, is used to linearize the dynamic models. All variables in the following equations with a subscript of 0 represent the initial steady-state value of that variable.

D.1 Reactor Core Model

D.1.1 Reactor neutronics

After replacing the reactivity term (ρ) in Equation (3.1) with its equivalent, the point kinetics equations are linearized to

$$\frac{d\delta P}{dt} = \frac{-\beta}{\Lambda}\delta P + \lambda\delta C + \frac{\alpha_F P_0}{\Lambda}\delta T_F + \frac{\alpha_C P_0}{\Lambda}\delta T_C + \frac{\alpha_P P_0}{\Lambda}\delta p_P + \frac{P_0}{\Lambda}\delta\rho_{ext} \tag{D.1}$$

$$\frac{d\delta C}{dt} = \frac{\beta}{\Lambda}\delta P - \lambda\delta C \tag{D.2}$$

D.1.2 Reactor thermal-hydraulics

Introducing perturbation variables in Equations (3.4), (3.5), and (3.6), the linearized form of the reactor thermal hydraulics is given by

$$m_F c_{p,F}\frac{d\delta T_F}{dt} = f_d\delta P - (UA)_{FC}(\delta T_F - \delta T_{C1}) \tag{D.3}$$

$$\left(\frac{m_C}{2}c_{p,C}\right)\frac{d\delta T_{C1}}{dt} = \left(\frac{1-f_d}{2}\right)\delta P + \left(U\frac{A}{2}\right)_{FC}(\delta T_F - \delta T_{C1}) - \dot{m}_{C,0}c_{p,C}(\delta T_{C1} - \delta T_{Ci}) - c_{p,C}(T_{C1,0} - T_{Ci,0})\delta\dot{m}_C \tag{D.4}$$

$$\left(\frac{m_C}{2}c_{p,C}\right)\frac{d\delta T_{C2}}{dt} = \left(\frac{1-f_d}{2}\right)\delta P + \left(U\frac{A}{2}\right)_{FC}(\delta T_F - \delta T_{C1}) - \dot{m}_{C,0}c_{p,C}(\delta T_{C2} - \delta T_{C1}) - c_{p,C}(T_{C2,0} - T_{C1,0})\delta\dot{m}_C \tag{D.5}$$

D.2 Hot Leg Riser and Downcomer Region

In a similar manner, equations for the hot leg riser and downcomer are linearized to

$$m_{HL}c_{p,HL}\frac{d\delta T_{HL}}{dt}=\dot{m}_{HL,0}c_{p,HL}\left(\delta T_{C2}-\delta T_{HL}\right)+c_{p,HL}\left(T_{C2,0}-T_{HL,0}\right)\delta\dot{m}_{HL} \tag{D.6}$$

$$m_{DR}c_{p,DR}\frac{d\delta T_{DR}}{dt}=\dot{m}_{DR,0}c_{p,DR}\left(\delta T_{P1}-\delta T_{DR}\right)+c_{p,DR}\left(T_{P1,0}-T_{DR,0}\right)\delta\dot{m}_{DR} \tag{D.7}$$

D.3 Steam Generator Model

Steam generator model is in the form of Equation (3.45) and after applying the small perturbation linearization method it can be stated as

$$\boldsymbol{\delta\dot{\mathbf{x}}}=\left(\mathbf{D}\big|_{\mathbf{x}_0,\mathbf{u}_0}\right)^{-1}\left[\frac{\partial\mathbf{f}}{\partial\mathbf{x}}\bigg|_{\mathbf{x}_0,\mathbf{u}_0}\right]\boldsymbol{\delta\mathbf{x}}+\left(\mathbf{D}\big|_{\mathbf{x}_0,\mathbf{u}_0}\right)^{-1}\left[\frac{\partial\mathbf{f}}{\partial\mathbf{u}}\bigg|_{\mathbf{x}_0,\mathbf{u}_0}\right]\boldsymbol{\delta\mathbf{u}} \tag{D.8}$$

then it is possible to rewrite Equation (D.8) in the general form for a linear system ($\dot{\mathbf{x}} = \mathbf{Ax} + \mathbf{Bu}$)

$$\boldsymbol{\delta\dot{\mathbf{x}}}=\mathbf{D}^{-1}\mathbf{F}_{\mathbf{x}}\boldsymbol{\delta\mathbf{x}}+\mathbf{D}^{-1}\mathbf{F}_{\mathbf{u}}\boldsymbol{\delta\mathbf{u}} \tag{D.9}$$

The partial derivative of the function $\mathbf{f}(\mathbf{x},\mathbf{u})$ with respect to the state and input variables are defined in Equations (D.10) and (D.11), with the matrix elements listed in Tables D.1 and D.2, respectively.

$$\frac{\partial \mathbf{f}}{\partial \mathbf{x}} = \mathbf{F}_{\mathbf{x}} = \begin{bmatrix} f_{x,11} & 0 & f_{x,13} & 0 & f_{x,15} & 0 & 0 & 0 & 0 & 0 \\ 0 & f_{x,22} & f_{x,23} & 0 & 0 & f_{x,26} & 0 & 0 & 0 & 0 \\ f_{x,31} & f_{x,32} & f_{x,33} & f_{x,34} & 0 & 0 & f_{x,37} & 0 & 0 & 0 \\ 0 & 0 & 0 & 0 & 0 & 0 & 0 & 0 & 0 & 0 \\ f_{x,51} & 0 & f_{x,53} & 0 & f_{x,55} & 0 & 0 & f_{x,58} & 0 & 0 \\ 0 & f_{x,62} & f_{x,63} & 0 & 0 & f_{x,66} & 0 & 0 & f_{x,69} & 0 \\ f_{x,71} & f_{x,72} & f_{x,73} & f_{x,74} & 0 & 0 & f_{x,77} & 0 & 0 & f_{x,710} \\ f_{x,81} & 0 & 0 & 0 & f_{x,85} & 0 & 0 & f_{x,88} & f_{x,89} & 0 \\ 0 & f_{x,92} & 0 & 0 & 0 & f_{x,96} & 0 & 0 & f_{x,99} & f_{x,910} \\ f_{x,101} & f_{x,102} & 0 & 0 & 0 & 0 & f_{x,107} & 0 & 0 & f_{x,1010} \end{bmatrix} \tag{D.10}$$

$$\frac{\partial \mathbf{f}}{\partial \mathbf{u}} = \mathbf{F}_{\mathbf{u}} = \begin{bmatrix} f_{u,11} & 0 & f_{u,13} & 0 & 0 \\ f_{u,21} & f_{u,22} & 0 & 0 & 0 \\ 0 & f_{u,32} & 0 & 0 & 0 \\ f_{u,41} & f_{u,42} & 0 & 0 & 0 \\ 0 & 0 & f_{u,53} & 0 & 0 \\ 0 & 0 & 0 & 0 & 0 \\ 0 & 0 & 0 & 0 & 0 \\ 0 & 0 & 0 & 0 & f_{u,85} \\ 0 & 0 & 0 & 0 & f_{u,95} \\ 0 & 0 & 0 & f_{u,104} & f_{u,105} \end{bmatrix} \tag{D.11}$$

Table D.1 Elements of matrix $\mathbf{F_x}$.

Index	Element
$f_{x,11}$	$\pi d_i \alpha_{i1}(T_{M1} - T_{S1})$
$f_{x,13}$	$-\dot{m}_{S,i}\frac{\partial h_f}{\partial p_S} - \pi d_i \alpha_{i1} L_1 \left(\frac{\partial T_{S1}}{\partial p_S}\right)$
$f_{x,15}$	$\pi d_i \alpha_{i1} L_1$
$f_{x,22}$	$\pi d_i \alpha_{i2}(T_{M2} - T_{S2})$
$f_{x,23}$	$\dot{m}_{S,i}\frac{\partial h_f}{\partial p_S} - \dot{m}_{S,o}\frac{\partial h_g}{\partial p_S} - \pi d_i \alpha_{i2} L_2 \left(\frac{\partial T_{sat}}{\partial p_S}\right)$
$f_{x,26}$	$\pi d_i \alpha_{i2} L_2$
$f_{x,31}$	$-\pi d_i \alpha_{i3}(T_{M3} - T_{S3})$
$f_{x,32}$	$-\pi d_i \alpha_{i3}(T_{M3} - T_{S3})$
$f_{x,33}$	$\dot{m}_{S,o}\frac{\partial h_g}{\partial p_S} - \pi d_i \alpha_{i3} L_3 \left(\frac{\partial T_{S3}}{\partial p_S}\right)$
$f_{x,34}$	$-\dot{m}_{S,o} - \pi d_i \alpha_{i3} L_3 \left(\frac{\partial T_{S3}}{\partial h_o}\right)$
$f_{x,37}$	$\pi d_i \alpha_{i3} L_3$
$f_{x,51}$	$\pi\left[d_o \alpha_{o1}(T_{P1} - T_{M1}) - d_i \alpha_{i1}(T_{M1} - T_{S1})\right]$
$f_{x,53}$	$\pi d_i \alpha_{i1} L_1 \left(\frac{\partial T_{S1}}{\partial p_S}\right)$
$f_{x,55}$	$-\pi L_1\left[d_o \alpha_{o1} + d_i \alpha_{i1}\right]$
$f_{x,58}$	$\pi d_o \alpha_{o1} L_1$
$f_{x,62}$	$\pi\left[d_o \alpha_{o2}(T_{P2} - T_{M2}) - d_i \alpha_{i2}(T_{M2} - T_{S2})\right]$
$f_{x,63}$	$\pi d_i \alpha_{i2} L_2 \left(\frac{\partial T_{sat}}{\partial p_S}\right)$
$f_{x,66}$	$-\pi L_2\left[d_o \alpha_{o2} + d_i \alpha_{i2}\right]$
$f_{x,69}$	$\pi d_o \alpha_{o2} L_2$

$f_{x,71}$	$-\pi\left[d_o\alpha_{o3}(T_{P3}-T_{M3})-d_i\alpha_{i3}(T_{M3}-T_{S3})\right]$
$f_{x,72}$	$-\pi\left[d_o\alpha_{o3}(T_{P3}-T_{M3})-d_i\alpha_{i3}(T_{M3}-T_{S3})\right]$
$f_{x,73}$	$\pi d_i\alpha_{i3}L_3\left(\frac{\partial T_{S3}}{\partial p_S}\right)$
$f_{x,74}$	$\pi d_i\alpha_{i3}L_3\left(\frac{\partial T_{S3}}{\partial h_o}\right)$
$f_{x,77}$	$-\pi L_3\left[d_o\alpha_{o3}+d_i\alpha_{i3}\right]$
$f_{x,710}$	$\pi d_o\alpha_{o3}L_3$
$f_{x,81}$	$-\pi d_o\alpha_{o1}(T_{P1}-T_{M1})$
$f_{x,85}$	$\pi d_o\alpha_{o1}L_1$
$f_{x,88}$	$-\left(\dot{m}_P c_{p,P}+\pi d_o\alpha_{o1}L_1\right)$
$f_{x,89}$	$\dot{m}_P c_{p,P}$
$f_{x,92}$	$-\pi d_o\alpha_{o2}(T_{P2}-T_{M2})$
$f_{x,96}$	$\pi d_o\alpha_{o2}L_2$
$f_{x,99}$	$-\left(\dot{m}_P c_{p,P}+\pi d_o\alpha_{o2}L_2\right)$
$f_{x,910}$	$\dot{m}_P c_{p,P}$
$f_{x,101}$	$\pi d_o\alpha_{o3}(T_{P3}-T_{M3})$
$f_{x,102}$	$\pi d_o\alpha_{o3}(T_{P3}-T_{M3})$
$f_{x,107}$	$\pi d_o\alpha_{o3}L_3$
$f_{x,1010}$	$-\left(\dot{m}_P c_{p,P}+\pi d_o\alpha_{o3}L_3\right)$

Table D.2 Elements of matrix $\mathbf{F_u}$.

Index	Element
$f_{u,11}$	$(h_i - h_f)$
$f_{u,13}$	$-\dot{m}_{S,i} - \pi d_i \alpha_{i1} L_1 \left(\frac{\partial T_{S1}}{\partial h_i} \right)$
$f_{u,21}$	h_f
$f_{u,22}$	$-h_g$
$f_{u,32}$	$(h_g - h_o)$
$f_{u,41}$	1
$f_{u,42}$	-1
$f_{u,53}$	$\pi d_i \alpha_{i1} L_1 \left(\frac{\partial T_{S1}}{\partial h_i} \right)$
$f_{u,85}$	$c_{p,P}(T_{P2} - T_{P1})$
$f_{u,95}$	$c_{p,P}(T_{P3} - T_{P2})$
$f_{u,104}$	$\dot{m}_P c_{p,P}$
$f_{u,105}$	$c_{p,P}(T_{Pi} - T_{P3})$

D.4 Pressurizer Model

After applying perturbation variables, Equation (3.53) takes the linearized form of

$$m_{l,0}\left(\frac{\partial u_f}{\partial p_P} - p_{P,0}\frac{\partial \upsilon_f}{\partial p_{P,0}}\right)\frac{d\delta p_P}{dt} = \delta Q_h + \left(h_0 - h_{f,0} + p_{P,0}\upsilon_{f,0}\right)\delta\dot{m}_{su} + \left(h_{DR,0} - h_{f,0} + p_{P,0}\upsilon_{f,0}\right)\delta\dot{m}_{sp} - \left(h_{fg,0} + p_{P,0}\upsilon_{f,0}\right)\delta\dot{m}_{ec} + \left[\dot{m}_{su,0}\left(-c_p\frac{\partial T_{sat}}{\partial p_P} + Y\right) + \dot{m}_{sp,0}\left(-c_p\frac{\partial T_{sat}}{\partial p_P} + Y\right) - \dot{m}_{ec,0}(Y)\right]\delta p_P \quad \text{(D.12)}$$

where $Y = p_{P,0}\dfrac{\partial \upsilon_f}{\partial p_P} + \upsilon_{f,0}$

Following that a linear expression for the condensation-evaporation rate is derived by utilizing the ideal gas law equation.

$$\delta \dot{m}_{ec} = \frac{1}{A}\frac{d\delta p_P}{dt} - \frac{B}{A}\frac{d\delta m_l}{dt} \tag{D.13}$$

where $A = \dfrac{RT_{sat,0}}{V_{v,0} - Rm_{v,0}\dfrac{\partial T_{sat}}{\partial p_p}}$ $\qquad$ $B = \dfrac{p_{p,0}\upsilon_f}{V_{v,0} - Rm_{v,0}\dfrac{\partial T_{sat}}{\partial p_p}}$

Finally, the linearized pressurizer pressure equation is obtained by substituting Equation (D.12) and the linearized version of Equation (3.46) into Equation (D.13), which is

$$\begin{aligned}
&\left[m_{l,0}\left(\frac{\partial u_f}{\partial p_P} - p_{P,0}\frac{\partial \upsilon_f}{\partial p_{P,0}} \right) + \frac{h_{fg,0} + p_{P,0}\upsilon_{f,0}}{A} + \frac{B}{A}\left(\frac{h_{fg,0} + p_{P,0}\upsilon_{f,0}}{A-B} \right) \right]\frac{d\delta p_P}{dt} = \\
&\qquad \delta Q_h + \left[h_0 - h_{f,0} + p_{P,0}\upsilon_{f,0} + \frac{B}{A-B}\left(h_{fg,0} + p_{P,0}\upsilon_{f,0} \right) \right]\delta \dot{m}_{su} \\
&\qquad + \left[h_{DR,0} - h_{f,0} + p_{P,0}\upsilon_{f,0} + \frac{B}{A-B}\left(h_{fg,0} + p_{P,0}\upsilon_{f,0} \right) \right]\delta \dot{m}_{sp} \\
&\qquad + \left[\dot{m}_{su,0}\left(-c_p\frac{\partial T_{sat}}{\partial p_P} + Y \right) + \dot{m}_{sp,0}\left(-c_p\frac{\partial T_{sat}}{\partial p_P} + Y \right) - \dot{m}_{ec,0}\left(Y \right) \right]\delta p_P
\end{aligned} \tag{D.14}$$